Designing Novel Chemical Tools Based on Optimized Rhodamine Fluorophores For Applications in Live Cell Nanoscopy

By

Jonathan Tyson

A dissertation submitted in partial satisfaction of the

requirements for the degree of

Doctor of Philosophy

in

Chemistry

in the

College of Chemistry

of the

University of California, Berkeley

Committee in charge:

Professor Alanna Schepartz, Chair
Professor Christopher Chang
Professor Roberto Zoncu

Summer 2021

Abstract

Designing Novel Chemical Tools Based on Optimized Rhodamine Fluorophores For Applications in Live Cell Nanoscopy

By

Jonathan Tyson

Doctor of Philosophy in Chemistry

University of California, Berkeley

Professor Alanna Schepartz, Chair

True molecular understanding of cellular and chemical biology requires the characterization of cellular structures with high spatial resolution in living cells. Over the past two decades, super-resolution microscopy (also called 'nanoscopy') has emerged as a powerful tool for the visualization of cellular structures with nanoscale resolution. The efficiency of nanoscopy; however, is limited by the fuel—the chemical tools that support the vast lists of requirements for stimulated emission depletion (STED) and single molecule localization microcopy (SMLM). This dissertation describes worked pursued during my graduate degree towards the development of new and unique chemical tools to expand the capabilities of live cell nanoscopy and accordingly advance cell and chemical biology. **Chapter 1** provides an introduction to and in-depth discussion of relevant concepts (e.g., nanoscopy, spontaneously blinking fluorophores), ultimately concluding with an overview and analysis of a class of dual component chemical tools developed by our lab termed high density environmentally sensitive (HIDE) probes. **Chapter 2** describes the application of HIDE probes to multicolor imaging via simultaneous development of a mutually orthogonal bioorthogonal labeling platform and development of a novel stimulated emission depletion (STED)-compatible rhodamine fluorophore. **Chapter 3** describes the development of novel bright and near-IR emitting spontaneously blinking fluorophores for two-color live cell single molecule localization microscopy (SMLM) without chemical additives and with only a single 642 nm laser. **Chapter 4** briefly summarized a series of projects that were designed, but not executed during my time in the lab.

Acknowledgements

I would like to express my utmost gratitude and appreciation to all of those who have made possible the work described herein. First, to my dissertation advisor, Professor Alanna Schepartz, I would like to thank you for all of the many contributions you have made to my academic and professional development over the years. I joined graduate school as a student, but as a result of your exquisite membership, I leave as a scientist. I'd like to express similar appreciation to Professors Derek Toomre, Joerg Bewersdorf and Jonathan Ellman for their additional mentorship, allowing me to make my way through graduate school with a diverse set of skills. I also would like to thank peers and mentors who have contributed to my development, including, but not limited to Kevin Hu, Dr. Alex Thompson, Dr. Aarushi Gupta, Dr. Ling Chu, Dr. Shuai Zheng and Dr. Andrew Cairns. I'd likewise like to thank the many friends I made along the way for entertainment and good conversation. This includes, but is not limited to James Kweon, Dr. Anthony Scruse, Dr. Charles Brown, Dr. Masha Elkin, Dr. Susan Knox, Patrick Ginther, Neville Dadina, Deepto Mozumdar and Rishi Argawal.

Finally, to my family and loved ones, I thank you for keeping me sane over the last five years. Mom and pops, thank you for the early sacrifices that made it possible for a first generation American and first generation college student to make it this far. Mom, I additionally thank you for being an amazing listener and entertaining all the random facts and observations I have shared with you about science. Josh, Jenille, Terrelle, Mario and Steph, thank you for your continued support. Last, but certainly, not least, I'd like to thank my amazing girlfriend Ligia Sandoval. You have offered me a tremendous amount of support throughout the years, and accordingly you likely deserve this degree as much as I do. Thank you for being there and baring with me through late nights at lab and lost weekends. I couldn't have done it without you and Marley.

Chapter 1. Introduction to HIDE Probes and Other Relevant Technologies

This chapter serves to introduce key ideas and concepts relevant to the entirety of the manuscript and also provides an overview of a class of dual component chemical tools developed by the Schepartz Lab of Chemical Biology called high density environmentally sensitive (HIDE) probes. These probes and technologies to support them are the focus of this dissertation.

1.1 Introduction

True molecular understanding of biology requires the characterization of cellular structures with high spatial resolution in living cells. Over the past two decades, super-resolution microscopy (also called 'nanoscopy') has emerged as a powerful tool for the visualization of cellular structures with nanoscale resolution[1–5]. The efficiency of nanoscopy; however, is limited by the fuel—the dyes and other chemical tools that support the vast lists of requirements for stimulated emission depletion (STED) and single molecule localization microcopy (SMLM)[6–11]. Rhodamine and its derivatives, carborhodamine (CR) and silicon rhodamine (SiR), have been shown to exhibit many promising characteristics for live-cell super-resolution microscopy, such as cell-permeability[8,12–32], photostability[8,12–32], fluorogenicity[8,11–13,16,17,22], and spontaneous blinking[17,21,26,33,34]. More importantly, recent studies have demonstrated that these fluorophores are blank canvases, enabling dramatic improvements to each of these characteristics via strategic chemical substitution.

Work in the Schepartz lab takes advantage of the versatility of triarylmethane fluorophores via the development of chemical tools known as high density environmentally sensitive (HIDE) probes[30] that enable nanoscale visualization of cellular targets, including the endoplasmic reticulum[21,27], Golgi apparatus[32], mitochondria[21,27], plasma membrane[21,27,29] and endocytic machinery[28] in multiple colors and over long time periods. The work described in this dissertstion leverages synthetic chemistry and chemical biology to develop next generation HIDE probes with enhanced functions that will help to push the frontiers of biology and medicine.

This chapter serves to lay the groundwork for the analyses described in subsequent chapters. The next several paragraphs provide an in-depth analysis of the concepts most relevant to this dissertation, before introducing the objectives of subsequent chapters.

1.2 Super-resolution Microscopy

1.2.1 Abbe Diffraction Limit

The Abbe diffraction limit defines the maximum obtainable optical resolution of a far-field microscope as roughly between half to a third of the wavelength of light emitted by a point-like fluorescence emitte[35–37]. More specifically:

$$d = \frac{\lambda}{2NA}$$

where *d* is the minimum distance between the centroids of two resolvable signals, λ is the emitted wavelength and *NA* is the numerical aperture of the lens collecting light from the sample. Pioneering work over the past few decades has demonstrated that this diffraction limit can be superseded via temporal separation of otherwise spatially overlapping signals (i.e., each signal within a diffraction limited region distributing along a time axis) [1–5]. While even an individualized point-like emitter would display a diffraction-limited fluorescence signal, by coupling the fluorescence event to a metric that can be computed to a precision

greater than the diffraction limit, resolutions far greater than those obtained via conventional microscopy methods can be accessed. Strategies for achieving this are collectively termed super-resolution microscopy or nanoscopy and can be broadly grouped into two categories—coordinated and stochastic.

1.2.2 STED nanoscopy

Coordinated methods such as stimulated emission depletion (STED) rely on point-scanning arrays. In this case, the coordinate of the laser point in the sample plane is known to a precision greater than the diffraction limit[1,2,38]. In STED, this precision is leveraged via a patterned depletion laser, which is collated with the excitation laser and prevents fluorescence from all positions, except for a zero point. Because the coordinates of this scanning zero-point are well-defined, by increasing the probability that any detectable signal originates from this center point, the resolution can be dramatically enhanced. The resolution in a STED nanoscope is therefore defined as

$$d = \frac{\lambda}{2NA\sqrt{1 + \frac{I}{I_{sat}}}}$$

where I is the intracavity intensity and I_{sat} is the saturation intensity [1,2,38]. In other words, the greater the intracavity intensity of the STED laser, the greater the probability a signal must originate from the centroid, and accordingly the greater the achievable resolution. By scanning the collated excitation and depletion lasers through the sample, an image with resolution far higher than the diffraction limit can be acquired.

1.2.3 Single Molecule Localization Microscopy

Stochastic methods such as single molecule localization microscopy (SMLM) function by controlling the sample and imaging conditions such that the average distance between any two fluorescence emitters in a controlled 'ON state' is greater than Abbe diffraction limit. Accordingly, at any point *t*, a series of dispersed diffraction patterns from individualized fluorescence emitters can be collected on the camera. These patterns can then be fit to a known function, most commonly a three-dimensional Gaussian[39]. Because the center of this new function can be determined with a precision far greater than the diffraction limit, a super-resolution image can be determined. The more precisely the centroid can be determined, the greater the resolution. Accordingly, the resolution of SMLM fit via a 3D Gaussian is typically defined as

$$d = \frac{\lambda}{2NA\sqrt{N}}$$

where N is the number of photons collected from the fluorescence emitter. In other words, the more data is collected from an emitter, the greater its centroid can be determined

when fit to a three-dimensional Gaussian. By collecting several frames from fluorescence emitters separated by an average distance greater than the diffraction limit, each emitter in the sample can be imaged, enabling a super-resolution image to be reconstructed[3,4].

1.3 Fluorophores for Super-resolution Microscopy

1.3.1 Fluorophores for STED

Specialized fluorophores are required to enable both coordinated and stochastic super-resolution microscopy techniques [6–11]. This is because in both cases, information from the sample plane is manipulated to generate diffraction-unlimited information. STED is dependent upon an inverted fluorophore population, meaning each emitter in the sample must be excited and depleted through several cycles to acquire a super-resolution image[11,36]. This means that fluorophores excited in a STED nanoscope will spend a much greater amount of time in the high energy S_1 state when compared to fluorophores excited via conventional methods, or even via SMLM. This will also mean that during STED, fluorophores are more likely to undergo intersystem crossing to the long-lived triplet state, which can react with triplet oxygen and other species to chemically modify the fluorophore. This process is known as photobleaching[40–42] and decreases the overall population of available fluorophores, leading to irreversible loss of signal. Fluorophores designed for STED must therefore be highly photostable, meaning even their high energy states are resistant to reaction. Red and near-IR absorbing and emitting fluorophores have smaller energy differences between their ground and excited states and are therefore generally more photostable (i.e., amenable to STED). Other modifications, such as addition of electron-withdrawing fluorine substituents can decrease the propensity for single electron transfer (SET) from the excited state fluorophore to acceptors like triplet oxygen[22,26,43].

1.3.2 Fluorophores for SMLM

While fluorophores for SMLM need not face the same degree of optical stress as fluorophores utilized for STED, they have the additional requirement of needing to be reversibly converted between ‘ON’ and ‘OFF’ states[7,8]. Since most small molecule fluorophores are organic compounds with highly conjugated structures, generation of the OFF-state, typically involves truncation of the pi system in order to render the molecule irresponsive to the excitation source[5,6,33,44]. The pi systems of many small molecule fluorophores typically possess internal olefins that are conjugated either 1,4 or 1,6 to electrophilic moieties such as ketones or iminium ions. These electrophilic sites are labile to conjugate addition from either external or internal nucleophiles, resulting in the necessary disruption of the pi system. The nucleophile must also serve as a good leaving group, such that a thermal equilibrium can be generated between the ‘ON’ and ‘OFF’ states of the fluorophore. The position of this equilibrium can then be tuned to ensure that the average distance between any two molecules in the ‘ON’ state is greater than the Abbe diffraction limit.

1.4 Silicon Rhodamine Fluorophores

1.4.1 *Introduction to Si-rhodamines*

One class of fluorophores known as Si-rhodamines[12,45] are particularly well-suited to live cell super-resolution microscopy. This is because Si-rhodamines are cell-permeant [8,12–32], photostable [8,12–32] and absorb and emit in the near-IR [8,12–32], a region of the electromagnetic spectrum well-suited to live cell imaging[46]. In addition, Si-rhodamines exist in equilibrium between closed, non-fluorescent and open, fluorescent due to an internal nucleophile that enables an intramolecular spirocyclization reaction[12,33]. Finally, each of the properties of Si-rhodamine can be fine-tuned via simple chemical modification to the fluorophore's core structure. For these reasons, Si-rhodamines are fantastic tools for both STED and SMLM.

1.4.2 Si-rhodamines for STED

Generally, Si-rhodamines utilized for STED possess a carboxylate at the 2'-position[12,14,17,22,24,43,47], making the primary fluorescent form of the molecule a zwitterion. The 2'-carboxylte is an ample nucleophile, meaning the fluorophore can readily occupy its closed lactone form. This form of the molecule is uncharged and accordingly highly cell-permeant. Furthermore, because this form of the molecule is nonfluorescent, it confers fluorogenicity on to the molecule: Si-rhodamines generally self-aggregate in aqueous solution, leading to self-solubilization into a hydrophobic environment where the lactone is enriched[12]. Upon binding its target however, the fluorophore is individualized and becomes fluorescent again. The flagship Si-rhodamine, carboxy-SiR[12] was reported by Kai Johnsson in 2014, and has seen extensive use for super-resolution microscopy. Since then, a wide variety of Si-rhodamines have been developed and utilized for live and fixed cell STED[12,14,17,22,24,43,47].

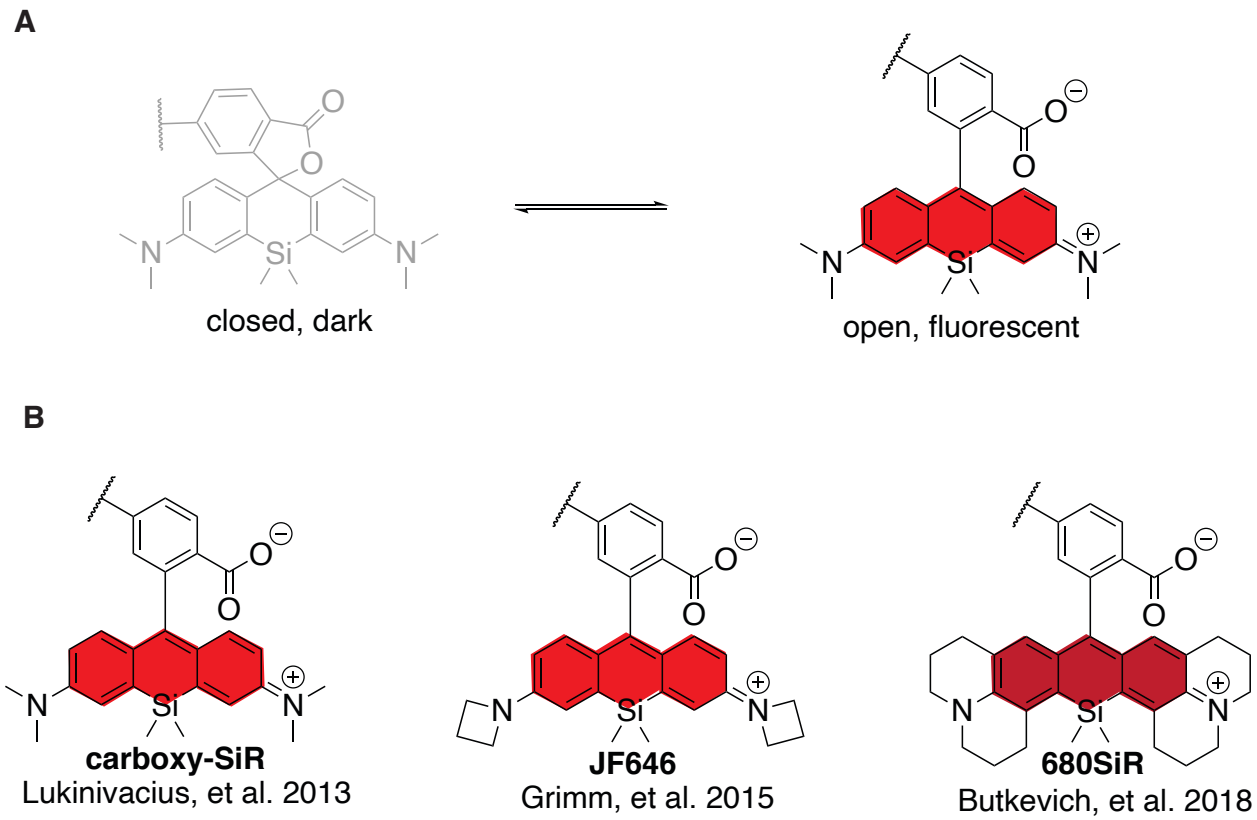

Figure 1.1 Si-rhodamines for STED. (A) Thermal equilibrium between closed, dark and open, fluorescent of Si-rhodamine fluorophores. (B) Examples of STED-compatible Si-rhodamine fluorophores.

1.4.3 Si-rhodamines for SMLM

Most conventional fluorophores for SMLM require the addition of external nucleophiles to achieve the requisite conversion between 'ON' and 'OFF' states[6]. Since many of these fluorophores react with nucleophiles in the triplet state, additional additives to stabilize that state are required. To increase specificity, oxygen depletion system must often be employed as well[7]. Because Si-rhodamines possess internal nucleophiles, if this nucleophile is sufficiently strong, one can enable conversion between 'ON' and 'OFF' states reliably without addition of external additives. These molecules, termed spontaneously blinking fluorophores (SBF)[17,26,33,34], typically trade in the 2'-carboxy substituent for a 2'-hydroxymethyl—a small percentage of which will exist as the highly nucleophilic alkoxide. The flagship SBF hydroxymethyl Si-rhodamine (HMSiR), developed and reported by Urano in 2014[33], interconverts between its 'ON' and 'OFF' states as a result of a ground state thermal equilibrium and can therefore enable live cell SMLM in near-physiological condition (i.e., in the absence of chemical additives)[21,26,33].

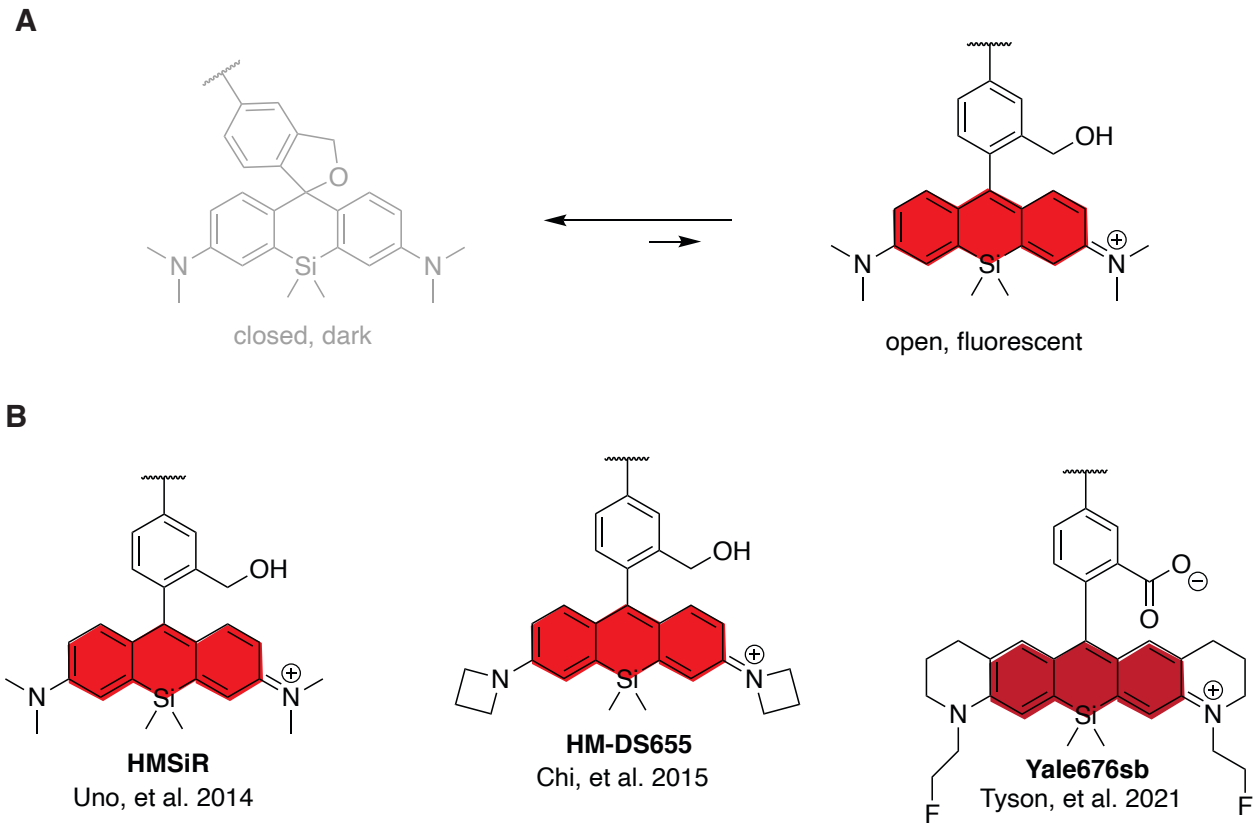

Figure 1.2 Si-rhodamines for SMLM. (A) Thermal equilibrium between closed, dark and open, fluorescent of spontaneously blinking Si-rhodamine fluorophores. (B) Examples of SMLM-compatible Si-rhodamine fluorophores.

1.5 HIDE Probes

Our lab has leveraged the properties of Si-rhodamine fluorophores to develop a class of dual-component chemical tools known as high density environmentally sensitive (HIDE) probes[30]. HIDE probes rely on three inherent technologies: 1) photostable and environmentally sensitive Si-rhodamine fluorophores[12,27,33], 2) synthetic lipids that specifically accumulate within organelle membranes of interest[21,28,32] and 3) bioorthogonal chemical ligations[48–50] that serve to combine the fluorophore and synthetic lipid *in situ*, accordingly localizing the fluorophore to an organelle membrane at high density. In the hydrophobic environment of intracellular organelle membranes, the equilibrium of carboxy-SiR and HMSiR are pushed heavily to favor their closed, neutral forms. These ultra-low on values; however, are offset by the high density at which the lipid-labeling strategy enables the fluorophore to pack within the organelle membrane[21,30]. The result is that at any given time, only a small fraction of the fluorophore population is being imaged. The large reservoir of unresponsive fluorophore can slowly equilibrate to the open form, allowing extremely long time-lapse nanoscopy to be performed in live cells.

HIDE probes enable live cell dynamics to be followed in cells for orders of magnitude longer than cells labeled via conventional protein tags, such as HaloTag[21,27–29].

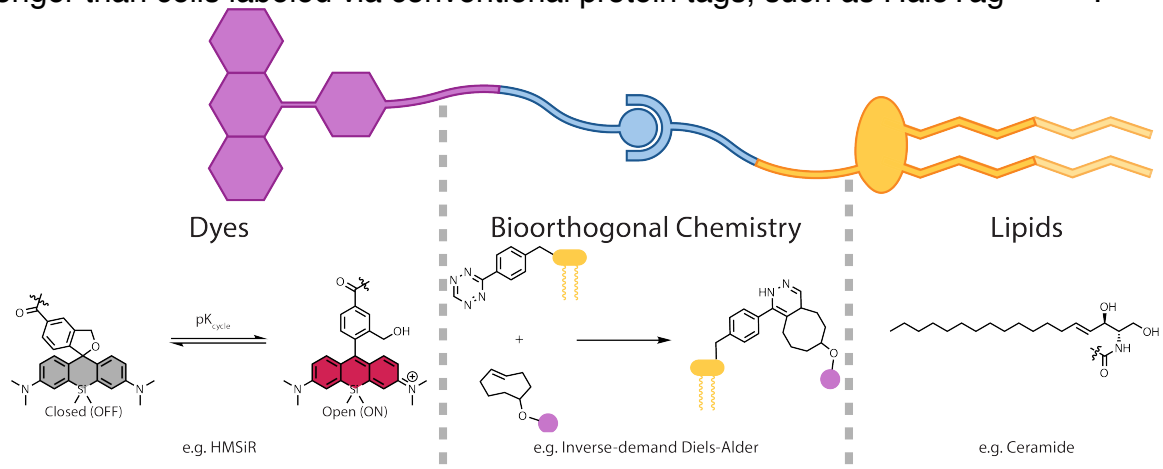

Figure 1.3 HIDE probes are multicomponent chemical tools. HIDE probes leverage three primary technologies: 1) photostable and environmentally sensitive Si-rhodamine fluorophores[12,27,33], 2) synthetic lipids that specifically accumulate within organelle membranes of interest[21,28,32] and 3) bioorthogonal chemical ligations[48–50] that serve to combine the fluorophore and synthetic lipid *in situ.*

1.6 Outlook

This dissertation describes work performed during my graduate studies that have enabled an expansion of the HIDE probe toolkit. Chapter 2 describes the first example of multicolor STED nanoscopy using HIDE probes. This was made possible via the optimization of a mutually orthogonal biorthogonal labeling strategy, as well as the development of a novel STED-compatible carborhodamine that is spectrally distinct from carboxy-SiR. Chapter 3 describes the development of the brightest reported nanoscopy-compatible Si-rhodamine, Yale676sb. This molecule is accessed via a novel design strategy and can partner with HMSiR to enable two-color live cell SMLM with only a single 642 nm laser. The final chapter of the dissertation, Chapter 4, describes a series of experiments designed but not fully implemented during my time in the Schepartz lab. These experiments build upon the work described herein to generate even more powerful fluorophores and even more robust labeling modalities.

1.7 References

1. Hell, S. W. Subdiffraction resolution in far-field fluorescence microscopy. 1 3 (1999).

2. Klar, T. A., Jakobs, S., Dyba, M., Egner, A. & Hell, S. W. Fluorescence microscopy with diffraction resolution barrier broken by stimulated emission. *Proc National Acad Sci* 97, 8206–8210 (2000).

3. Rust, M. J., Bates, M. & Zhuang, X. Sub-diffraction-limit imaging by stochastic optical reconstruction microscopy (STORM). *Nat Methods* 3, 793 796 (2006).

4. Betzig, E., Hess, H. F. & Lippincott-Schwartz, J. Imaging Intracellular Fluorescent Proteins at Nanometer Resolution. *Science* 313, 1638 1642 (2006).

5. Heilemann, M. *et al.* Subdiffraction-Resolution Fluorescence Imaging with Conventional Fluorescent Probes. *Angewandte Chemie Int Ed* 47, 6172–6176 (2008).

6. Dempsey, G. T., Vaughan, J. C., Chen, K. H., Bates, M. & Zhuang, X. Evaluation of fluorophores for optimal performance in localization-based super-resolution imaging. *Nat Methods* 8, 1027 1036 (2011).

7. Li, H. & Vaughan, J. C. Switchable Fluorophores for Single-Molecule Localization Microscopy. *Chem Rev* 118, 9412 9454 (2018).

8. Jradi, F. M. & Lavis, L. D. Photosensitive fluorophores for single-molecule localization microscopy. *ACS Chemical Biology* (2019) doi:10.1021/acschembio.9b00197.

9. Lavis, L. D. & Raines, R. T. Bright Building Blocks for Chemical Biology. *Acs Chem Biol* 9, 855 866 (2014).

10. Lavis, L. D. Teaching Old Dyes New Tricks: Biological Probes Built from Fluoresceins and Rhodamines. *Annu Rev Biochem* 86, 825 843 (2017).

11. Wang, L., Frei, M. S., Salim, A. & Johnsson, K. Small-Molecule Fluorescent Probes for Live-Cell Super-Resolution Microscopy. *J Am Chem Soc* 141, 1 12 (2018).

12. Lukinavičius, G. *et al.* A near-infrared fluorophore for live-cell super-resolution microscopy of cellular proteins. *Nat Chem* 5, 1 8 (2012).

13. Lukinavičius, G. *et al.* Fluorogenic Probes for Multicolor Imaging in Living Cells. *J Am Chem Soc* 138, 9365–9368 (2016).

14. Butkevich, A. N. *et al.* Two-Color 810 nm STED Nanoscopy of Living Cells with Endogenous SNAP-Tagged Fusion Proteins. *Acs Chem Biol* 13, acschembio.7b00616 6 (2017).

15. Butkevich, A. N., Lukinavičius, G., D'Este, E. & Hell, S. W. Cell-Permeant Large Stokes Shift Dyes for Transfection-Free Multicolor Nanoscopy. *J Am Chem Soc* 139, jacs.7b06412 4 (2017).

16. Butkevich, A. N. *et al.* Fluorescent Rhodamines and Fluorogenic Carbopyronines for Super-Resolution STED Microscopy in Living Cells. *Angewandte Chemie Int Ed* 55, 3290–3294 (2016).

17. Zheng, Q. *et al.* Rational Design of Fluorogenic and Spontaneously Blinking Labels for Super-Resolution Imaging. *Acs Central Sci* 5, 1602–1613 (2019).

18. Grimm, J. B. *et al.* A general method to optimize and functionalize red-shifted rhodamine dyes. *Nat Methods* 17, 815–821 (2020).

19. Grimm, J. B. *et al.* A General Method to Improve Fluorophores Using Deuterated Auxochromes. *Jacs Au* (2021) doi:10.1021/jacsau.1c00006.

20. Grimm, J. B. *et al.* Optimization and functionalization of red-shifted rhodamine dyes. *Biorxiv* 2019.12.20.881227 (2019) doi:10.1101/2019.12.20.881227.

21. Takakura, H. *et al.* Long time-lapse nanoscopy with spontaneously blinking membrane probes. *Nat Biotechnol* 35, 773 780 (2017).

22. Grimm, J. B. *et al.* A general method to fine-tune fluorophores for live-cell and in vivo imaging. *Nat Methods* 14, e04236 14 (2017).

23. Zhou, X., Lai, R., Beck, J. R., Li, H. & Stains, C. I. Nebraska Red: a phosphinate-based near-infrared fluorophore scaffold for chemical biology applications. *Chem Commun* 52, 12290–12293 (2016).

24. Grimm, J. B. *et al.* A general method to improve fluorophores for live-cell and single-molecule microscopy. *Nat Methods* 12, 244 250 (2015).

25. Grimm, J. B. *et al.* Carbofluoresceins and Carborhodamines as Scaffolds for High-Contrast Fluorogenic Probes. *Acs Chem Biol* 8, 1303–1310 (2013).

26. Tyson, J. *et al.* Extremely Bright, Near-IR Emitting Spontaneously Blinking Fluorophores Enable Ratiometric Multicolor Nanoscopy in Live Cells. *Acs Central Sci* (2021) doi:10.1021/acscentsci.1c00670.

27. Chu, L. *et al.* Two-color nanoscopy of organelles for extended times with HIDE probes. *Nature Communications* 11, (2020).

28. Gupta, A., Rivera-Molina, F., Xi, Z., Toomre, D. & Schepartz, A. Endosome motility defects revealed at super-resolution in live cells using HIDE probes. *Nat Chem Biol* 1–7 (2020) doi:10.1038/s41589-020-0479-z.

29. Thompson, A. D. *et al.* Long-Term Live-Cell STED Nanoscopy of Primary and Cultured Cells with the Plasma Membrane HIDE Probe DiI-SiR. *Angewandte Chemie Int Ed* 56, 10408–10412 (2017).

30. Thompson, A. D., Bewersdorf, J., Toomre, D. & Schepartz, A. HIDE Probes: A New Toolkit for Visualizing Organelle Dynamics, Longer and at Super-Resolution. *Biochemistry-us* 56, acs.biochem.7b00545 8 (2017).

31. Bottanelli, F. *et al.* Two-colour live-cell nanoscale imaging of intracellular targets. *Nat Commun* 7, 1 5 (2016).

32. Erdmann, R. S. *et al.* Super-Resolution Imaging of the Golgi in Live Cells with a Bioorthogonal Ceramide Probe. *Angewandte Chemie Int Ed* 53, 10242 10246 (2014).

33. Uno, S. *et al.* A spontaneously blinking fluorophore based on intramolecular spirocyclization for live-cell super-resolution imaging. *Nat Chem* 6, 681 689 (2014).

34. Uno, S., Kamiya, M., Morozumi, A. & Urano, Y. A green-light-emitting, spontaneously blinking fluorophore based on intramolecular spirocyclization for dual-colour super-resolution imaging. *Chem Commun* 54, 102–105 (2017).

35. Toomre, D. & Bewersdorf, J. A New Wave of Cellular Imaging. *Annu Rev Cell Dev Bi* 26, 285–314 (2010).

36. Sahl, S. J., Hell, S. W. & Jakobs, S. Fluorescence nanoscopy in cell biology. *Nat Rev Mol Cell Bio* 18, 685 701 (2017).

37. Schermelleh, L. *et al.* Super-resolution microscopy demystified. *Nat Cell Biol* 21, 1 13 (2018).

38. Hell, S. W. Ground-state-depletion fluorscence microscopy: A concept for breaking the diffraction resolution limit. 1 3 (1995).

39. Sage, D. *et al.* Super-resolution fight club: assessment of 2D and 3D single-molecule localization microscopy software. *Nat Methods* 16, 1 14 (2019).

40. Eggeling, C., Widengren, J., Rigler, R. & Seidel, C. A. M. Photobleaching of Fluorescent Dyes under Conditions Used for Single-Molecule Detection: Evidence of Two-Step Photolysis. *Anal Chem* 70, 2651 2659 (1998).

41. Tasso, T. T. *et al.* Photobleaching Efficiency Parallels the Enhancement of Membrane Damage for Porphyrazine Photosensitizers. *Journal of the American Chemical Society* (2019) doi:10.1021/jacs.9b05991.

42. Wang, C. *et al.* Super-Photostable Phosphole-Based Dye for Multiple-Acquisition Stimulated Emission Depletion Imaging. *J Am Chem Soc* 139, jacs.7b04418 8 (2017).

43. Grimm, J. B., Brown, T. A., Tkachuk, A. N. & Lavis, L. D. General Synthetic Method for Si-Fluoresceins and Si-Rhodamines. *Acs Central Sci* 3, acscentsci.7b00247 11 (2017).

44. Vaughan, J. C., Dempsey, G. T., Sun, E. & Zhuang, X. Phosphine Quenching of Cyanine Dyes as a Versatile Tool for Fluorescence Microscopy. *J Am Chem Soc* 135, 1197 1200 (2013).

45. Koide, Y., Urano, Y., Hanaoka, K., Terai, T. & Nagano, T. Evolution of Group 14 Rhodamines as Platforms for Near-Infrared Fluorescence Probes Utilizing Photoinduced Electron Transfer. *Acs Chem Biol* 6, 600 608 (2011).

46. Light-induced cell damage in live-cell super-resolution microscopy. *Sci Rep-uk* 5, 1 12 (2015).

47. Lukinavičius, G., Johnsson, K., Hell, S. W. & Urano, Y. Fluorogenic Probes for Multicolor Imaging in Living Cells. 1 4 (2016) doi:10.1021/jacs.6b04782/suppl_file/ja6b04782_si_002.pdf.

48. Agard, N. J., Prescher, J. A. & Bertozzi, C. R. A Strain-Promoted [3 + 2] Azide?Alkyne Cycloaddition for Covalent Modification of Biomolecules in Living Systems. *J Am Chem Soc* 126, 15046 15047 (2004).

49. Debets, M. F. *et al.* Aza -dibenzocyclooctynes for fast and efficient enzyme PEGylation via copper-free (3+2) cycloaddition. *Chem Commun* 46, 97–99 (2010).

50. Blackman, M. L., Royzen, M. & Fox, J. M. Tetrazine Ligation: Fast Bioconjugation Based on Inverse-Electron-Demand Diels–Alder Reactivity. *J Am Chem Soc* 130, 13518–13519 (2008).

Chapter 2. Two-color nanoscopy of organelles for extended times with HIDE probes

This chapters details a series of experiments that serve to expand HIDE probes to enable multicolor imaging in live cells via stimulated emission depletion (STED) nanoscopy. Two-color STED of organelles for extended time periods is enabled via two primary achievements: 1) the optimization of a mutually orthogonal bioorthogonal labeling strategy that leverages tetrazine, trans-cyclooctene, azide and dibenzocyclooctene and 2) the development of the novel photostable and red-emitting carborhodamine Yale595, which is demonstrated to have superior performance for live cell STED when compared to existing fluorophores. HIDE probes based on these new tools are non-toxic and cell-permeant, therefore facilitating multicolor STED in primary and difficult to transfect cell lines. This article was published as an article and is reproduced with permission: *Chu, L., Tyson, J., Shaw, J.E. et al. Two-color nanoscopy of organelles for extended times with HIDE probes.Nat Commun* ***11,*** *4271 (2020). https://doi.org/10.1038/s41467-020-17859-1*

2.1 Introduction

Super-resolution microscopy ('nanoscopy') can visualize cellular components with resolutions as high as ~10 nanometers, far below the Abbe diffraction limit[1]. When combined with multi-color labeling strategies, nanoscopy can reveal key features of organelle structure and interactions that are hidden when visualized using diffraction-limited approaches[2,3]. However, visualizing organelle *dynamics* at super-resolution remains challenging because even the most photostable fluorophores bleach within tens to hundreds of seconds under conditions required for stimulated emission depletion (STED) or single molecule localization microscopy (SMLM)[4].

Previously, we reported a set of high-density environmentally sensitive (HIDE) probes that support long time-lapse, single-color nanoscopy of organelles including the ER, mitochondria, Golgi apparatus, and plasma membrane (PM)[5-7]. HIDE probes consist of an organelle-specific lipid or lipid-like small molecule with a reactive *trans*-cyclooctene (TCO) moiety and a silicon rhodamine-tetrazine (SiR-Tz)[8] reaction partner. These two components undergo a rapid, *in situ* tetrazine ligation reaction[9,10] that localizes the SiR dye at high density within the organelle membrane. In this environment, HIDE probes support the acquisition of continuous SMS and STED super-resolution movies in standard culture media (no redox chemicals) exceeding 25 mins - approximately 50-fold longer than when the identical fluorophore is linked to an organelle-resident protein[7]. Here we describe innovations that enable live-cell HIDE imaging of two different organelles in two colors for extended times using STED (Fig. 1a). The ~50 nm per axis resolution achieved here (Fig. 2) significantly exceeds the ~100 nm resolution obtained when using structured illumination[11] or lattice light-sheet microscopy[12].

2.2 Results

2.2.1 HIDE probes assembled via SPAAC support long time-lapse live-cell nanoscopy

Two-color, live-cell HIDE nanoscopy demands not only two organelle-specific small molecules and a second photostable fluorophore but also a second conjugation reaction that is orthogonal to the tetrazine ligation and proceeds rapidly to completion within live cells. We were drawn to the strain-promoted azide-alkyne cycloaddition reaction (SPAAC)[13] between an azide and a dibenzoazacyclooctyne (DBCO) as it is live-cell compatible and reacts rapidly enough (k = 0.31 $M^{-1}s^{-1}$)[14] to ensure complete reaction using reagents at micromolar concentrations.

To confirm that a SPAAC-assembled HIDE probe would localize as expected, DiI-N_3 and SiR-DBCO were synthesized (Supplementary Information, Fig. 1b, Supplementary Fig. 1a), added sequentially to HeLa cells, incubated 30 minutes to generate DiI-SiR and imaged by confocal microscopy. Under these conditions, DiI-SiR colocalized extensively with a bona fide PM marker, VAMP2-pH (PCC = 0.63 ± 0.06); no colocalization was observed when cells were incubated with SiR-DBCO in absence of DiI-N_3 (PCC = 0.29 ±

0.03) (Fig. 1c lower middle panel, Supplementary Fig. 2). As observed previously[5], the HIDE probe DiI-SiR must be assembled in two steps, as cells treated with the pre-assembled reaction product DiI-SiR (Supplementary Fig. 1a) showed no PM labeling in SiR channel (Supplementary Fig. 3).

To test whether a HIDE probe assembled using SPAAC would support prolonged STED nanoscopy, we treated HeLa cells, under optimized conditions (Supplementary Fig. 4), with 10 μM DiI-N_3 and 2 μM SiR-DBCO. We imaged the cells continuously by STED for 20 minutes at 0.5 Hz and monitored plasma membrane (PM) fluorescence over time (Supplementary Movie 1). Both the initial fluorescence intensity (Supplementary Fig. 5a) and bleaching half-life (Fig. 1d and Supplementary Fig. 5b) of the HIDE probe generated from DiI-N_3 and SiR-DBCO were virtually identical to those measured using DiI-TCO and SiR-Tz (bleaching half-life 62.9±1.4 vs 65.9±0.6). The similarity of these values confirms that HIDE probes assembled using SPAAC support prolonged STED imaging; the small difference in structure due to alternative linker chemistry has no apparent effect on SiR photostability. In contrast, STED images generated using the Smo-Halo/SiR-CA combination bleached within 1 minute when visualized by STED (Fig. 1d, black trace). Additionally, fluorescence recovery after photobleaching (FRAP) experiment support that the dramatic difference in photostability between Smo-Halo/SiR-CA and DiI-TCO/SiR-Tz is not due to diffusion dynamics, as we observed similar diffusion kinetics of recovery with protein and lipid labeling strategies; 10.9±4.5 versus 10.3±1.3 seconds, respectfully (Supplementary Fig. 6a). While the HIDE probes had a marginally higher mobile fraction (25%) this increase cannot account for the ~40-fold increased resistance of HIDE probes to photobleaching. As an additional control the bleaching recovery kinetics of an independent lipid dye (Laurdan) were virtually identical in control cells to those labeled with DiI-TCO/SiR-Tz supporting that the HIDE probe labeling causes no general changes in plasma membrane fluidity (Supplementary Fig. 6b).

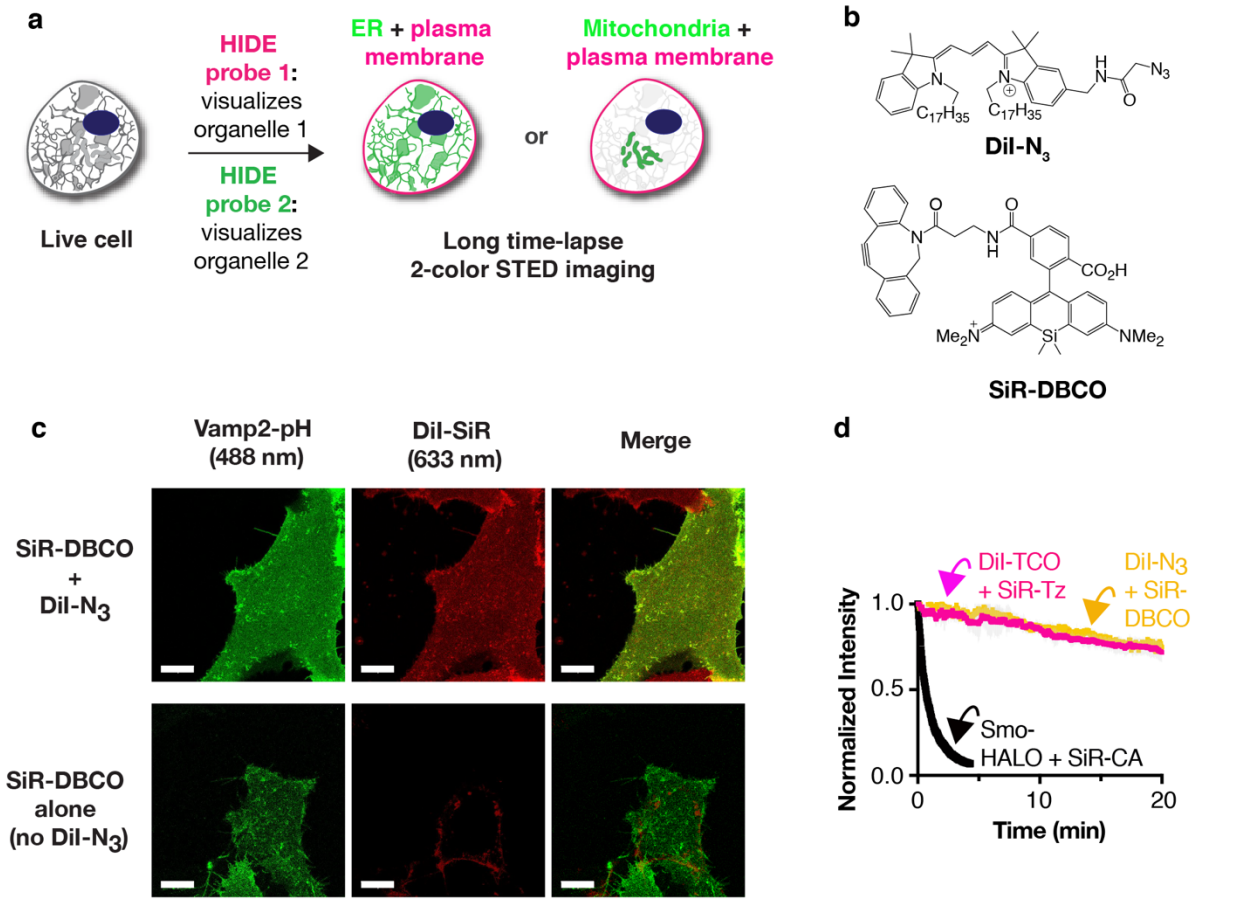

Figure 1 Development of two-color high-density environment-sensitive (HIDE) probes. (**a**) HIDE probes enable long time-lapse two-color STED imaging. (**b**) Chemical structures of DiI-N_3 and SiR-DBCO. (**c**) Top: Images of DiI-SiR (633 nm) colocalizes with plasma membrane marker Vamp2-pH (488 nm). Bottom: HeLa cells transciently expressing Vamp2-pH was incubated with 2 µM SiR-DBCO for 30 min at 37 °C then imaged under a spinning disk confocal microscope. When DiI-N_3 was not added, SiR-DBCO (633 nm) did not colocalize with Vamp2-pH (488 nm). Scale bar: 10 µm (**d**) Plot illustrating normalized fluorescence intensity of Smo-HALO+SiR-CA (black), DiI-TCO+SiR-Tz (red) and DiI-N_3+SiR-DBCO (yellow) over time (mean±SD, n = 3 ROI, N = 1 cell).

2.2.1 Development and Evaluation of Yale595

Next, we sought to identify a STED-appropriate fluorophore that would be compatible with SiR to enable two-color HIDE nanoscopy. The ideal second fluorophore should be: (1) membrane-permeant; (2) non-toxic; (3) highly photostable; and (4) spectrally separable from SiR. We first evaluated four previously reported fluorophores: 580CP[15], Atto590[16, 17], JF585[18], and SiR700[19] (Supplementary Fig. 7). HeLa cells were treated with 10 μM DiI-TCO followed by 2 μM of either 580CP-Tz, Atto590-Tz, JF585-Tz, or SiR700-Tz (Supplementary Information) then imaged by STED at 0.5 Hz. None of these previously reported fluorophores were suitable. Visual inspection and time-dependent quantification of PM fluorescence revealed that the HIDE probes generated from DiI-TCO and either CP580-Tz or SiR700-Tz bleached considerably more rapidly than that generated using SiR-Tz (Fig. 2a,b, Supplementary Fig. 8; Supplementary Movie 2); further the HIDE probe generated from DiI-TCO and SiR700-Tz was also dimmer (Supplementary Fig. 8d; Supplementary Movie 3). Of note, the HIDE probe generated from DiI-TCO and Atto590-Tz was acutely cytotoxic (Supplementary Movie 4, Fig. 8a and e), while that generated from DiI-TCO and JF585-Tz was extremely dim (Supplementary Fig. 8b and d). Strikingly, all PM-localized HIDE probes generated here could be imaged for an order of magnitude longer then a PM-localized protein Smo-Halo/SiR-CA (Supplementary Movie5).

We were intrigued by the poor performance of the HIDE probe generated from DiI-TCO and JF585-Tz, as this fluorophore performs well when used to label a membrane resident protein[18]. We hypothesized that this difference reflected a shift in the equilibrium between the open (ON) and closed (OFF) states of this dye in the two environments: JF-585 performs well when attached to a membrane protein because it is mainly ON in a polar, aqueous environment, but poorly as a HIDE probe because it is mainly OFF in the lipid environment. A plot of JF585 emission as a function of the percent water in a water/dioxane mixture is consistent with this hypothesis; the midpoint of the transition occurs at approximately 91% water (Fig. 2d). We reasoned that a tetrazine derivative of JF585 in which the 3,3-difluoroazetidine ring[20] is replaced with a less electrophilic 3-fluoroazetidine ring to form 3-fluorazetidine carborhodamine would display a higher ON fraction in the lipid environment and thereby facilitate STED imaging. We synthesized tetrazine fluorazetidine carborhodamine (see Supplementary Information) which we named Yale595 to reflect its origin and slight red spectral maximum excitation shift (Supplementary Fig. 9). The excitation and emission spectra of Yale595-CO_2H are compatible with SiR for two-color imaging (Supplementary Fig. 9). As anticipated, a plot of Yale595 emission as a function of the percent water in a water/dioxane mixture was shifted, with a midpoint at ~75% water (Fig. 2d). Moreover, the apparent photostabilities of HIDE probes generated from DiI-TCO and Yale595-Tz or DiI-TCO and SiR-Tz were similar (Fig. 2a, b, Supplementary Fig. 8, 10a, b and Supplementary Movie 6). To further validate the utility of Yale595 in cells, we generated an ER-specific HIDE probe from Cer-TCO[5] and Yale595-Tz (Supplementary Fig. 1b). This probe colocalized with Sec61□-GFP (Supplementary Fig. 10c and d) and when visualized using STED could resolve individual ER tubules with a full width half-maximum (FWHM) of ~50 nm (Fig. 2e, f). Labeling with Cer-TCO and SiR-Tz was harder to visualize ER than with Yale595-Tz, which is likely

due to higher nonspecific binding of SiR-Tz (Supplementary Fig. 10e, f). Per the increased photostability of Yale595 we reasoned that it results from a combination of high-density labeling enabled by the lipid probe[7] and the low ON/OFF ratio of Yale595 in a hydrophobic membrane environment. Support for this concept derives from the observation of a comparable initial fluorescent intensity of cells whose ER membranes were labeled with Sec61□□SNAP/Yale595-BG and Cer-TCO/Yale595-Tz, but only cells that were labeled with Cer-TCO/Yale595-Tz strongly resisted photobleaching. These observations are consistent with a model in which the low ON/OFF ratio of Yale595 in the lipid environment establishes a pool of non-absorbing (dark) Yale595 molecules that can replenish absorbing (bright) Yale595 molecules that have been photo-bleached. Minimal crosstalk (<1%) between 561 nm and 595 nm channel was observed when PM-specific HIDE probe DiI-Yale595 or mitochondria-specific HIDE probe RhoB-Yale595 (Supplementary Fig. 1c) was imaged under the STED microscope (Supplementary Fig. 11). To optimize conditions to visualize cellular structures using Yale595 in live cells, we labeled HeLa cells with 10 μM DiI-TCO and 2 μM Yale595-Tz and imaged them by STED using different excitation power and STED depletion powers, as shown in Supplementary Fig. 12. These studies support that photostability was maximal when the excitation laser power (595 nm) was set to 10% and the depletion laser power (775 nm) was set to 30%; albeit the brightness was as expected higher using to 20% power. We thus used these conditions for live cells imaging experiments.

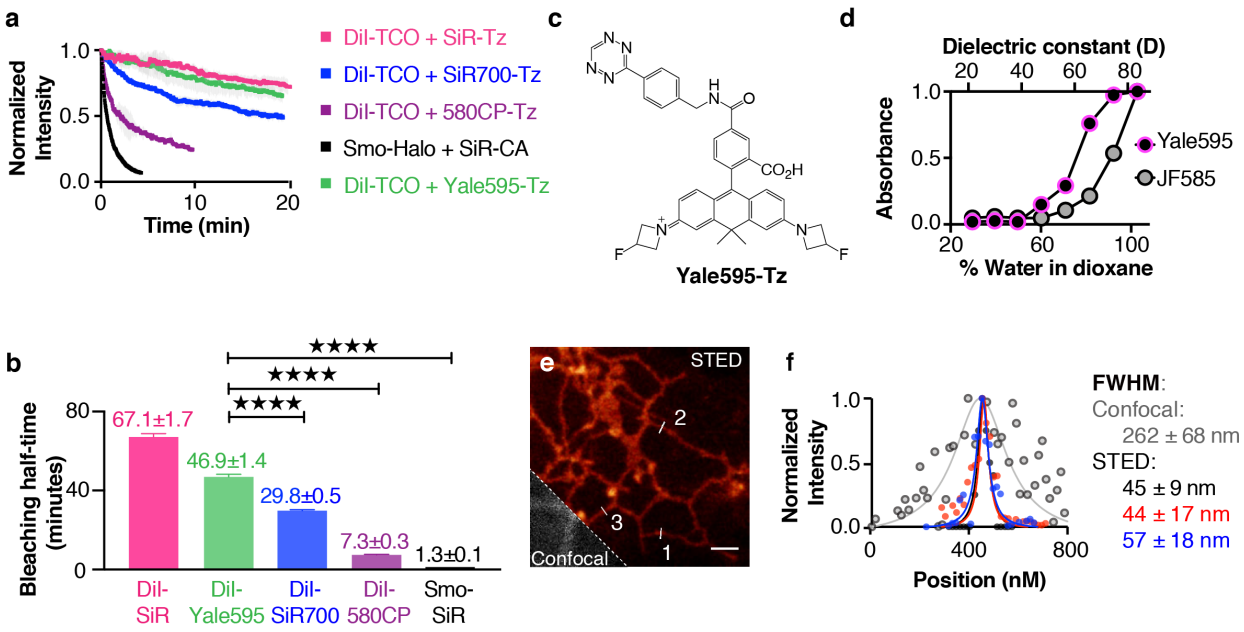

Figure 2 Development of Yale595. (**a**) Plot illustrating normalized fluorescence intensity (NI) of 580CP (purple), SiR (red), SiR700 (blue) and Yale595 (green) over time (mean±SD, n = 3 ROI, N = 1 cell). (**b**) Bleaching half-time calculated from a single exponential fit to the photobleaching curves in **c** (mean ± SD., n = 3 ROI, N = 1 cell). ****P ≤ 0.0001. (**c**) Chemical structure of Yale595-Tz. (**d**) Plot of normalized absorbance of Yale595-COOH and JF585-COOH in response to different dielectric constant, D, of dioxane-water mixtures (mean, n = 2). (**e**) STED imaging of endoplasmic reticulum of HeLa cells labeled with 2 µM Cer-TCO for 1 hr followed by 2 µM Yale595-Tz for 30 min with a confocal cutaway in gray. Scale bar: 1 µm (**f**) A plot of the fluorescence signal in the STED and confocal image as a function of position along the line profile in **e**. A fit of three line profiles from the confocal data to a Lorentzian function (grey line) provides a FWHM (mean ± SD, n = 3) of 262 ± 68 nm. Fits of three line profiles (white lines) in the STED image individually to a Lorentzian function provide FWHM values of 45 ± 9 nm, 44 ± 17 nm, and 57 ± 18 nm.

2.2.1 Long time-lapse two-color live-cell nanoscopy using HIDE probes

The ER HIDE probe generated using Yale595-Tz was then used in combination with DiI-N_3/SiR-DBCO to achieve two-color HIDE imaging of the ER and PM. HeLa cells were treated first with DiI-N_3 and Cer-TCO then with SiR-DBCO and Yale595-Tz (Fig. 3a, Supplementary Fig. 13) and imaged by STED (Supplementary Fig. 3b). High resolution images were obtained in both channels (FWHM = 72 ± 19 nm for Yale 595; 57 ± 8 nm for SiR (Fig. 3c) with cross-talk between the two channels minimized by spectral unmixing (Fig. S14). No cross-reactivity was observed when HeLa cells were labeled with Cer-TCO + Yale595-DBCO or DiI-N3 + Yale595-Tz (Supplementary Fig. 15). With the two-color HIDE probes, we observed ER tubule formation, elongation, and rearrangement as well as filopodia movement over 250 time points with no significant loss of fluorescence (Fig. 3d, e, Supplementary Movie 7). When conjugated to ER (Sec61□)- and PM (Smo)-resident proteins through Halo and SNAP tags, respectively, SiR and Yale595 bleached 15- to 40-fold faster (Fig. 3d, e, Supplementary Movie 8). The two-color HIDE strategy was easily generalized to simultaneously image the PM and mitochondria in live cells for extended times (Fig. 3f, g). Namely, HeLa cells were treated with DiI-N_3 along with the mitochondria-specific small molecule RhoB-TCO followed by SiR-DBCO and Yale595-Tz (Fig. 3f, Supplementary Fig. 16) then imaged by STED at 0.5 Hz (Fig. 3g, Supplementary Movie 9). Here the fine and rapid dynamic processes of mitochondria fission and filopodia remodeling could be observed and studied over 5 minutes with minimal photobleaching. The toxicity of two-color HIDE probes was studied by monitoring cell division events of HeLa cells. No toxicity of the probes was observed, as monitored by the number of cell division events per hour after probe treatment (Supplementary Fig. 17).

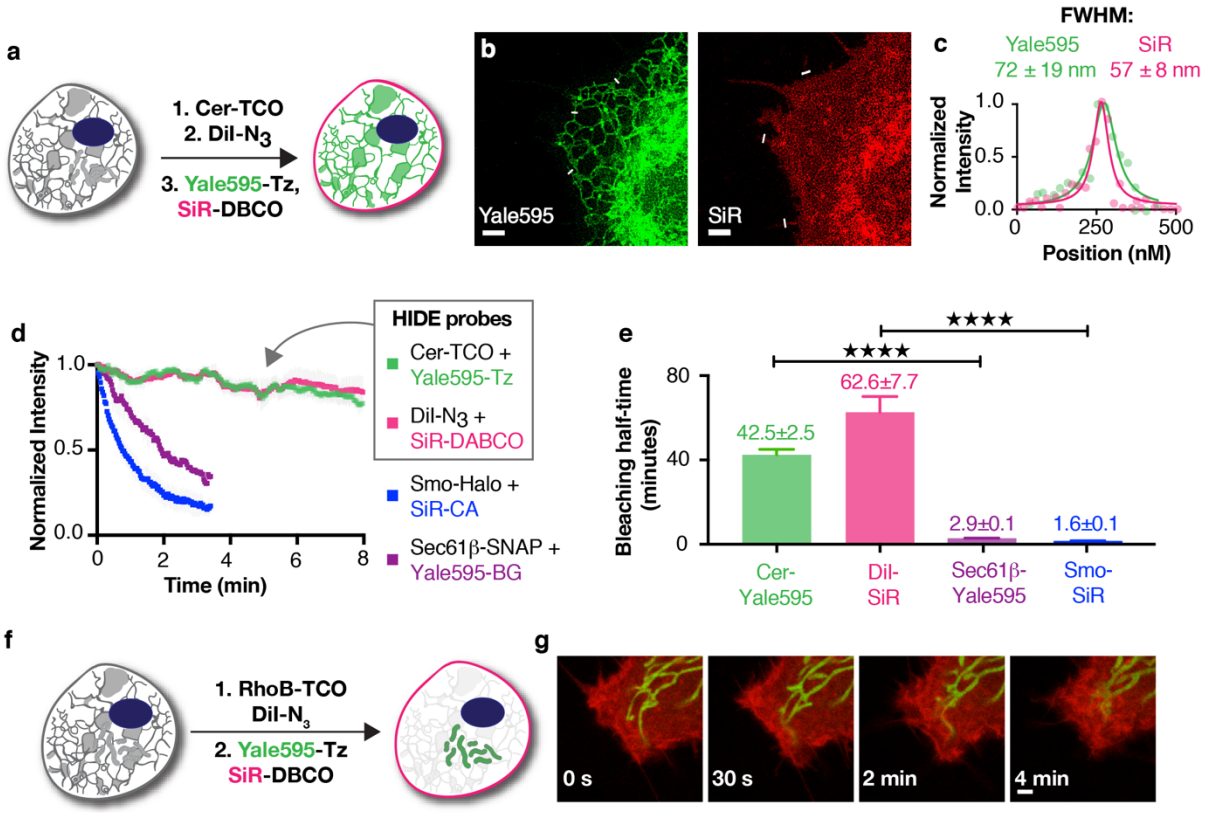

Figure 3 Long time-lapse two-color live-cell STED imaging of HeLa cells. (**a**) Schematic illustration of the three-step procedure employed to label the plasma membrane and ER. (**b**) Two-color STED image of the plasma membrane and ER of HeLa cells. Images from both channels are shown. Scale bars: 2 µm. (**c**) A plot of the fluorescence signal in the two-color STED image as a function of position along the line profile in **b**. A fit of the line profile from the Yale595 channel to a Lorentzian function (green line) provides a FWHM of 72 ± 19 nm. A fit of the line profile from the SiR channel to a Lorentzian function (red line) provides a FWHM of 57 ± 8 nm. (**d**) Plot of normalized fluorescence intensity of protein tags and HIDE probes over time (mean±SD, n = 3 ROI). The fluorescence intensity was measured in each channel separately. (**e**) τ values calculated from a single exponential fit to the photo-bleaching curves in **d** (mean ± SD., n = 3 ROI). ****P ≤ 0.0001. (**f**) Schematic illustration of the two-step procedure employed to label the plasma membrane and mitochondria. (**g**) Time course images of the plasma membrane and mitochondria. Scale bar: 2 µm.

As HIDE probes are generated from pairs of cell-permeant small molecules, they can be used to label both primary and hard-to-transfect cells[6]. To highlight this versatility, we imaged pairs of organelles in two colors by STED in three types of primary cells: human umbilical vein endothelial cells (HUVEC), mouse hippocampal neurons, and retinal pigment epithelium (RPE) cells (Fig. 4). Two-color images of the PM and ER of HUVEC cells with Cer-TCO/Yale595-Tz and DiI-N_3/SiR-DBCO revealed filopodia of one cell strikingly proximal to the ER of an adjacent cell (see ROI I and II in Fig. 4b and c, Supplementary Movie 10, for two more examples, see Supplementary Movies 12, 13). This interaction was observed in 13 of the 15 HUVECs imaged. These interactions persisted for several minutes (Fig. 4b, arrows). To quantify the number of apparent ER-PM interactions in each movie we counted the number of long-term ER-PM interactions that persisted throughout each movie. To rule out these being random co-localization we compared them to the long-term ER-PM interactions that persisted throughout each movie when the 595 nm channel was flipped 180^o (Supplemental Fig. 18). We observed significant higher number of events in the former case, supporting that the apparent ER-PM interactions that we saw is not stochastic. Interestingly while the ER in a single cell is known to form contacts with the PM[21], the inter-cell interactions evident here have to our knowledge previously not been observed and may potentially represent a new site of inter-cellular communication, an area of wide general interest[22]. Aside, structure such as tunneling nanotubes (TNT) while now well accepted in many cell as important 50-200 nm thin tunnels between cells were only relatively recently discovered via serial EM[23] – highlighting the link between advanced imaging and detection of new interaction. In another example, mouse hippocampal neurons were labeled with the dual HIDE PM and mitochondria probes and imaged by STED (Fig. 4e, f). We can discern two separate structures, dendritic membrane and mitochondria, only 114 nm apart (Fig. 4f, ROI II, Fig. 4h). We also observed interactions between dendritic filopodia and mitochondria over a few minutes (Fig. 4g, Supplementary Movie 11).

Importantly the benefits of two-component HIDE probes are not limited to STED. A common photon-demanding imaging modality is 3D time-lapse (4D) imaging. To test the benefit of dual color HIDE probes, we compared conventional confocal 4D imaging of dual HIDE probes to cells tagged with the protein markers SMO25-Yale595 (mitochondria) and Smo-SiR (PM). Here too there was a major benefit of imaging with HIDE probes as SiR and Yale595 tagged HIDE probes were up to 8 times more photostable than the comparable protein-tags (Fig. 4i, j).

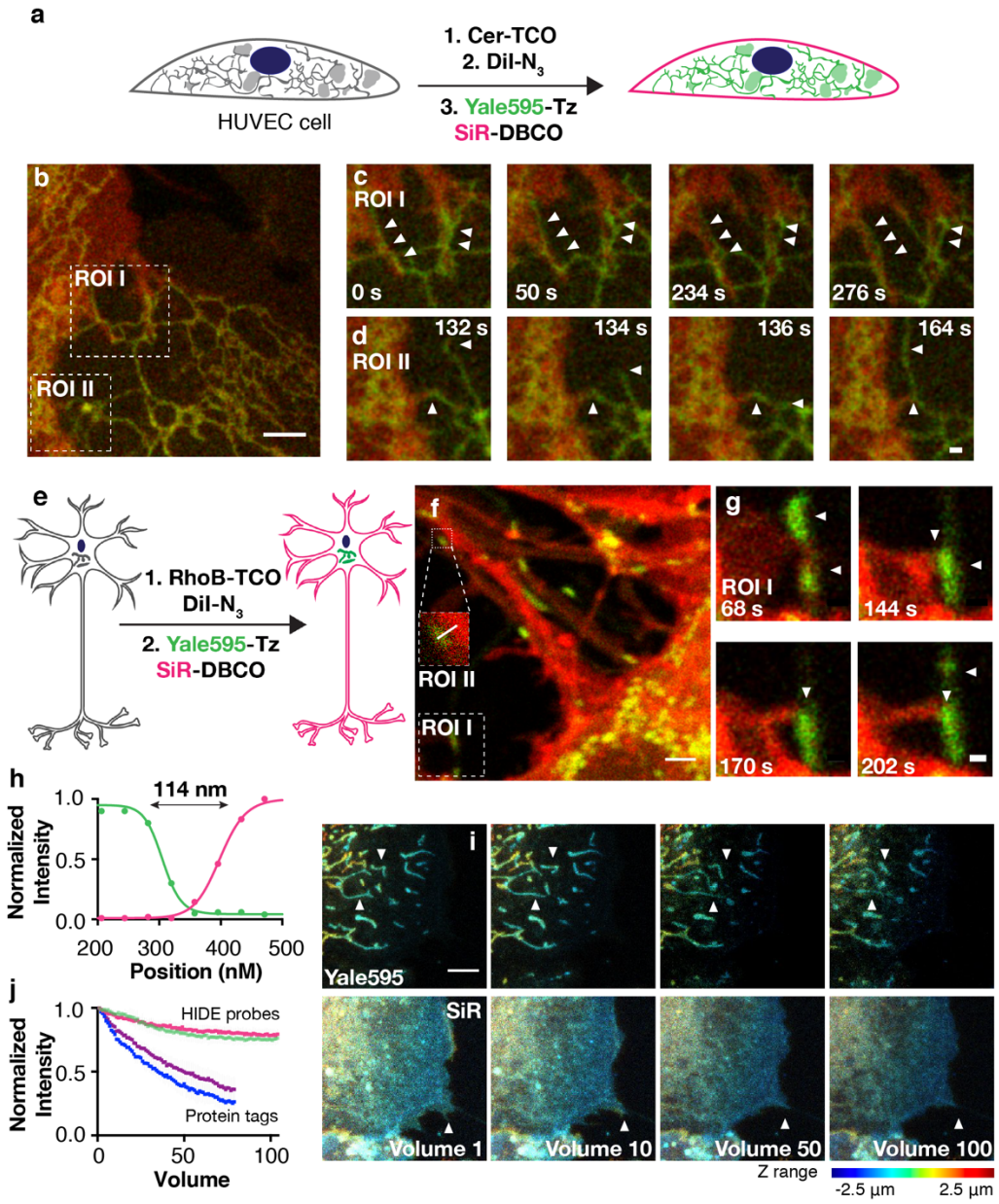

Figure 4 Application of two-color HIDE probes to primary cell lines. (**a**) Schematic illustration of the three-step procedure employed to label the plasma membrane and ER of Human umbilical vein endothelial cells (HUVECs). (**b**) Snapshot of a two-color STED movie of HUVEC. Scale bar: 2 µm. (**c,d**) Time lapse images of ER dynamics and interactions between filopodia and ER. Scale bars: 500 nm. (**e**) Schematic illustration of the two-step procedure employed to label the plasma membrane and mitochondria of DIV4 mouse hippocampal neurons. (**f**) Snapshot of a two-color STED movie of DIV4 mouse hippocampal neurons. Scale bar: 2 µm. (**g**) Time lapse images of interactions between filopodia and mitochondria. Scale bars: 500 nm. (**h**) Plot of line profile shown in (**f**, ROI II) illustrating the distance between plasma membrane and mitochondria. (**i**) Time-lapse two-color confocal imaging of mitochondria and plasma membrane in retinal pigment epithelium (RPE) cells. The mitochondrial and plasma membrane volumetric dynamics are recorded continuously over seconds. The axial information is color-coded. 20 z-stacks per volume. volumn rate: 6.1 s. Scale bar: 2 µm (**j**) Plot illustrating normalized fluorescence intensity of RhoB-Yale595 (green), DiI-SiR (red), SMO25-Yale595 (purple) and Smo-SiR (blue) over time (mean±SD, n = 3 ROI, N = 1 cell).

The new HIDE probes developed here enabled two-color time lapse live-cell STED imaging for hundreds of time points with virtually no bleaching, far exceeding the duration using state-of-the-art protein tags by over an order of magnitude. The labeling protocols can easily be adapted to various cell lines, including hard-to-transfect and primary cells. We envision that imaging experiments that require a large photon budget would generally benefit from these densely labeled and photostable organelle HIDE probes.

2.3 Methods

2.3.1 General methods: chemical synthesis, cell culture, plasmid construction, and microscopy.

2.3.1.1 Chemical synthesis. Synthesis protocol and additional characterization can be found in the supplementary information.

2.3.1.2 Cell culture. HeLa cells (ATCC) were cultured in Dulbecco's modified Eagle medium (DMEM) (Gibco) supplemented with 10% FBS (Sigma-Aldrich), penicillin (100 unit/mL) and streptomycin (100 µg/mL). hTERT RPE-1 cells (ATCC, CRT-400) were cultured in DMEM/F12 (Gibco) supplemented with 10% FBS, 1% nonessential amino acids (Gibco), 2 mM sodium pyruvate (Gibco), penicillin (100 unit/mL) and streptomycin (100 µg/mL). Human umbilical vein endothelial cells (HUVEC) (Lonza, C2517A) were cultured in EGMTM-2 Endothelial Cell Growth Medium-2 BulletKit (Lonza, CC-3162). All cells were purchased from commercial sources and periodically tested for mycoplasma with DNA methods. Primary neurons were isolated from P0-P1 mouse hippocampus using papain digestion and plated in Neurobasal A media (Invitrogen) with 2% Gem21 supplement (Gemini) and 10% FBS on glass- bottom culture dishes (Matek) coated with poly-D-lysine (20 µg/mL, Corning) and laminin 111 (1 µg/mL, Corning). Media was changed on the neurons after 4 hours and maintained in serum-free Neurobasal A/Gem21 media containing 1% pen/strep and 2 mM L-glutamine.

2.3.1.3 Plasmid. The SNAP-Tag plasmid Sec61□-SNAP and OMP25-SNAP was obtained from the Rothman lab and the Bewersdorf lab at Yale School of Medicine[16].
pLVX-ss-HaloTag-Smo: The ss-HaloTag-Smo fragment was PCR amplified from pC4S1-ss-Halotag-mSmo[7] and cloned by In-Fusion HD into pLVX-puro digested with *EcoRI* and *BamHI* to generate pLVX-ss-pH-Smo for lentivirus production.

2.3.1.4 Confocal microscopy. Spinning-disk confocal microscopy was performed using a Improvision UltraVIEW VoX system (Perkin-Elmer) built around a Olympus XI71 inverted microscope, equipped with PlanApo objectives (60×, 1.45 NA) and controlled by the Volocity software (Improvision). To image DiI and SiR, 561-nm and 640-nm laser lines with appropriate filters (615 ± 35 and 705 ± 45 nm, respectively) were used.

2.3.1.5 STED microscopy. Live-cell STED microscopy was performed on a Leica TCS SP8 Gated STED 3X microscope. The microscope is equipped with a tunable (460-660 nm) pulsed white light laser for excitation and two HyD detectors for tunable spectral detection. There are also two additional PMT detectors. The microscope is outfitted with

three STED depletion lasers (592 nm, 660 nm, and 775 nm). For live cell imaging, the microscope was equipped with a Tokai Hit stage top incubator (model: INUBG2A-GSI) with temperature and CO2 control to maintain an environment of 37°C and 5% CO2. Detailed information on excitation laser and detection window varies depend on the dyes and protocols used and is indicated below in each section. Imaging was conducted with a 100x oil immersion objective (HC PL APO 100x/1.40 OIL) at 1000 Hz with 2 line accumulations in a 19.38 μm2 field of view (1024x1024 pixels at 18.94 nm/pixel). Raw microscopy data were Gaussian blurred (2.0 pixels) in ImageJ. The FWHM values were obtained by fitting line profiles to a Lorentz distribution using Origin 9.1 (www.originlab.com)

2.3.2 Live-cell imaging of plasma membrane labeled with DiI-N_3 and SiR-DBCO

2.3.2.1 Labeling of plasma membrane with DiI-N_3 and SiR-DBCO. HeLa cells were incubated with 500 µL of 10 µM DiI-N_3 in PBS containing 1% casein hydrolysate for 3 min at 37 °C. The cells were then washed and incubated with 500 µL of 2 µM SiR-DBCO in PBS containing 1% casein hydrolysate for 30 min at 37 °C. After washing, DMEM ph(-) was added as imaging buffer, and confocal imaging was performed at 37 °C.

2.3.2.2 Optimization of labeling conditions. First, the concentration of DiI-N_3 was optimized. HeLa cells were incubated with 500 µL of 5 µM, 10 µM, 15 µM, or 20 µM in PBS containing 1% casein hydrolysate DiI-N_3 for 3 min at 37 °C. After washing, DMEM ph(-) was added as imaging buffer, and confocal imaging was performed at 37 °C. Then the concentration of SiR-DBCO was optimized. HeLa cells were incubated with 500 µL of 10 µM DiI-N_3 in PBS containing 1% casein hydrolysate for 3 min at 37 °C. The cells were then washed and incubated with 500 µL of 2 µM, 5µM, or 10 µM SiR-DBCO in PBS containing 1% casein hydrolysate for 30 min at 37 °C. After washing, DMEM ph(-) was added as imaging buffer, and confocal imaging was performed at 37 °C.

2.3.2.3 Labeling of plasma membrane with pre-mixed DiI-N_3 and SiR-DBCO. 500 µL of 10 µM DiI-N_3 and 2 µM, 5 µM, or 10 µM SiR-DBCO in PBS containing 1% casein hydrolysate was incubated at 37 °C for 1 hour. The formation of the product was confirmed by MS analysis. The resulting mixture was added to HeLa cells and incubated for 3 min at 37 °C. After washing, DMEM ph(-) was added as imaging buffer, and confocal imaging was performed at 37 °C.

2.3.2.4 Measurement of the photostability of DiI-N_3 and SiR-DBCO. HeLa cells were labeled as described in 2.1 and imaged under STED microscope at 37 °C. SiR dye was excited at 633 nm (40% power) and their emission was detected using a HyD detector from 650-737 nm. The 775 nm depletion laser was used for STED microscopy (30% power). Images were recorded continuously at 2 seconds per frame. Photobleaching plots were generated by normalizing background-subtracted fluorescence intensities (Plasma Membrane ROI – Background ROI) from three separate ROIs using the ROI manager Multi Measure tool in ImageJ.

2.3.3. Measurement of the photostability of 580CP, JF585, Atto590 and SiR700.
HeLa cells were incubated with 500 µL of 10 µM DiI-TCO in PBS containing 1% casein hydrolysate for 3 min at 37 °C. The cells were then washed and incubated with 500 µL of 2 µM 580CP-Tz, JF585-Tz, Atto590-Tz or SiR700 in PBS containing 1% casein hydrolysate for 30 min at 37 °C. After washing, DMEM ph(-)was added as imaging buffer, and STED imaging was performed at 37 °C. 580CP, and Atto590 were excited at 590 nm (5% power) and their emission was detected using a HyD detector from 600-670 nm. JF585 dye was excited at 590 nm (15% power) and their emission was detected using a HyD detector from 600-670 nm. SiR700 dye was excited at 650 nm (40% power) and their emission was detected using a HyD detector from 660-730 nm. The 775 nm depletion laser was used for STED microscopy (30% power). Images were recorded continuously at 2 seconds per frame. Photobleaching plots were generated by normalizing background-subtracted fluorescence intensities (Plasma Membrane ROI – Background ROI) from three separate ROIs using the ROI manager Multi Measure tool in ImageJ.

2.3.4. Live-cell imaging with Yale595.
2.3.4.1 Measurement of photophysical properties of Yale595.
2.3.4.1a Absorption and Emission Spectra of Yale-595 and SiR. The absorbance spectra of Yale-595 and SiR were measured at 2 µM in DPBS (w/ 0.1% DMSO) on a Beckman UV-Vis spectrophotomerter. The emission spectra of the same solutions were measured on a TCSPC TD-Fluor Horiba Fluorolog 3 Time Domain Fluorimeter.

2.3.4.1b Quantum Yield Determination for Yale-595. Solutions of Yale-595 and Bodipy-Texas Red between 0 – 10 µM were prepared in DPBS (w/ 0.05% - 0.25% DMSO). Absorbance at 550 nm was measured for each on a Beckman UV-Vis spectrophotomerter. Afterwards, fluorescence of the same samples was measured on a TCSPC TD-Fluor Horiba Fluorolog 3 Time Domain Fluorimeter. Both the excitation and emission bandwidths for all measurements were set to 5 nm. The spectra were recorded with a step size of 1 nm. The excitation wavelength was set to 550 nm and the emission spectra were recorded in the 560-800 nm interval. Absorbance at 550 nm versus integrated fluorescence intensity for each solution was plotted using GraphPad Prism 7.0. The relative quantum yield of Yale-595 was calculated from the linear regressions according to the following:

$$QY_{exp} = \frac{m_{exp}}{m_{std}} QY_{std}$$

Where QY_{exp} and m_{exp} are the relative quantum yield and slope of linear regression, respectively, for Yale-595 and QY_{std} and m_{std} are the absolute quantum yield and slope of linear regression, respectively, for Bodipy-Texas Red. The absolute quantum yield for Bodipy-Texas Red was previously reported.

2.3.4.1b Standard Curve of Exctinction Coefficient for Yale 595. Solutions of Yale-595 and SiR at 5µM, 10 µM, 15 µM, 20 µM and 25 µM in DPBS (w/ 0.25 – 1.25% DMSO) were prepared. The absorbance at 597 nm (Yale-595) or 652 nm (SiR) were measured

on Spiegel Lab plate reader using polypropylene 96-well plates. The concentrations were plotted against their absorbances using GraphPad Prism 7.0. The extinction coefficient of Yale-595 was calculated from the linear regressions according to the following:

$$\varepsilon_{exp} = \frac{m_{exp}}{m_{std}} \varepsilon_{std}$$

Where ε_{exp} and m_{exp} are the extinction coefficient and slope of linear regression, respectively, for Yale-595 and ε_{std} and m_{std} are the extinction coefficient and slope of linear regression, respectively, for SiR. The extinction coefficient for SiR was previously reported[8].

2.3.4.2 Measurement of absorbance in response to different solvent polarities. Yale595-COOH (or JF585-COOH) was dissolved into a mixture of water and dioxane (0-100% dioxane in water) to a final concentration of 10 µM. The absorbance data was recorded on a DU730 Life Science UV/Vis spectrophotometer using the wavelength scan mode.

2.3.4.3 Measurement of the photostability of Yale595. HeLa cells were incubated with 500 µL of 10 µM DiI-TCO in PBS containing 1% casein hydrolysate for 3 min at 37 °C. The cells were then washed and incubated with 500 µL of 2 µM Yale595-Tz in PBS containing 1% casein hydrolysate for 30 min at 37 °C. After washing, DMEM ph(-)was added as imaging buffer, and STED imaging was performed at 37 °C. Yale595 dye was excited at 595 nm (10% power) and their emission was detected using a HyD detector from 605-675 nm. The 775 nm depletion laser was used for STED microscopy (30% power). Images were recorded continuously at 2 seconds per frame. Photobleaching plots were generated by normalizing background-subtracted fluorescence intensities (Plasma Membrane ROI – Background ROI) from three separate ROIs using the ROI manager Multi Measure tool in ImageJ.

2.3.4.4 Live-cell STED imaging of ER using Yale595. HeLa cells were incubated with 500 µL of 2 µM Cer-TCO in PBS containing 1% casein hydrolysate and 0.2% Pluronic F-127 for 60 min at 37 °C. The cells were then washed and incubated with 500 µL of 2 µM Yale595-Tz in PBS containing 1% casein hydrolysate for 30 min at 37 °C and imaged on the SP8 STED microscope. Yale595 dye was excited at 595 nm (10% power) and their emission was detected using a HyD detector from 605-675 nm. The 775 nm depletion laser was used for STED microscopy (30% power).

2.3.5. Live-cell two-color STED imaging using HIDE probes.

2.3.5.1 Plasma membrane and ER of HeLa cells. HeLa cells were incubated with 500 µL of 4 µM Cer-TCO in Live Cell Imaging Solution (Life Technologies, A14291DJ) containing 0.2% Pluronic F-127 for 60 min at 37 °C. After washing, the cells were treated with 500 µL of 10 µM DiI-N_3 in Live Cell Imaging Solution for 3 min at 37 °C. After washing, the cells were incubated with 500 µL of 2 µM SiR-DBCO and 2 µM Yale595-Tz in Live Cell Imaging Solution for 30 min at 37 °C. After washing, STED imaging was carried out at 37 °C using DMEM ph(-) as the imaging buffer under Leica SP8 microscope with two

excitation lasers at 595 nm (10% power), 650 nm (60% power) and two detection windows at 605-625 nm and 670-750 nm. The 775 nm depletion laser was used for STED microscopy (30% power). Images were recorded continuously at 2 seconds per frame. Raw image data were spectral unmixed and Gaussian blurred (2.0 pixels) in ImageJ.

2.3.5.2 Plasma membrane and mitochondria of HeLa cells. HeLa cells were incubated with 500 µL of 10 µM RhoB-TCO and 10 µM Dil-N_3 in Live Cell Imaging Solution for 3 min at 37 °C. After washing, the cells were incubated with 500 µL of 2 µM SiR-DBCO and 2 µM Yale595-Tz in Live Cell Imaging Solution for 30 min at 37 °C. After washing, cells were incubated at 37 °C in DMEM ph(-) for 30 min to wash out the remaining dyes. After further washing, STED imaging was carried out at 37 °C using DMEM ph(-) as the imaging buffer under Leica SP8 microscope with two excitation lasers at 595 nm (10% power), 650 nm (60% power) and two detection windows at 605-625 nm and 670-750 nm. The 775 nm depletion laser was used for STED microscopy (30% power). Images were recorded continuously at 2 seconds per frame. Raw image data were spectral unmixed and Gaussian blurred (2.0 pixels) in ImageJ.

2.3.5.3 Plasma membrane and ER of Human umbilical vein endothelial cells (HUVEC). HUVECs were incubated with 500 µL of 4 µM Cer-TCO in Live Cell Imaging Solution containing 0.2% Pluronic F-127 for 60 min at 37 °C. After washing, the cells were treated with 500 µL of 10 µM Dil-N_3 in Live Cell Imaging Solution for 3 min at 37 °C. After washing, the cells were incubated with 500 µL of 2 µM SiR-DBCO and 2 µM Yale595-Tz in Live Cell Imaging Solution for 30 min at 37 °C. After washing, STED imaging was carried out at 37 °C using DMEM ph(-) as the imaging buffer under Leica SP8 microscope with two excitation lasers at 594 nm (10% power), 650 nm (60% power) and two detection windows at 605-625 nm and 670-750 nm. The 775 nm depletion laser was used for STED microscopy (30% power). Images were recorded continuously at 2 seconds per frame. Raw image data were spectral unmixed and Gaussian blurred (2.0 pixels) in ImageJ.

2.3.5.4 Plasma membrane and mitochondria of mouse hippocampal neuron cells. Neuron cells were incubated with 500 µL of 10 µM RhoB-TCO and 10 µM Dil-N_3 in DMEM for 3 min at 37 °C. After washing, the cells were incubated with 500 µL of 2 µM SiR-DBCO and 2 µM Yale595-Tz in DMEM for 30 min at 37 °C. After washing, cells were incubated at 37 °C in DMEM ph(-) for 30 min to wash out the remaining dyes. After further washing, STED imaging was carried out at 37 °C using DMEM as the imaging buffer under Leica SP8 microscope with two excitation lasers at 595 nm (10% power), 650 nm (60% power) and two detection windows at 605-625 nm and 670-750 nm. The 775 nm depletion laser was used for STED microscopy (30% power). Images were recorded continuously at 2 seconds per frame. Raw image data were Gaussian blurred (2.0 pixels) in ImageJ.

2.3.6. Live-cell two-color imaging using protein tags.

2.3.6.1 Two-color STED imaging of plasma membrane and ER. Generation of hTERT RPE-1 cells stably expressing Smo-Halo was described previously using pLVX-ss-HaloTag-Smo[24]. hTERT RPE-1 cells stably expressing Smo-Halo were transfected with

Sec61β-SNAP using FuGENE HD Transfection Reagent (Promega) one day before imaging. Before imaging, the cells were incubated with 500 µL of 2 µM SiR-CA and 2 µM Yale595-BG in Live Cell Imaging Buffer for 30 min at 37 °C. After washing, STED imaging was carried out at 37 °C using DMEM as the imaging buffer under Leica SP8 microscope with two excitation lasers at 595 nm (10% power), 650 nm (60% power) and two detection windows at 605-625 nm and 670-750 nm. The 775 nm depletion laser was used for STED microscopy (30% power). Images were recorded continuously at 2 seconds per frame. Raw image data were spectral unmixed Gaussian blurred (2.0 pixels) in ImageJ.

2.3.6.2 Two-color confocal 3D imaging of plasma membrane and Mitochondria. hTERT RPE-1 cells stably expressing Smo-Halo were transfected with OMP25-SNAP using FuGENE HD Transfection Reagent (Promega) one day before imaging. Before imaging, the cells were incubated with 500 µL of 2 µM SiR-CA and 2 µM Yale595-BG in Live Cell Imaging Buffer for 30 min at 37 °C. After washing, STED imaging was carried out at 37 °C using DMEM as the imaging buffer under Leica SP8 microscope with two excitation lasers at 595 nm (10% power), 650 nm (60% power) and two detection windows at 605-625 nm and 670-750 nm. The 775 nm depletion laser was used for STED microscopy (30% power). Images were recorded continuously at 2 seconds per frame. Raw image data were spectral unmixed Gaussian blurred (2.0 pixels) in ImageJ.

2.3.7. Live-cell two-color 3D confocal imaging of plasma membrane and mitochondria using HIDE probes.

HeLa cells were incubated with 500 µL of 10 µM RhoB-TCO and 10 µM DiI-N_3 in Live Cell Imaging Solution for 3 min at 37 °C. After washing, the cells were incubated with 500 µL of 2 µM SiR-DBCO and 2 µM Yale595-Tz in Live Cell Imaging Solution for 30 min at 37 °C. After washing, cells were incubated at 37 °C in DMEM ph(-) for 30 min to wash out the remaining dyes. After further washing, 3D confocal imaging was carried out at 37 °C using DMEM ph(-) as the imaging buffer under Leica SP8 microscope with two excitation lasers at 595 nm (3% power), 650 nm (20% power) and two detection windows at 605-625 nm and 670-750 nm. The images were taken at 20 z-stacks per volume at 6.1s per volume. Raw image data were spectral unmixed in ImageJ.

2.3.8. Evaluation of cellular toxicity of two-color HIDE probes using a cell division assay[6].

We monitored the cell division in three groups of HeLa cells. 1) Non-treated cells; 2) HeLa cells labeled as described in 5.1; and 3) HeLa cells labeled as described in 5.2. Labeling of the cells was confirmed by a confocal microscopy. Wide field imaging was carried out on an Invitrogen™ EVOS™ FL Auto 2 Imaging system equipped with temperature, humidity, and atmosphere controls for live cell imaging. The sample was kept at 37 °C with 5% CO2 and imaged using a 20x objective and a high sensitivity 1.3 MP CMOS camera (1,328 x 1,048 pixels) every 10 minutes for 15 h using bright field. Cell division events were counted manually.

2.3.9 Chemical Synthesis

2.3.9.1 General considerations. Chemicals used for synthesis were purchased from commercial sources and were used without further purification. Flash chromatography was performed using a Teledyne Isco CombiFlash Rf using pre-packed columns with RediSep Rf silica (40– 60 μm). ^{1}H NMR and ^{13}C NMR spectra were recorded on an Agilent DD2 600 NMR spectrometer (600 MHz for ^{1}H and 151 MHz for ^{13}C). The values of chemical shifts (δ) are reported in p.p.m. relative to the solvent residual signals of CD_3OD (3.31 p.p.m. for ^{1}H, 49.00 p.p.m. for ^{13}C), CD_2Cl_2 (5.33 p.p.m. for ^{1}H, 53.84 p.p.m. for ^{13}C) or CD_3CN (1.94 p.p.m. for ^{1}H, 1.32, 118.26 p.p.m. for ^{13}C). Coupling constants (*J*) are reported in Hz. High-resolution mass spectra (HRMS) were recorded on a Waters Xevo QTOF LCMS with ESI using a Waters Acquity UPLC. HPLC purifications were performed on a reverse-phase colμMn (GL Sciences, Inertsil ODS-3 10 mm × 250 mm and Inertsil ODS-3 20 mm × 250 mm) using a HPLC system composed of a pump (Jasco PU-2080 or PU-2087) and a detector (Jasco MD-2010 or MD- 2018).

2.3.9.2 Experimental. Cer-TCO[1], DiI-TCO[2], RhoB-TCO[2], Atto590-Tz[3], and SiR-Tz[4] were synthesized as described previously.

2.3.9.3 Synthesis of DiI-N3, 1.

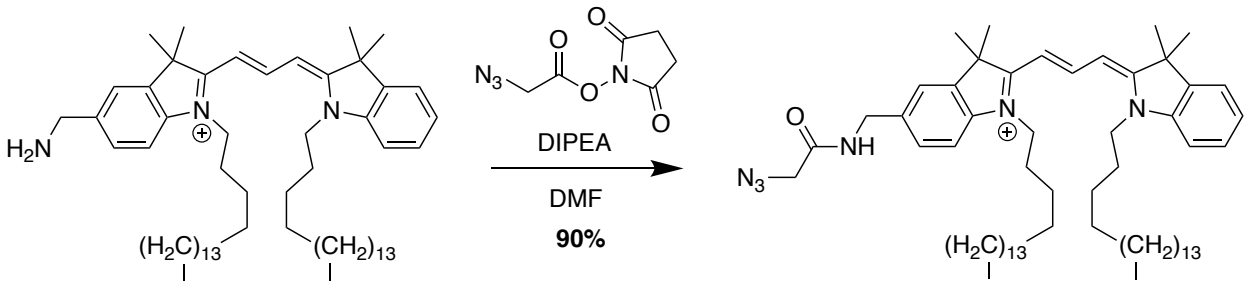

DiI-NH$_2$ **DiI-N$_3$. 1**

DiI-NH2 (10 mg, 1.0 eq), azido-acetic acid-NHS (Sigma-Aldrich, 1.2 eq) and DIPEA (3.0 eq) were dissolved in DMF (1 mL) under an argon atmosphere, stirred for 6 h, and concentrated under reduced pressure. The residue was subjected to flash column chromatography (100:0 CH_2Cl_2:CH_3OH / CH_2Cl_2:CH_3OH 90:10) to yield DiI-N3 as a pink solid (90% yield). ^{1}H NMR (600 MHz, Methanol-*d*4) δ 8.57 (dd, *J* = 13.4, 13.4 Hz, 1H), 7.58 (d, *J* = 7.4 Hz, 1H), 7.53 (s, 1H), 7.48 (dd, *J* = 7.7, 7.7 Hz, 1H), 7.43 (d, *J* = 8.1 Hz, 1H), 7.38 (d, *J* = 8.0 Hz, 1H), 7.35 (dd, *J* = 8.8, 8.8 Hz, 2H), 6.49 (d, *J* = 13.5 Hz, 1H), 6.48 (d, *J* = 13.4 Hz, 1H), 4.51 (s, 2H), 4.24 – 4.14 (m, 4H), 3.98 (s, 2H), 1.91 – 1.83 (m, 4H), 1.80 (s, 12H),

1.58 – 1.22 (m, 60H), 0.92 (t, J = 6.9 Hz, 6H). ^{13}C NMR (151 MHz, CD_3OD) δ 176.87, 176.78, 171.03, 152.78, 144.21, 143.54, 143.40, 143.08, 138.59, 130.87, 130.34, 127.67, 124.40, 123.92, 113.36, 113.30, 104.65, 104.62, 53.92, 51.53, 51.46, 46.15, 46.10, 44.70, 33.95, 31.66, 31.64, 31.61, 31.49, 31.47, 31.46, 31.45, 31.36, 31.28, 29.39, 29.38, 29.19, 28.64, 28.64, 24.62, 15.34. HRMS [$C_{62}H_{101}N_6O^+$] Cal: 945.8031, Obs: 945.8050.

2.3.9.4 Synthesis of SiR-DBCO 2.

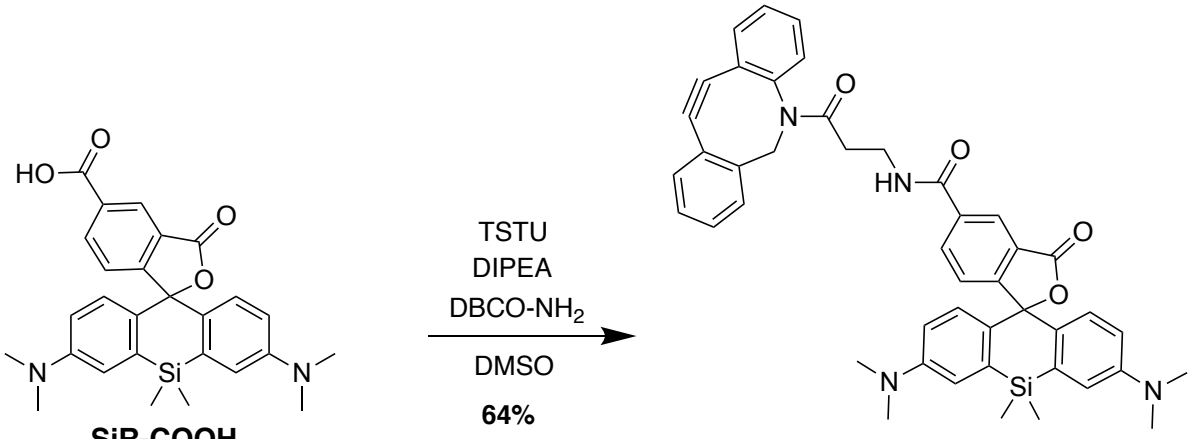

SiR-COOH (5 mg, 1 eq.)[4], TSTU (1.2 eq.) and DIPEA (2 eq.) were dissolved in DMSO and stirred at room temperature for 20 min. DBCO-NH_2 (Click Chemistry Tools LLC, 1.2 eq.) and DIPEA (2 eq.) was added and the stirring was continued for 2 hours until LC-MS showed no remaining starting material. The mixture was then filtered and purified by reverse phase HPLC using eluent A (H_2O with 0.1% TFA) and eluent B (CH_3CN with 0.1% TFA) to give SiR-DBCO as a blue solid (64% yield). HRMS [$C_{45}H_{43}N_4O_4Si^+$] Cal: 731.3048, Obs: 731.3025.

2.3.9.5 Synthesis of 580CP-Tz, 3.

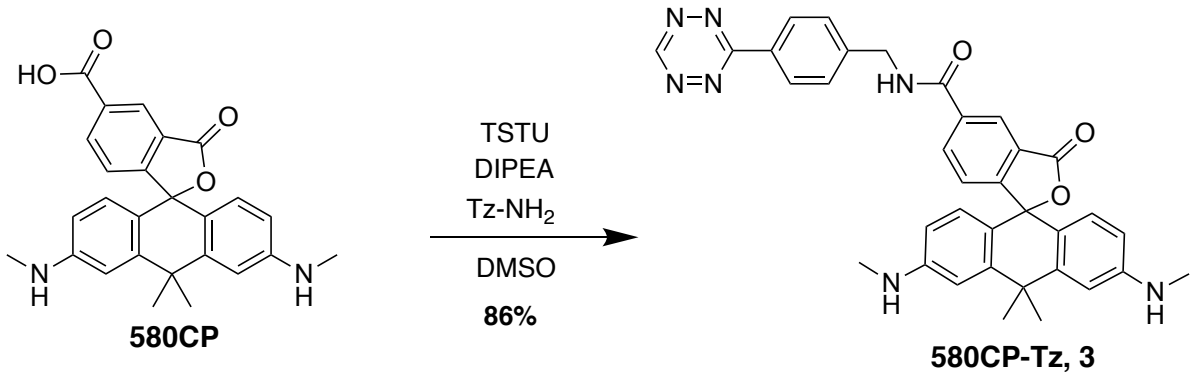

580CP-COOH was synthesized as previously described[5]. 580CP-COOH (5 mg, 1 eq.), TSTU (1.2 eq.) and DIPEA (2 eq.) were dissolved in DMSO and stirred at room temperature for 20 min. Tz-NH_2 (2 eq.) and DIPEA (2 eq.) were added and the stirring was continued for 2 hours until LC-MS showed completion of the reaction. The mixture was then filtered and purified by reverse phase HPLC using eluent A (H_2O with 0.1% TFA) and eluent B (CH_3CN with 0.1% TFA) to give 580CP-Tz as a purple solid (86% yield). ^{1}H NMR (600 MHz, Methanol-*d*4) δ 10.31 (s, 1H), 8.79 (d, *J* = 1.8CP-Tz 3 Hz, 1H), 8.59 (d, *J* = 8.4 Hz, 2H), 8.27 (dd, *J* = 7.9, 1.9 Hz, 1H), 7.68 (d, *J* = 8.5 Hz, 2H), 7.46 (d, *J* = 7.9 Hz, 1H), 7.10 (d, *J* = 2.2 Hz, 2H), 6.96 (d, *J* = 8.8 Hz, 2H), 6.60 (dd, *J* = 9.2, 2.2 Hz, 2H), 4.78 (s, 2H), 3.03 (s, 6H), 1.81 (s, 3H), 1.70 (s, 3H). ^{13}C NMR (151 MHz, CD_3OD) δ 169.27, 168.50, 168.25, 167.66, 160.17, 160.15, 160.13, 146.36, 143.06, 137.51, 133.87, 133.32, 133.03, 132.79, 132.06, 130.33, 130.28, 122.69, 112.29, 45.35, 36.35,32.72, 30.87.HRMS: [$C_{35}H_{32}N_7O_3^+$] Cal: 598.2561, Obs: 598.2554.

2.3.9.6 Synthesis of SiR700-Tz, 4.

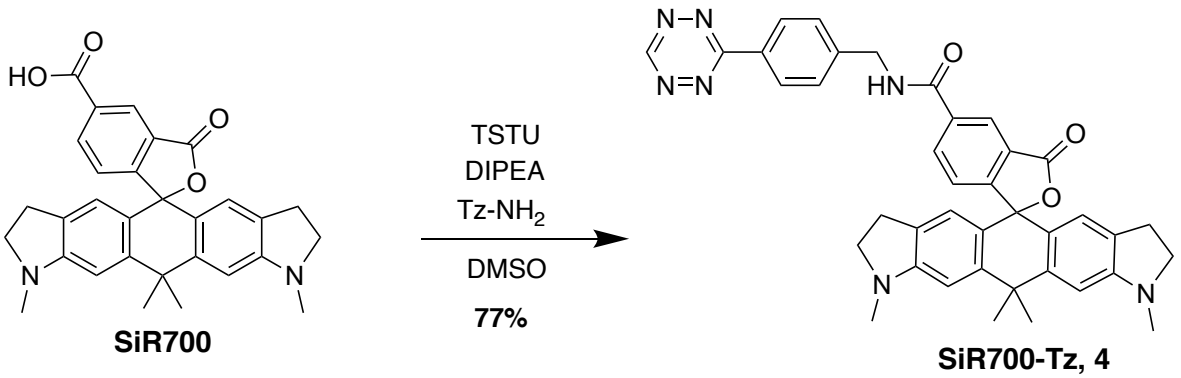

SiR700 **SiR700-Tz, 4**

SiR700-COOH was synthesized as previously described [6]. SiR700-COOH (5 mg, 1 eq.), TSTU (1.2 eq.) and DIPEA (2 eq.) were dissolved in DMSO and stirred at room temperature for 20 min. Tz-NH2 (2 eq.) and DIPEA (2 eq.) were added and the stirring was continued for 2 hours until LC-MS showed completion of the reaction. The mixture was then filtered and purified by reverse phase HPLC using eluent A (H_2O with 0.1% TFA) and eluent B (CH_3CN with 0.1% TFA) to give SiR700-Tz as a green solid (77% yield). ^{1}H NMR (600 MHz, Methanol-*d*4) δ 10.35 (s, 1H), 8.62 (d, *J* = 8.2 Hz, 2H), 8.47 (s, 1H), 8.19 (d, *J* = 8.1 Hz, 1H), 7.69 (d, *J* = 8.1 Hz, 2H), 7.25 (d, *J* = 8.0 Hz, 2H), 6.80 (s, 2H), 6.63 (s, 2H), 4.78 (s, 2H), 3.30 – 3.24 (m, 4H), 2.91 – 2.72 (m, 10H), 0.63 (s, 3H), 0.56 (s, 3H). ^{13}C NMR (151 MHz, cd_3od) δ 173.31, 169.43, 168.50, 163.69, 160.13, 155.18, 146.33, 137.44, 137.00, 135.51, 135.20, 134.47, 133.28, 130.26, 130.25, 128.63, 128.62, 126.47, 126.43, 125.45, 112.58, 57.42, 45.30, 36.75, 30.12, 0.81, 0.36. HRMS [$C_{38}H_{36}N_7O_3Si^+$] Cal: 666.2643, Obs: 666.2647.

2.3.9.7 Synthesis of JF585-Tz 5.

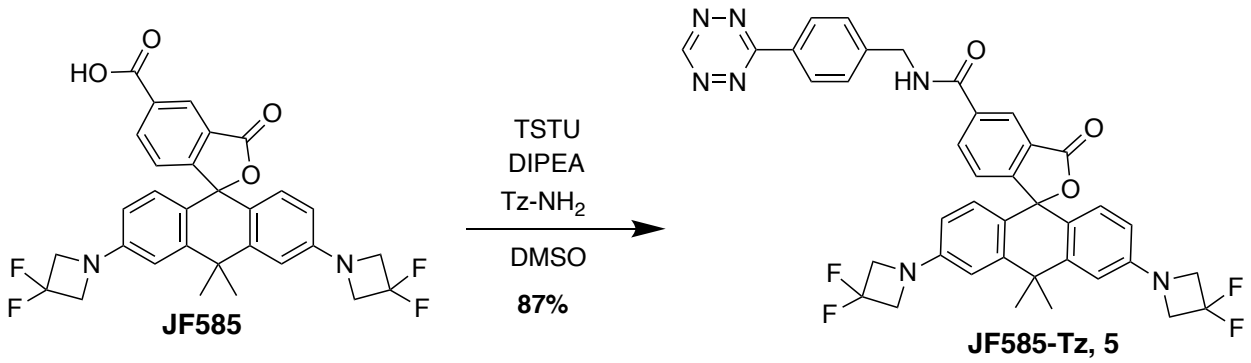

JF585-COOH[7] (Tocris Bioscience, 0.5 mg, 1 eq.), TSTU (1.2 eq.) and DIPEA (2 eq.) were dissolved in DMSO and stirred at room temperature for 20 min. Tz-NH2 (2 eq.) and DIPEA (2 eq.) were added and the stirring was continued for 2 hours until LC-MS showed completion of the reaction. The mixture was then filtered and purified by reverse phase HPLC using eluent A (H_2O with 0.1% TFA) and eluent B (CH_3CN with 0.1% TFA) to give JF585-Tz as a purple solid (87% yield). ^1H NMR (600 MHz, DMSO-*d*6) δ 10.54 (s, 1H), 9.40 (dd, *J* = 5.8, 5.8 Hz, 1H), 8.40 (d, *J* = 8.2 Hz, 2H), 8.17 (d, *J* = 8.1 Hz, 1H), 8.08 (d, *J* = 8.1 Hz, 1H), 7.52 (d, *J* = 8.2 Hz, 2H), 7.47 (s, 1H), 6.83 (d, *J* = 2.0 Hz, 2H), 6.51 (d, *J* = 8.6 Hz, 2H), 6.39 (dd, *J* = 8.6, 2.2 Hz, 2H), 4.51 (d, *J* = 5.8 Hz, 2H), 4.28 (t, *J* = 12.3 Hz, 8H), 1.80 (s, 3H), 1.68 (s, 3H). ^{13}C NMR (151 MHz, DMSO-*d*6) δ 169.49, 165.80, 165.26, 158.55, 155.62, 150.76, 146.62, 144.77, 140.60, 130.92, 128.72, 128.30, 125.51, 122.56, 121.00, 117.12, 112.74, 116.23 (t, *J* = 277.2 Hz), 110.42, 63.32 (t, *J* = 24.9 Hz), 44.55, 38.38, 34.78, 33.52. HRMS [$C_{39}H_{32}F_4N_7O_3^+$] Cal: 722.2497, Obs: 722.2496.

Compound **6** was synthesized according to previous reports[7]:

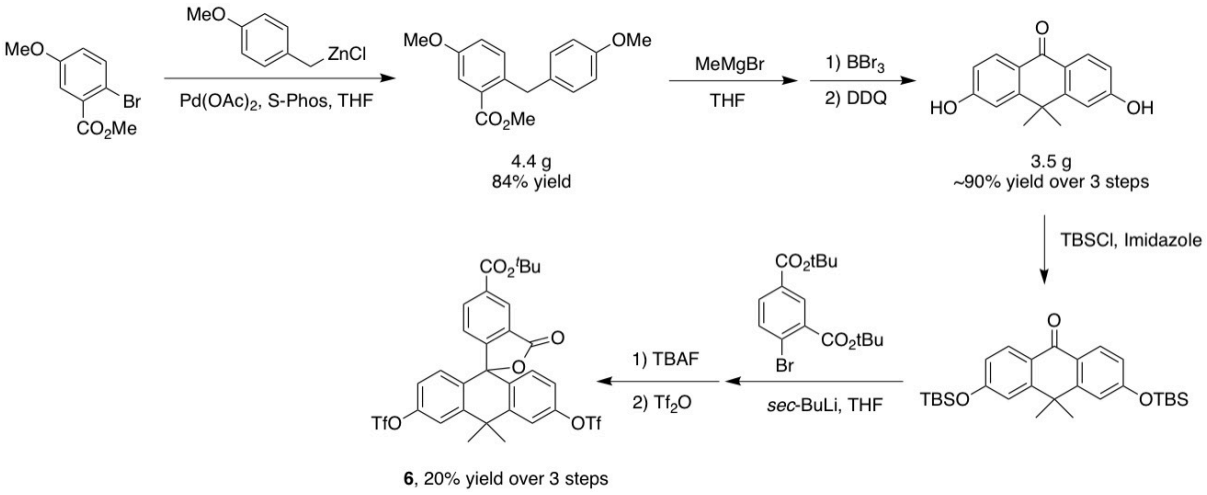

2.3.9.8 Synthesis of Yale595-COOH, 7.

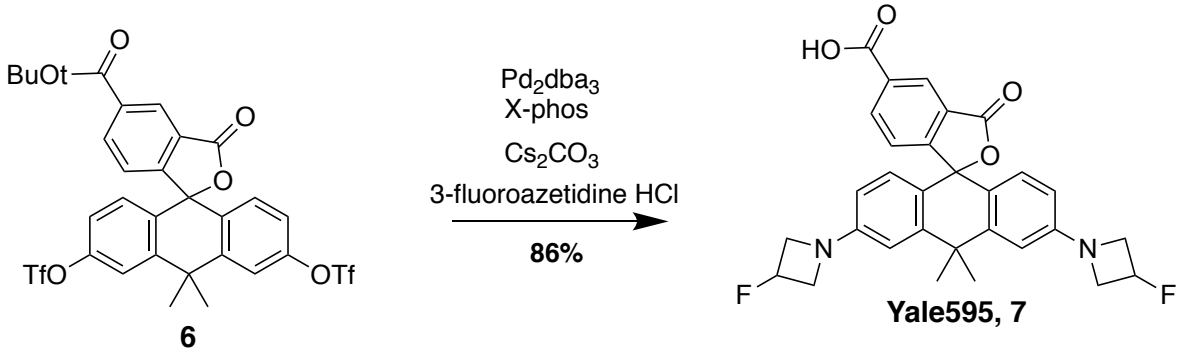

Yale595-COOH **7** was prepared from bis-triflate **6** as described previously[7]. To a Schlenk tube was added Pd2dba3 (0.1 eq.), X-phos (0.3 eq.), compound **6** (1 eq., 130 mg), 3-fluoroazetidine hydrochloride (2.2 eq.), Cs_2CO_3 (5 eq.), and 4 mL dioxane. The mixture was stirred under N_2 at 100 ^{o}C for 5 h. The mixture was filtered through a pad of Celite, concentrated and purified by silica gel to obtain the product as a dark- purple solid (86 % yield). ^{1}H NMR (600 MHz, Methanol-*d*4) δ 8.85 (s, 1H), 8.37 (d, *J* = 7.9 Hz, 1H), 7.42 (d, *J* = 7.9 Hz, 1H), 7.01 – 6.92 (m, 4H), 6.46 (d, *J* = 9.1 Hz, 2H), 5.63 – 5.59 (m, 1H), 5.54 – 5.50 (m, 1H), 4.66 – 4.56 (m, 4H), 4.38 (dd, *J* = 23.4, 11.6 Hz, 4H), 1.88 (s, 3H), 1.76 (s, 3H). ^{13}C NMR (151 MHz, CD_3OD) δ 168.83, 168.49, 158.32, 157.28, 157.27, 137.94, 135.26, 134.38, 133.56, 133.17, 132.16, 122.90, 113.47, 111.35, 84.39 (d, *J* = 203.7 Hz), 61.34 (d, *J* = 26.3 Hz), 43.49, 36.30, 32.81. HRMS [$C_{30}H_{27}F_2N_2O_4^+$] Cal: 517.1933, Obs: 517.1934.

2.3.9.9 Synthesis of Yale595-Tz 8.

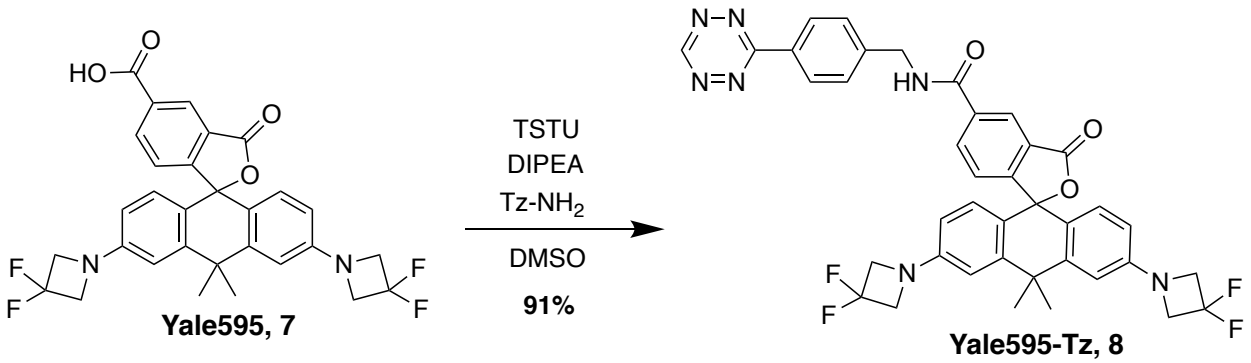

Yale595, 7 **Yale595-Tz, 8**

Yale595-COOH (5 mg, 1 eq.), TSTU (1.2 eq.) and DIPEA (2 eq.) were dissolved in DMSO and stirred at room temperature for 20 min. Tz-NH_2 (2 eq.) and DIPEA (2 eq.) was added and the stirring was continued for 2 hours until LC-MS showed no remaining starting material. The mixture was then filtered and purified by reverse phase HPLC using eluent A (H_2O with 0.1% TFA) and eluent B (CH_3CN with 0.1% TFA) to give Yale595-Tz as a purple solid (91% yield).

^1H NMR (600 MHz, DMSO-*d*6) δ 10.59 (s, 1H), 9.52 (t, *J* = 6.0 Hz, 1H), 8.54 (s, 1H), 8.50 (d, *J* = 8.3 Hz, 2H), 8.23 (dd, *J* = 8.1, 1.5 Hz, 1H), 7.66 (d, *J* = 8.4 Hz, 2H), 7.17 (d, *J* = 7.9 Hz, 1H), 6.74 (d, *J* = 2.3 Hz, 2H), 6.49 (d, *J* = 8.6 Hz, 2H), 6.33 (dd, *J* = 8.6, 2.4 Hz, 2H), 5.57 – 5.51 (m, 1H), 5.47 – 5.41 (m, 1H), 4.67 (d, *J* = 5.9 Hz, 2H), 4.19 (ddd, *J* = 20.8, 9.4, 5.8 Hz, 4H), 3.93 (ddd, *J* = 24.2, 9.3, 2.4 Hz, 4H), 1.80 (s, 3H), 1.69 (s, 3H).

^{13}C NMR (151 MHz, DMSO-*d*6) δ 169.28, 165.42, 164.89, 158.11, 157.66, 151.41, 151.40, 146.06, 144.58, 135.29, 134.62, 130.48, 128.24, 128.22, 127.86, 126.03, 123.90, 123.42, 119.46, 111.32, 108.87, 83.46 (d, *J* = 199.9 Hz), 59.28 (d, *J* = 23.3 Hz), 48.59, 42.71, 37.86, 34.38, 33.11. HRMS: [$C_{39}H_{34}F_2N_7O_3^+$] Cal: 686.2686, Obs: 686.2683.

2.4 Supplementary Figures

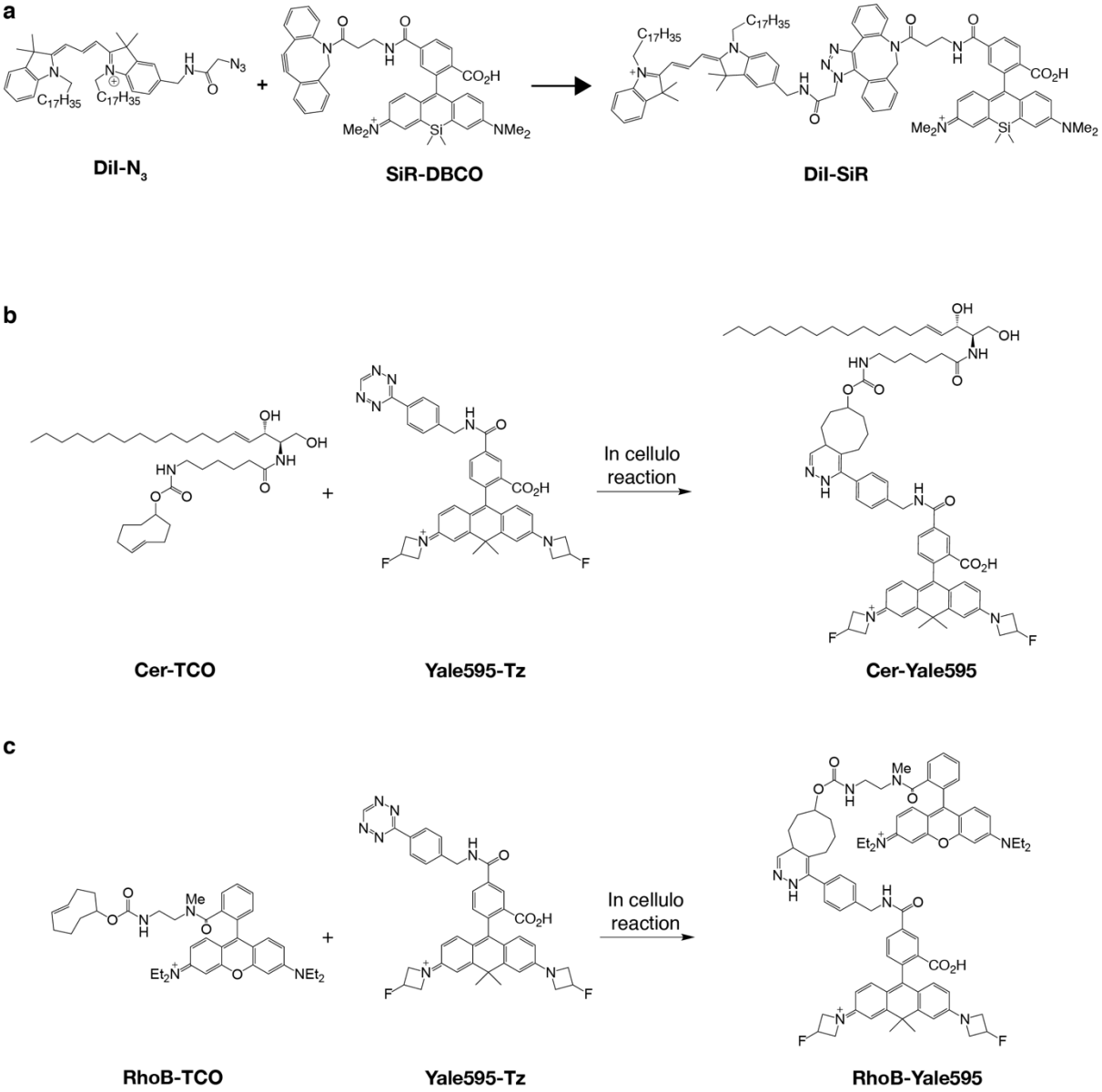

Supplementary Figure 1. Chemical structures and reactions used for labeling of organelle membranes. (a) In cellulo strain-promoted alkyne-azide cycloadditions between DiI-N_3 and SiR-DBCO yields DiI-SiR. (b) In cellulo inverse electron-demand Diels-Alder reaction between Cer-TCO and Yale595-Tz yields Cer-Yale595. (c) In cellulo inverse electron-demand Diels-Alder reaction between RhoB-TCO and Yale595-Tz yields RhoB-Yale595.

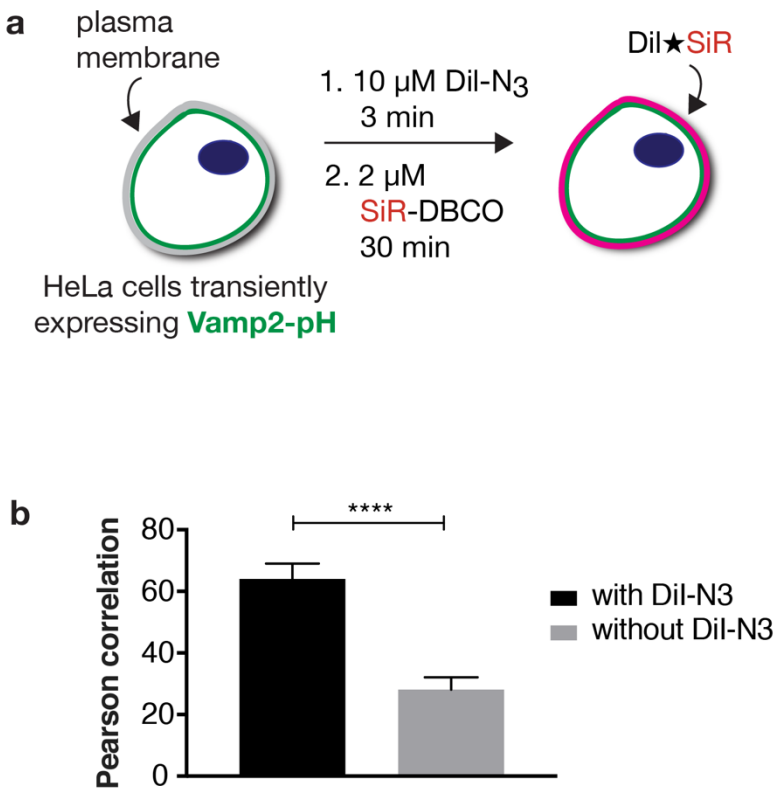

Supplementary Figure 2. Labeling of plasma membrane with DiI-N_3 and SiR-DBCO. (a) Schematic illustration of the in vivo labeling protocol. (b) Pearson correlation between Vamp2-pH and DiI-SiR (black) or Vamp2-pH and SiR-DBCO (grey). (mean±SD, N = 5), ****P≤ 0.0001

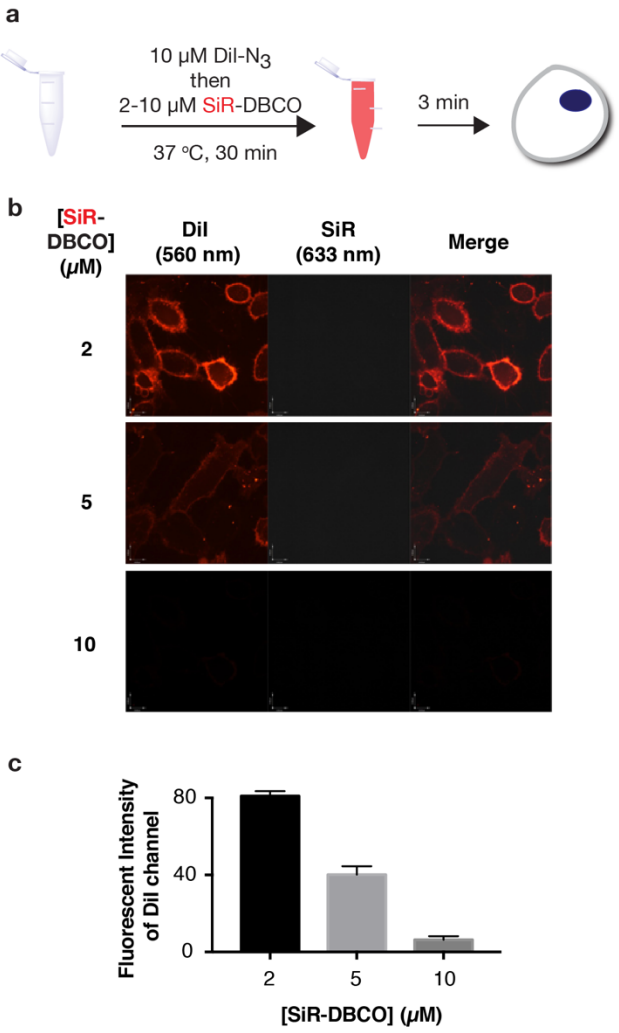

Supplementary Figure 3. In vitro pre-mixing of DiI-N_3 and SiR-DBCO and labeling of plasma membrane. (a) Schematic illustration of the in vitro mixing protocol. 10 μM DiI-N_3 in PBS with 1% casein was mixed with different concentrations of SiR-DBCO in PBS with 1% casein in an eppendorf tube and incubated at 37 °C for 30 min. The mixture was then added to HeLa cells and incubated at 37 °C for 3 min and imaged under a spinning disk confocal microscope. The formation of product DiI-SiR in vitro was confirmed by LC-MS. (b) Images of 10 μM DiI-N_3 pre-mixed with different concentrations of SiR-DBCO. No plasma membrane labeling was detected in the SiR (633 nm) channel, indicating the pre-mixed product does not localize on the plasma membrane. (c) Fluorescent intensity quantification of b, first row. The fluorescent intensity of DiI channel decreases as the concentration of SiR-DBCO increases, indicating the pre-mixed product does not localize on the plasma membrane.

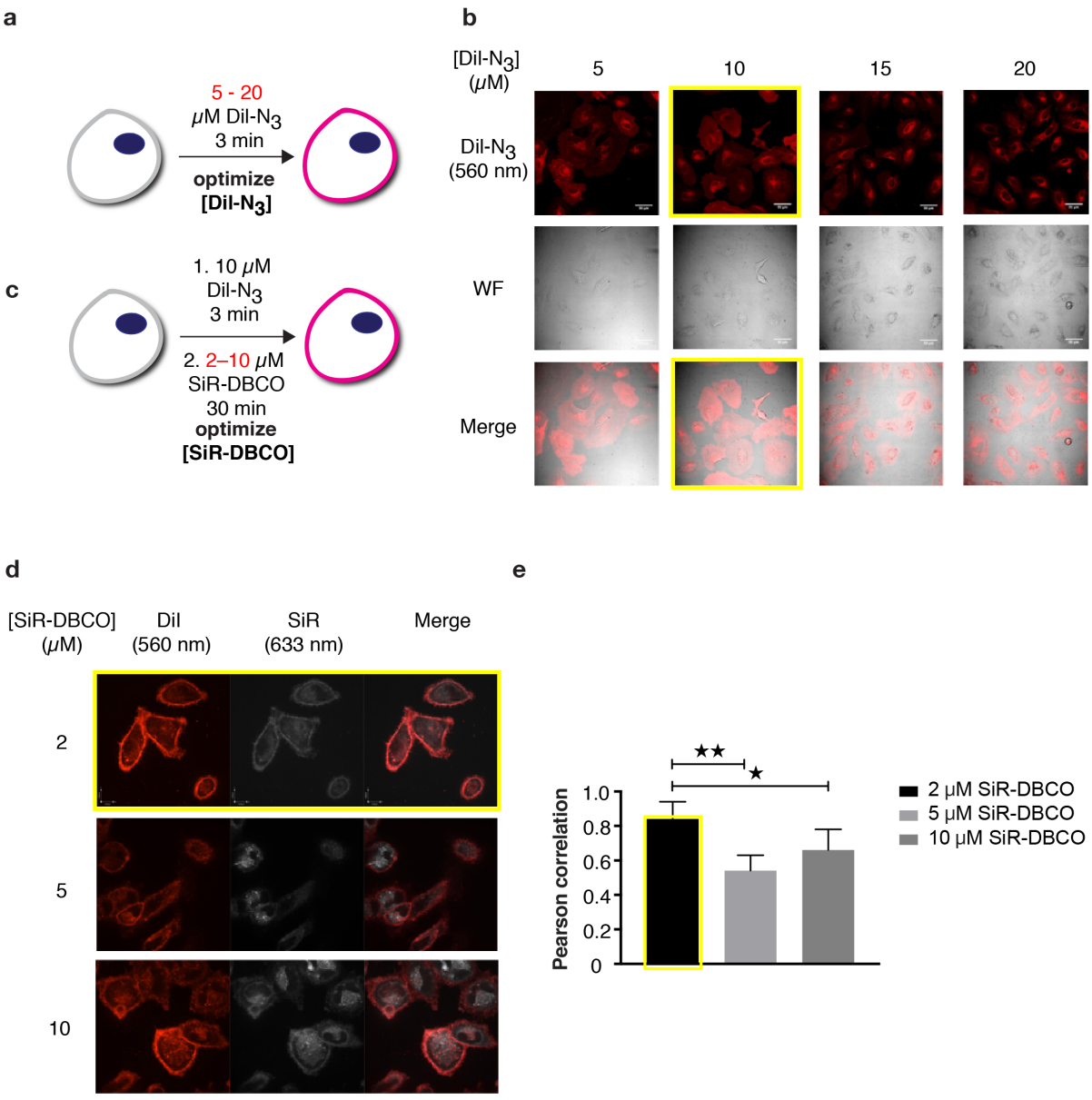

Supplementary Figure 4. Optimization of labeling conditions with DiI-N_3 and SiR-DBCO. (a) Schematic illustration of HeLa cells labeled with different concentrations of DiI-N_3 (b) Images of HeLa cells labeled with X μM DiI-N_3. When 5 μM DiI-N_3 was used, not all cells are universily labeled. When 15 or 20 μM DiI-N_3 was used, nonspecific labeling in the cytosol was observed. (c) Schematic illustration of HeLa cells labeled with 10 μM DiI-N_3 and different concentrations of SiR-DBCO. (d) Confocal images of HeLa cells labeled with 10 μM DiI-N_3 and different concentrations of SiR-DBCO. Images of both DiI (560 nm) channel and SiR (633 nm) channel was recorded. (e) Pearson correlation between DiI channel and SiR channel. (mean±SD, N = 5), ★P = 0.0328, ★★P = 0.0011.

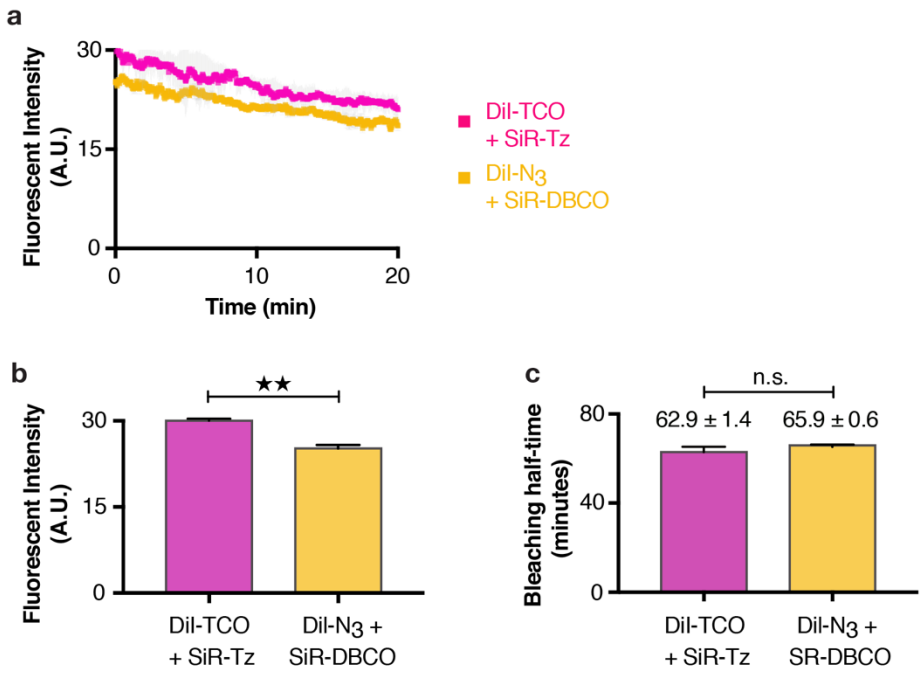

Supplementary Figure 5. Comparison of TCO-tetrazine ligation and Cu-free SPAAC click chemistry.
(a) Plot illustrating fluorescence intensity of HeLa cells labled with DiI-TCO+SiR-Tz or DiI-N_3+SiR-DBCO over time (mean±SD, n = 2 ROI, N = 1 cell). (c) Fluoresecent intensity of b at time 0. ★★P = 0.0096 (d) τ values calculated from a single exponential fit to the photobleaching curves in b (mean ± SD., n = 2 ROI, N = 1 cell). n.s. = not significant.

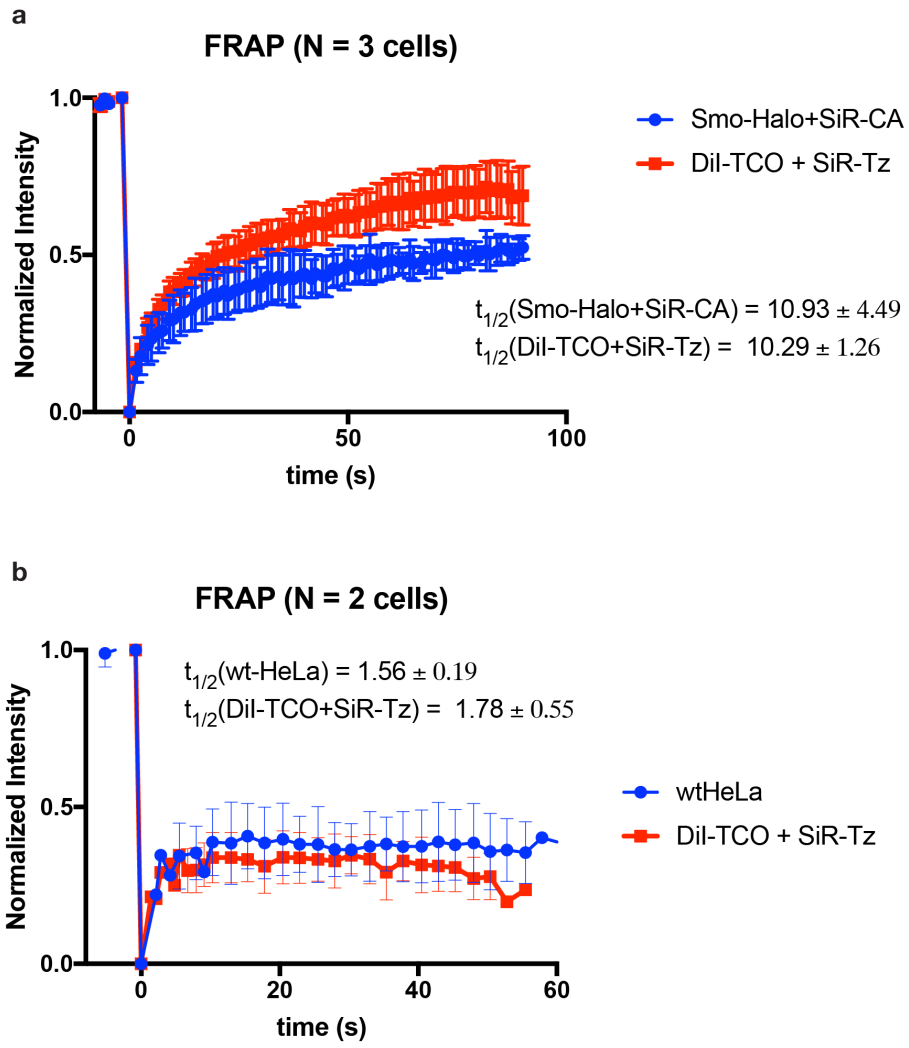

Supplementary Figure 6. Fluorescence recovery after photobleaching (FRAP) experiments. (a) Plot illustrating normalized fluorescence intensity of RPE cells labled with Smo-Halo+SiR-CA or DiI-TCO+SiR-Tz over time (mean±SD, N = 3 cells). RPE cells stably expressing Smo-Halo were labeled with either 2 μM SiR-CA or 10 μM DiI-TCO + 2 μM SiR-Tz and performed the FRAP experiment. Photobleaching was performed with the built-in FRAP unit. A region of interest was photobleached using 40 scans of the 650 nm laser (SiR channel) at 100% laser power. Images of a single XY-plane were taken at 0.8 Hz with an exposure time of 167 ms. Quantification was performed with Velocity. The resulting curves were fit to an exponential growth equation using Velocity Analysis. (b) Plot illustrating normalized fluorescence intensity of Laurdan (405 nm) of wild type HeLa cells or HeLa cells labled with DiI-TCO+SiR-Tz over time (mean±SD, N = 2 cells). HeLa cells labeled with either 5 μM Laurdan or 10 uM DiI-TCO + 2 uM SiR-Tz + 5 μM Laurdan. Photobleaching was performed with the built-in FRAP unit. A region of interest was photobleached using 40 scans of the 405 nm laser (Laurdan channel) at 100% laser power. Images of a single XY-plane were taken at 0.5 Hz with an exposure time of 210 ms. Quantification was performed with Velocity.

a

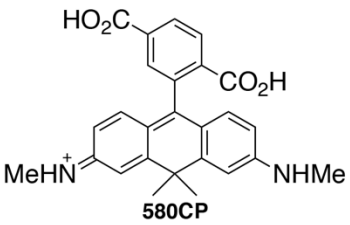

580CP

Angew. Chem. Int. Ed. 55, 3290 (**2016**)

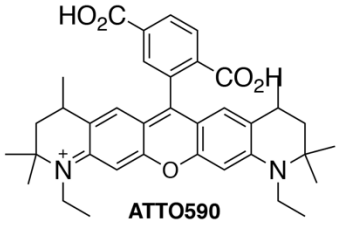

ATTO590

PMC Biophys. 3, 4 (**2010**); *Nat. Commun.* 7 (**2016**) DOI: 10.1038/ncomms10778

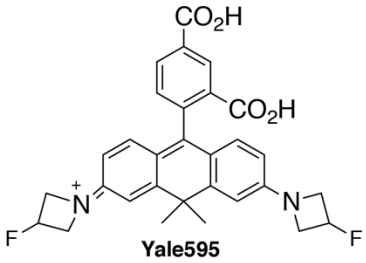

Yale595

This work

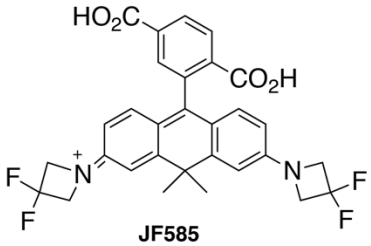

JF585

Nat. Methods 14, 987 (**2017**)

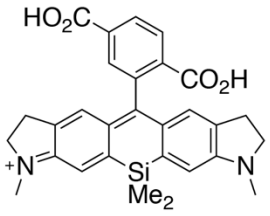

SiR700

J. Am. Chem. Soc. 138, 9365 (**2016**)

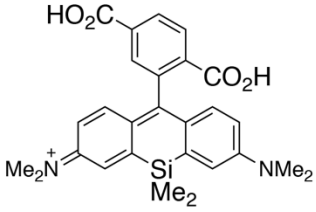

SiR

Nat. Chem. 5, 132 (**2013**)

b

Dye	Ex. (nm)	Em. (nm)	ε_{max} ($M^{-1}cm^{-1}$)	QY	Relative brightness
580CP	582	607	90000	0.69	1.55
ATTO590	593	622	120000	0.80	2.4
JF585	585	609	156000	0.78	3.05
SiR700	687	716	100000	0.13	0.33
Yale595	597	621	88000	0.76	1.67
SiR	645	677	100000	0.4	1

Supplementary Figure 7. Chemical structures of STED dyes used in this work. (a) Chemical structures and references. (b) Photophysical properties.

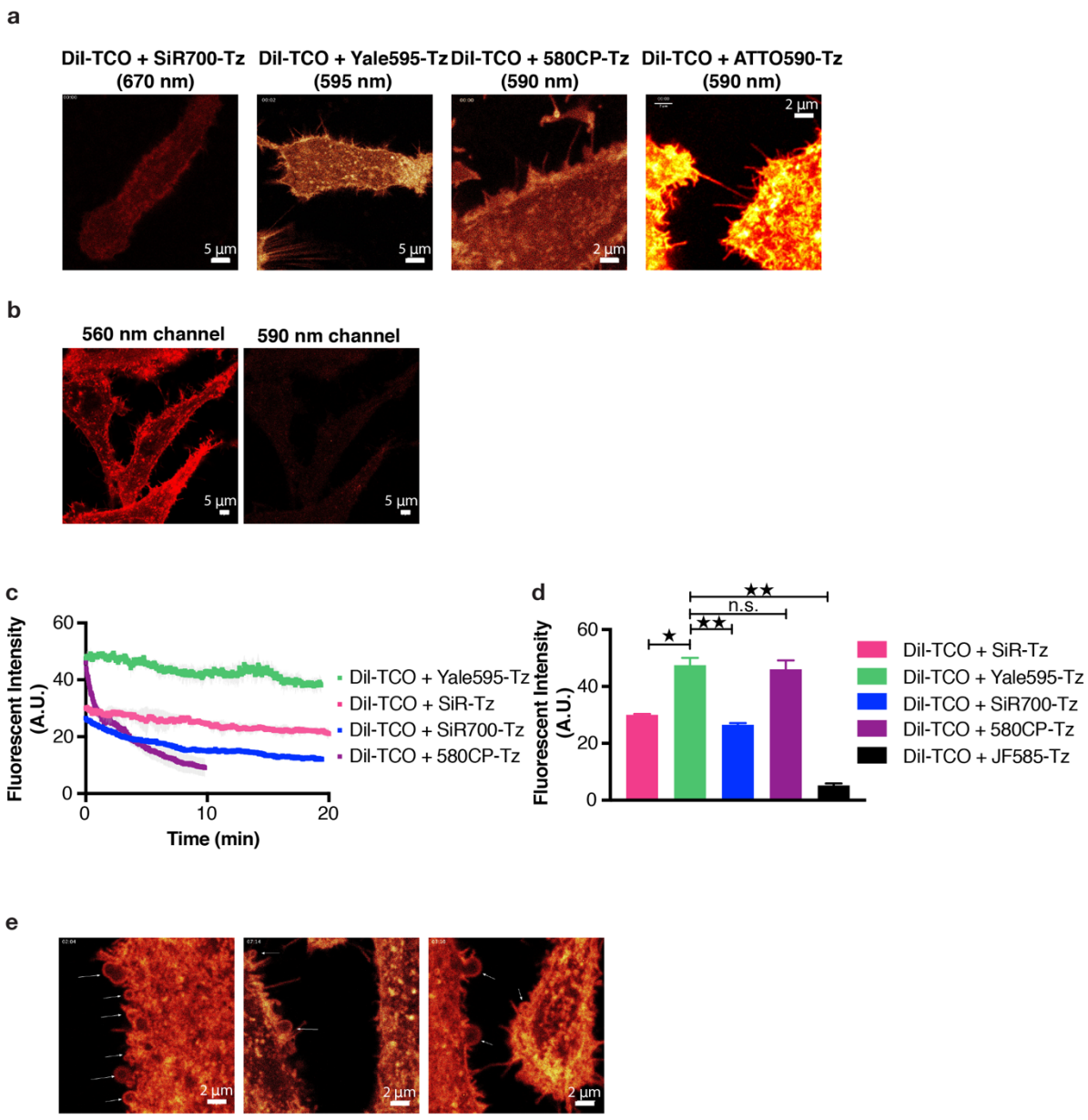

Supplementary Figure 8. Live-cell nanoscopy with Yale595, SiR700, CP580, Atto590, or JF585 (a) Representative images of plasma membrane labeled with DiI-TCO and Yale595-Tz, SiR700-Tz, 580CP-Tz, or Atto590-Tz. (b) Representative images of plasma membrane labeled with DiI-TCO and JF585-Tz. Image of DiI (560 nm) channel showed DiI-JF585 localized on the plasma membrane. Image of JF585 channel (590 nm) showed weak fluorescence. (c) Plot illustrating fluorescence intensity of 580CP (purple), SiR (red), SiR700 (blue) and Yale595 (green) over time (mean±SD, n = 2 ROI, N = 1 cell). (d) Fluoresecent intensity of d at time 0 (mean±SD, n = 2 ROI, N = 1 cell). ★P = 0.0108, ★★P (580CP) = 0.0078, ★★P (JF585) = 0.0020, n.s. = not significant. (e) Cell membrane blebbing when exiting Att0590-Tz. Cells were labeled with Atto590Tz followed by DiI-TCO and imaged by STED confocal microscopy (excitation at 595). As shown by the white arrows (three different cells) there was high toxicity as assessed by membrane blebs when using this dye.

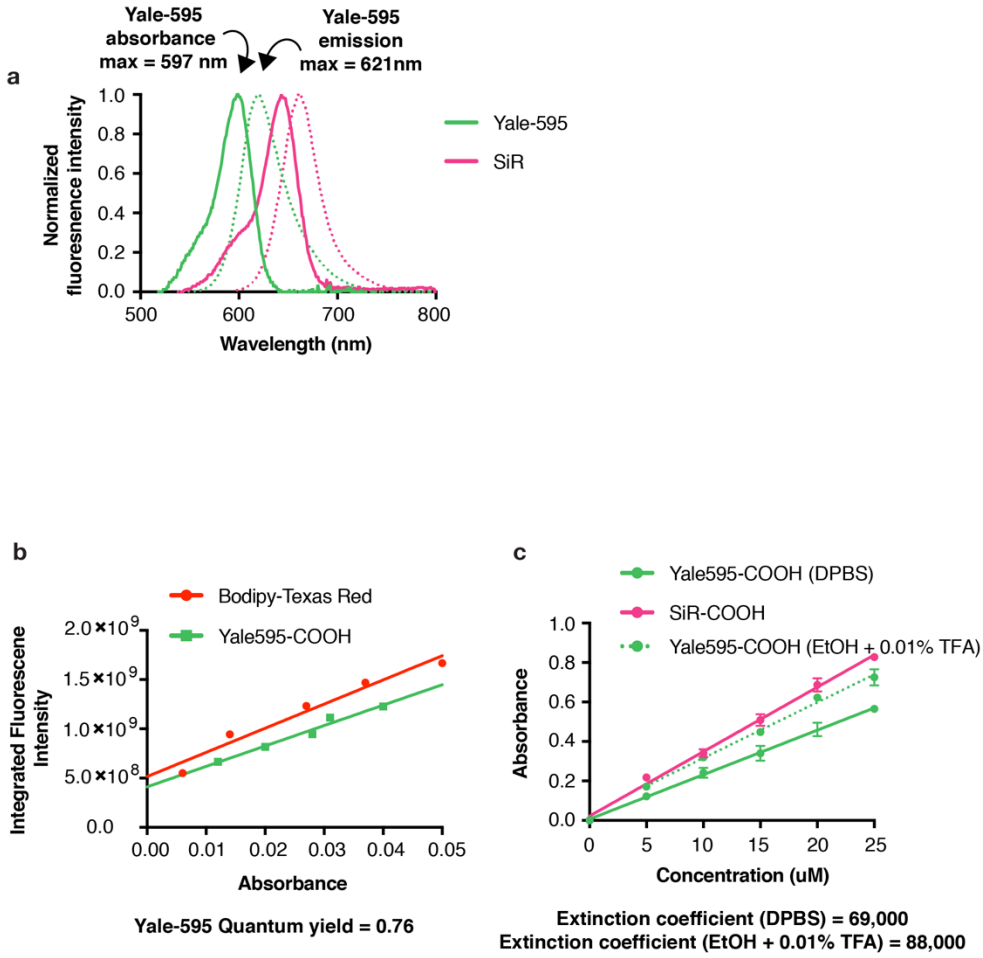

Supplementary Figure 9. Photophysical properties of Yale-595. (a) Fluorescence excitation (solid lines) and emission (dashed lines) spectra of Yale-595 (green) and SiR (pink). (b) Integrated fluorescence of Yale-595 (green) and Bodipy-Texas Red (red) as a function of absorbance at 550 nm. (c) Standard curve for Yale-595 (green) and SiR (pink) in DPBS (solid) or EtOH with 0.1% TFA (dash) (mean ± SD, N = 3).

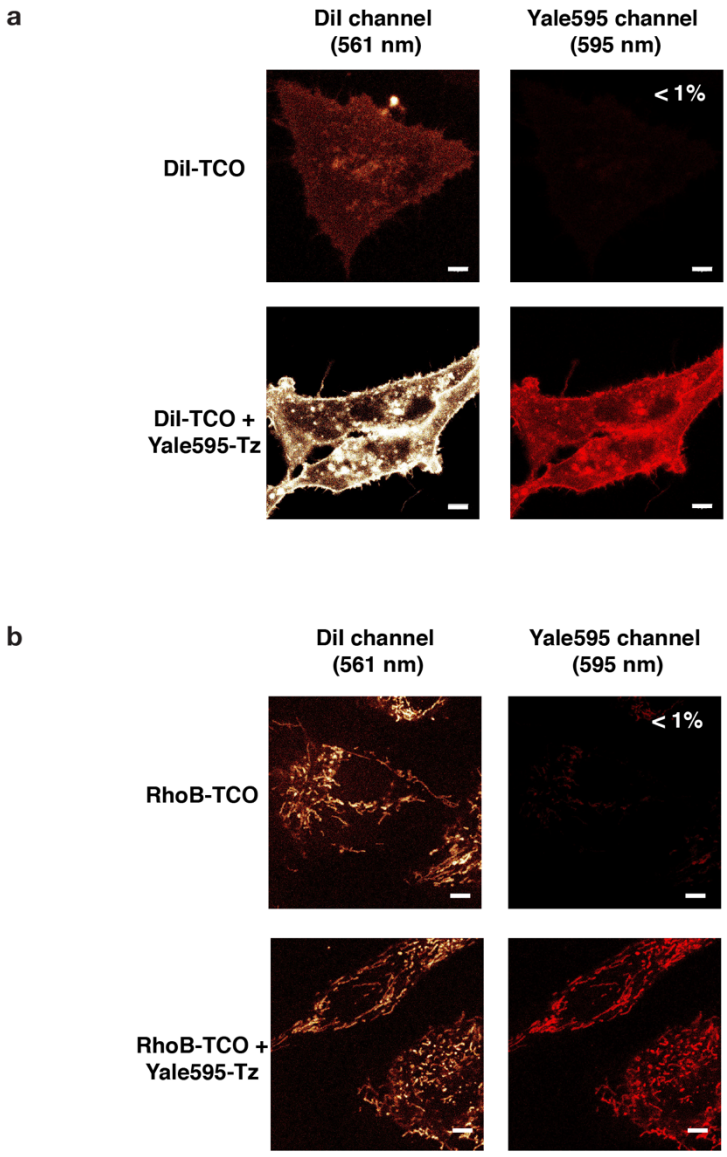

Supplementary Figure 11. Measurement of crosstalk between 561 nm and 595 nm channels. (a) Selected example illustrating mininal crosstalk of DiI-TCO in 595 nm channel. HeLa cells were labeled with either DiI-TCO alone (10 μM) or with DiI-TCO + Yale595-Tz (10 μM + 2 μM), and imaged in both the 561 nm channel (to detect DiI) and the 595 nm channel (to presumably detect only Yale-595) using the same STED setting described in the manuscript (10% 595 nm excitation, 30% 775 nm depletion, detection window: 605-625 nm). Scale bars: 10 µm.(b) Selected example illustrating mininal crosstalk of RhoB-TCO in 595 nm channel. HeLa cells were labeled with either RhoB-TCO alone (10 μM) or with RhoB-TCO + Yale595-Tz (10 μM + 2 μM), and imaged in both the 561 nm channel (to detect DiI) and the 595 nm channel (to presumably detect only Yale-595) using the same STED setting described in the manuscript (10% 595 nm excitation, 30% 775 nm depletion, detection window: 605-625 nm). Scale bars: 10 µm.

17

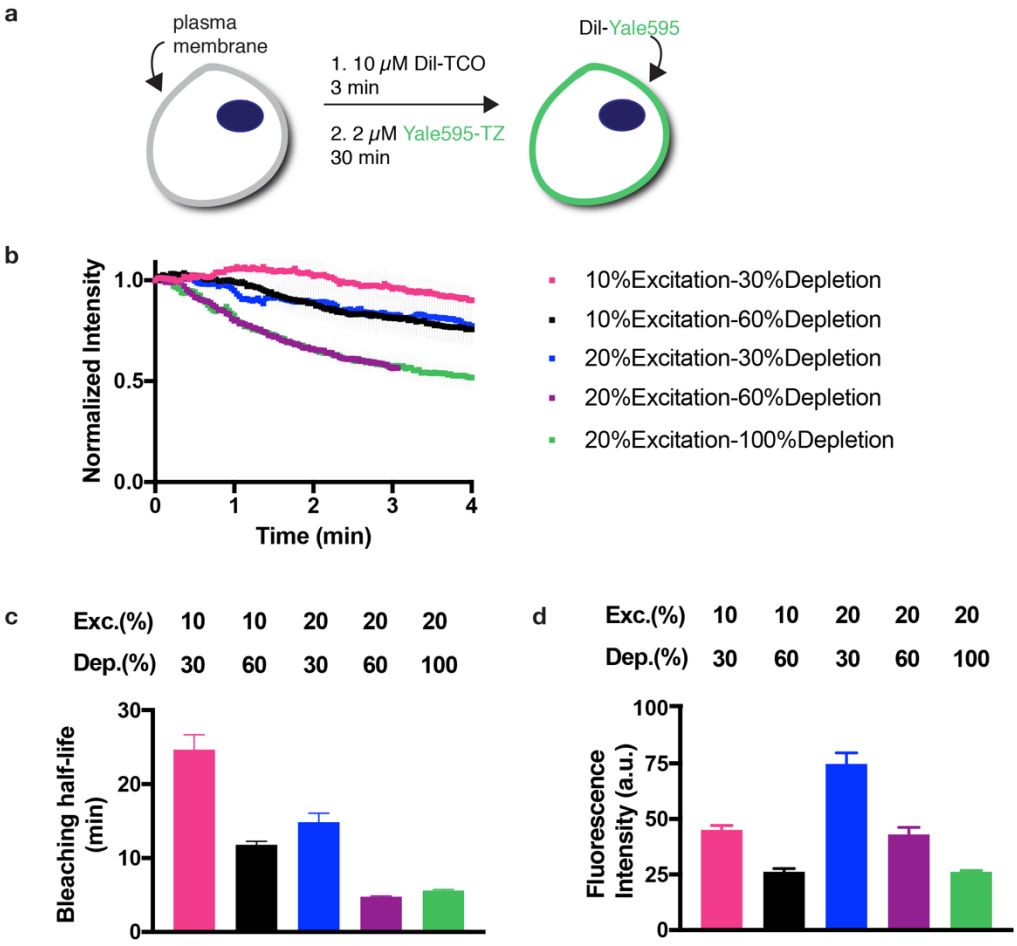

Supplementary Figure 12. Photobleaching curve of Yale595 under different imaging conditions. (a) Schematic illustration of HeLa cells labeled with DiI-TCO+Yale595-Tz. (b) Plot illustrating normalized fluorescence intensity of HeLa cells over time under different imaging conditions. (c) Bleaching half-life calculated from a single exponential fit to the photobleaching curves in b. (d) Initial fluorecence intensity of HeLa cells under different imaging conditions.

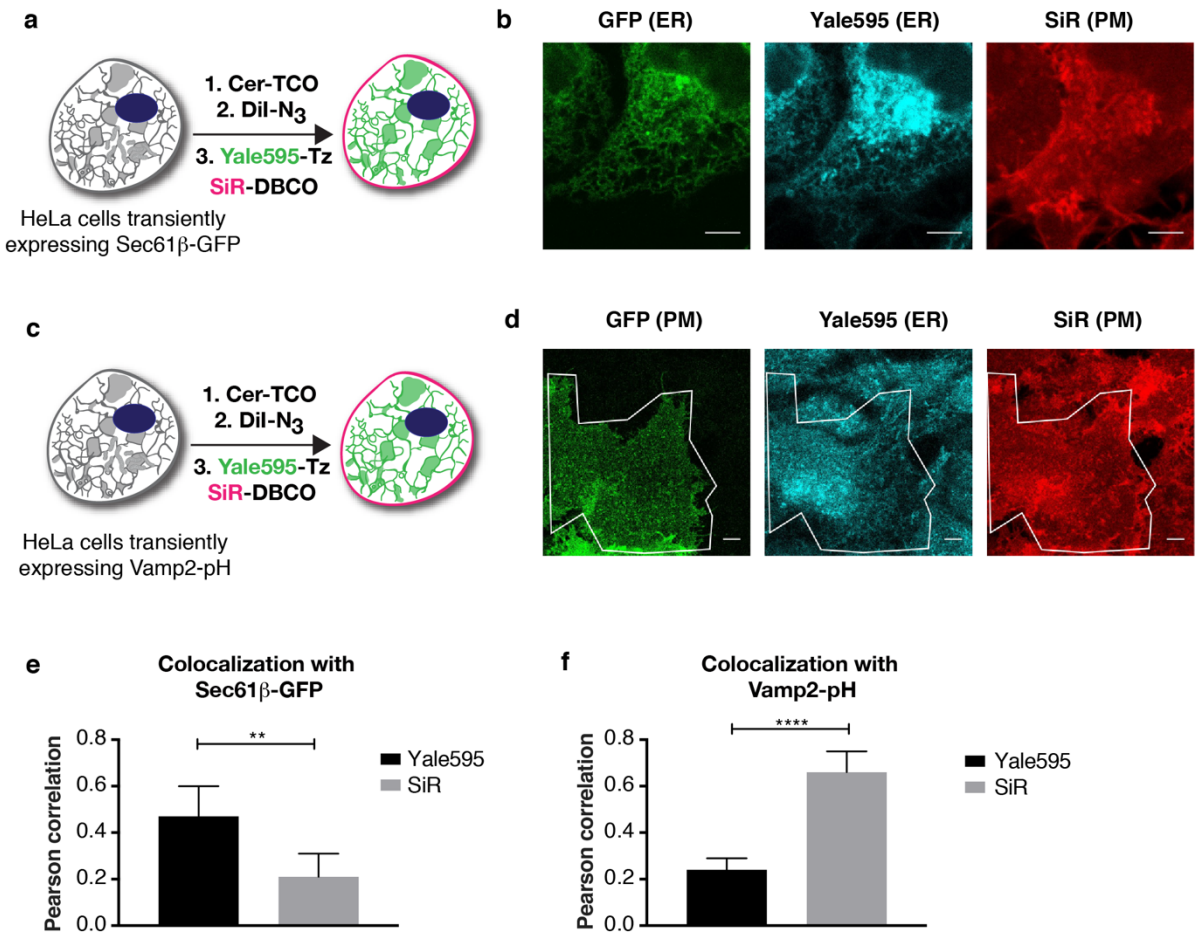

Supplementary Figure 13. Colocalization of two-color HIDE probe labeling of PM and ER with organelle marker
(a) Schematic illustration of HIDE probe PM and ER labeling of HeLa cells transiently expressing Sec61b-GFP. (b) Representative images of PM and ER labeling in three channels. Scale bars: 2 μm.(c) Schematic illustration of HIDE probe PM and ER labeling of HeLa cells transciently expressing Vamp2-pH. (d) Representative images of PM and ER labeling in three channels. Scale bars: 2 μm. (e) Cer-Yale595 still colocalize with Sec61b-GFP (ER marker) with two-color HIDE labeling protocol. (mean±SD, N = 5), **P = 0.0076. (f) DiI-SiR still colocalize with Vamp2-pH (PM marker) with two-color HIDE labeling protocol. (mean±SD, N = 5), ****P ≤ 0.0001.

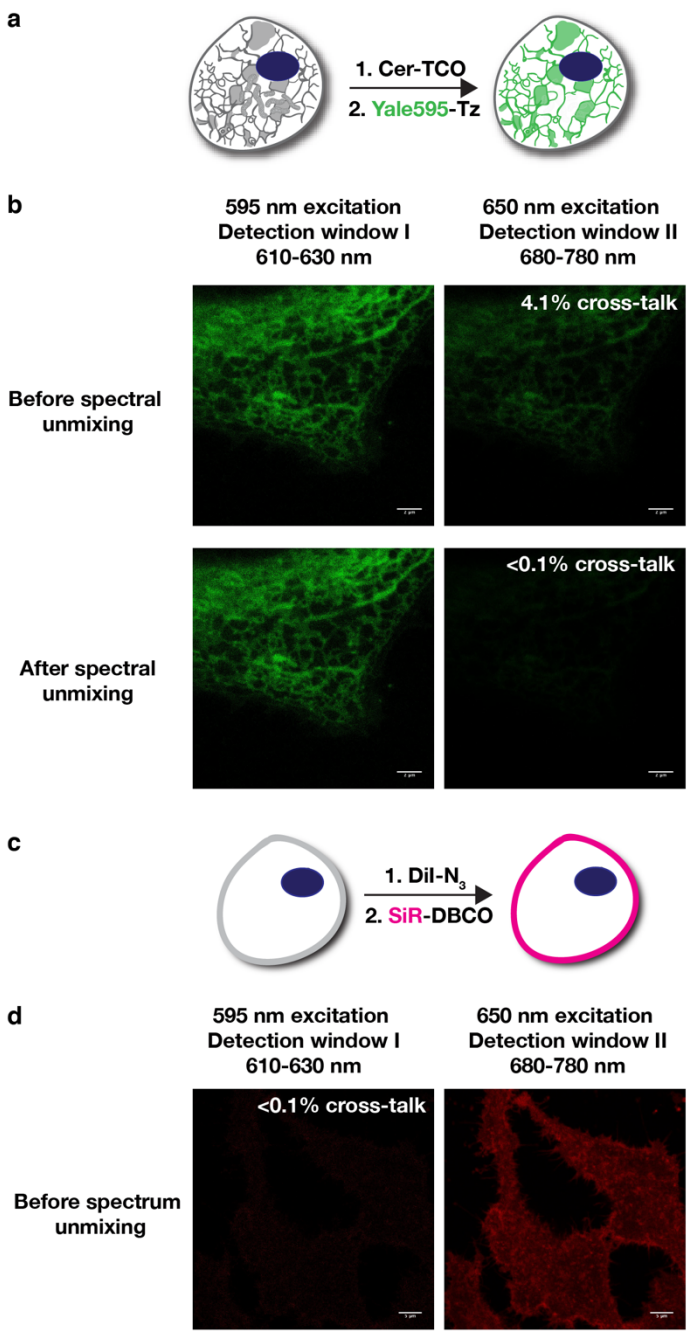

Supplementary Figure 14. Measurement of cross-talk between two channels. (a) Schematic illustration of ER labeled with Cer-TCO and Yale595-Tz. (b) STED Images of ER labeled with Cer-Yale595. Images in both 590 nm and 650 nm channel was recorded and cross-talk percentages was calculated as the ratio of fluorescent intensity between two channels. Spectral unmixing was done using a imagej plugin SpectrumUnmixing. Scale bars: 2 μm. (c) Schematic illustration of plasma membrane labeled with DiI-N_3 and SiR-DBCO. (d) STED Images of ER labeled with DiI-SiR. Images in both 590 nm and 650 nm channel was recorded. Scale bars: 5 μm.

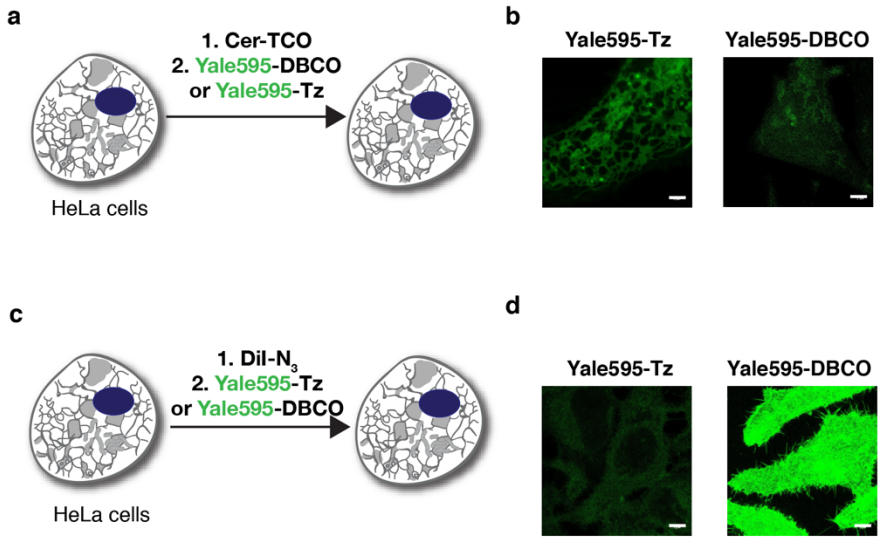

Supplementary Figure 15. Study of cross reactivity of different probes. (a) Schematic illustration of HeLa cells treated with Cer-TCO followed by Yale595-DBCO or Yale595-Tz. (b) Representative images of Yale595 channel (595 nm). Scale bars: 2 μm.(c) Schematic illustration of HeLa cells treated with DiI-N_3 followed by Yale595-Tz or Yale595-DBCO. (d) Representative images of Yale595 channel (595 nm). Scale bars: 5 μm.

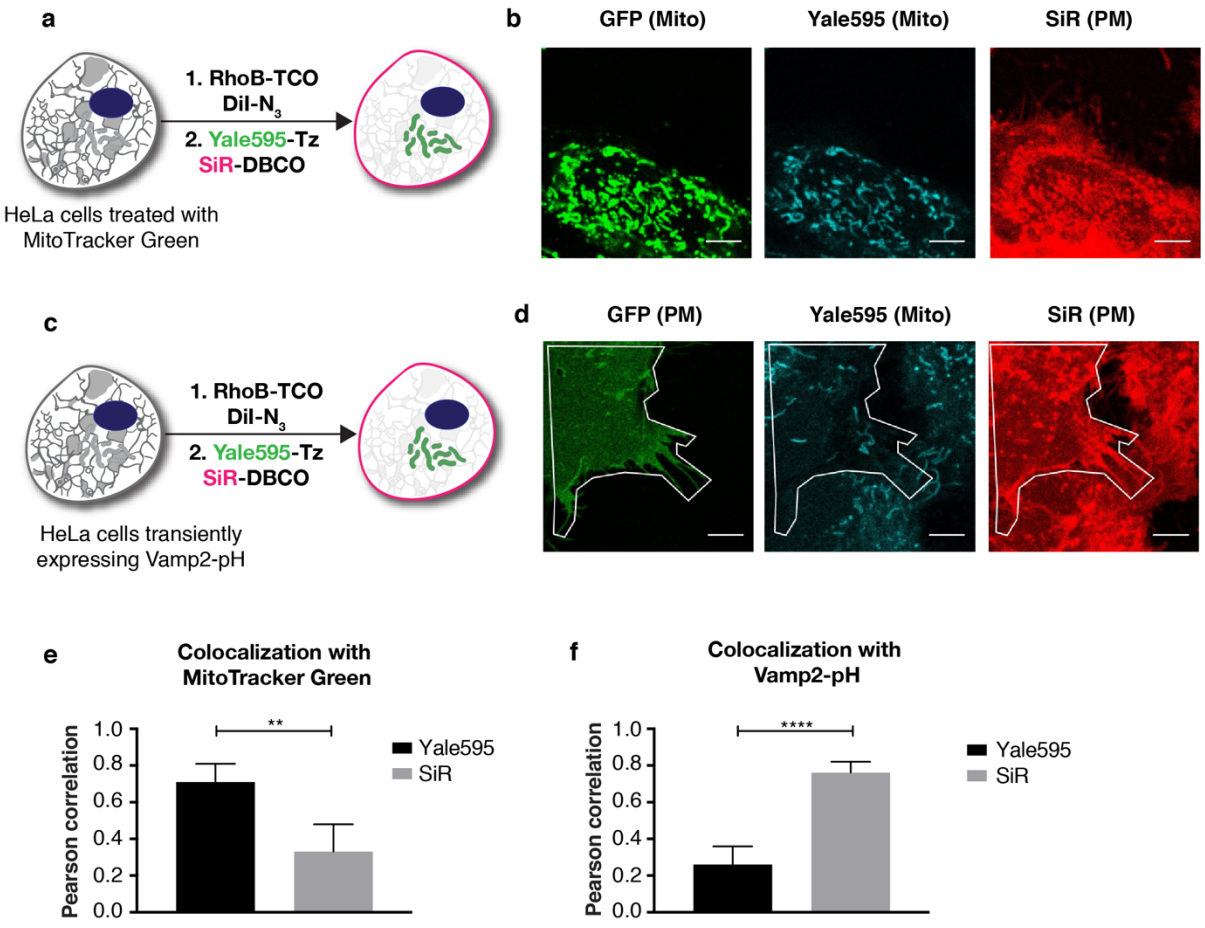

Supplementary Figure 16. Colocalization of two-color HIDE probe labeling of PM and Mitochondria with organelle marker. (a) Schematic illustration of HIDE probe PM and mitochondria labeling of HeLa cells treated with MitoTracker Green. (b) Representative images of PM and Mitochondria labeling in three channels. (c) Schematic illustration of HIDE probe PM and Mitochondria labeling of HeLa cells transiently expressing Vamp2-pH. Scale bars: 2 μm. (d) Representative images of PM and Mitochondria labeling in three channels. Scale bars: 2 μm.(e) RhoB-Yale595 still colocalize with MitoTracker Green with two-color HIDE labeling protocol. (mean±SD, N = 5), **P = 0.0015. (f) DiI-SiR still colocalize with Vamp2-pH (PM marker) with two-color HIDE labeling protocol. (mean±SD, N = 5), ****P ≤ 0.0001.

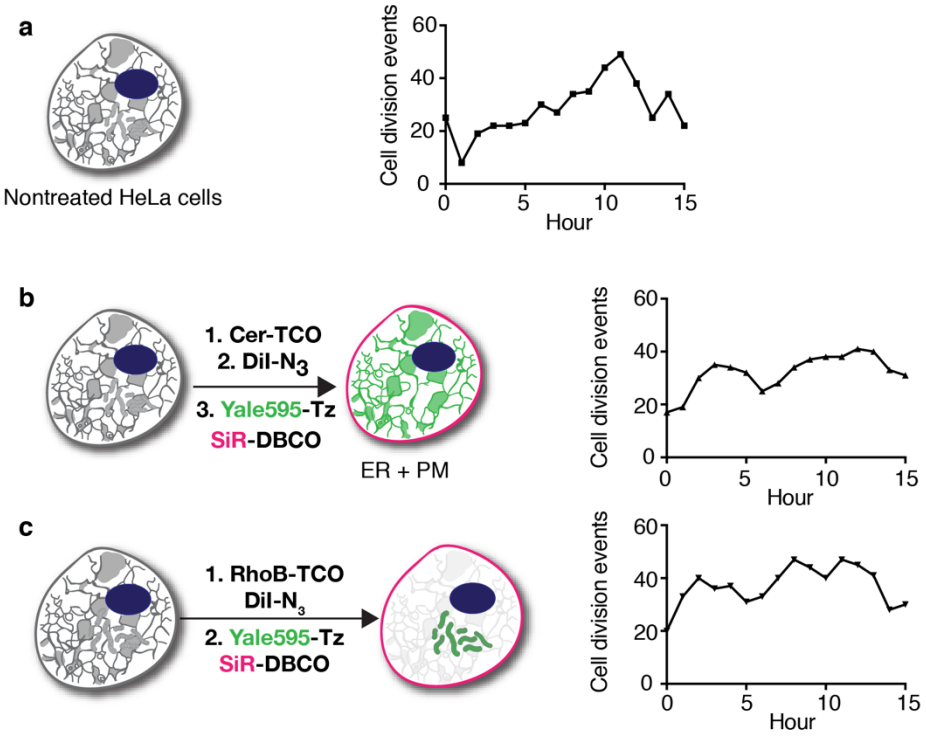

Supplementary Figure 17. Cell toxicity study of two-color HIDE probes. (a) Number of cell division events of nontreated HeLa cells. The cells were monitored by an Invitrogen™ EVOS™ FL Auto 2 Imaging system equipped with temperature, humidity, and atmosphere controls for live cell imaging. The sample was kept at 37 °C with 5% CO2 and imaged using a 20x objective and a Highsensitivity 1.3 MP CMOS monochrome camera (1,328 x 1,048 pixels) every 10 minutes for 15 h using bright field. Each timepoint indicates the number of cell division events in that hour. (b) Number of cell division events of HeLa cells treated with Cer-TCO and DiI-N_3 then Yale595-Tz and SiR-DBCO. Cells were washed and incubated in DMEM with 10% FBS before imaging. The imaging conditions were the same as in (a). (c) Number of cell division events of HeLa cells treated with RhoB-TCO and DiI-N_3 then Yale595-Tz and SiR-DBCO. Cells were washed and incubated in DMEM with 10% FBS before imaging. The imaging conditions were the same as in (a).

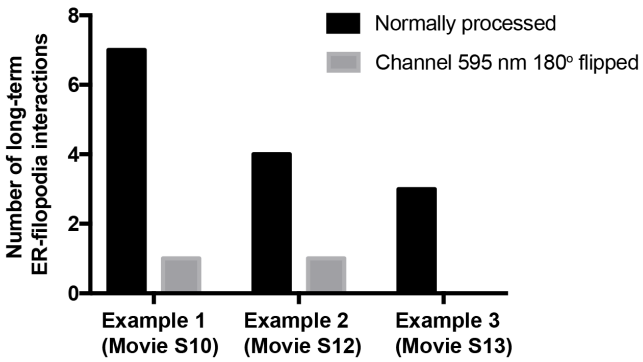

Supplementary Figure S18. Quantification of long-term ER-filopodia interactions. Black columns indicate the number of long-term ER-filopodia interactions that are preserved through out each movie. Gray columns indicate when the 595 nm channel was 180° flipped, the number of long-term ER-filopodia interacrtions that are preserved through out each movie.

2.4 References

1. Abbe, E. Beiträge zur Theorie des Mikroskops und der mikroskopischen Wahrnehmung. *Archiv. Mikrosk. Anat.* **9**, 413-418 (1873).
2. Sahl, S.J., Hell, S.W. & Jakobs, S. Fluorescence nanoscopy in cell biology. *Nat Rev Mol Cell Bio* **18**, 685-701 (2017).
3. Nixon-Abell, J. et al. Increased spatiotemporal resolution reveals highly dynamic dense tubular matrices in the peripheral ER. *Science* **354** (2016).
4. Oracz, J., Westphal, V., Radzewicz, C., Sahl, S.J. & Hell, S.W. Photobleaching in STED nanoscopy and its dependence on the photon flux applied for reversible silencing of the fluorophore. *Sci Rep-Uk* **7** (2017).
5. Erdmann, R.S. et al. Super-Resolution Imaging of the Golgi in Live Cells with a Bioorthogonal Ceramide Probe. *Angew Chem Int Edit* **53**, 10242-10246 (2014).
6. Thompson, A.D. et al. Long-Term Live-Cell STED Nanoscopy of Primary and Cultured Cells with the Plasma Membrane HIDE Probe DiI-SiR. *Angew Chem Int Edit* **56**, 10408-10412 (2017).
7. Takakura, H. et al. Long time-lapse nanoscopy with spontaneously blinking membrane probes. *Nat Biotechnol* **35**, 773-780 (2017).
8. Lukinavicius, G. et al. A near-infrared fluorophore for live-cell super-resolution microscopy of cellular proteins. *Nat Chem* **5**, 132-139 (2013).
9. Blackman, M.L., Royzen, M. & Fox, J.M. Tetrazine ligation: Fast bioconjugation based on inverse-electron-demand Diels-Alder reactivity. *J Am Chem Soc* **130**, 13518-13519 (2008).
10. Devaraj, N.K., Weissleder, R. & Hilderbrand, S.A. Tetrazine-Based Cycloadditions: Application to Pretargeted Live Cell Imaging. *Bioconjugate Chem* **19**, 2297-2299 (2008).
11. Han, Y.B., Li, M.H., Qiu, F.W., Zhang, M. & Zhang, Y.H. Cell-permeable organic fluorescent probes for live-cell long-term super-resolution imaging reveal lysosome-mitochondrion interactions. *Nat Commun* **8** (2017).
12. Chen, B.C. et al. Lattice light-sheet microscopy: Imaging molecules to embryos at high spatiotemporal resolution. *Science* **346**, 1257998 (2014).
13. Agard, N.J., Prescher, J.A. & Bertozzi, C.R. A strain-promoted [3+2] azide-alkyne cycloaddition for covalent modification of biomolecules in living systems (vol 126, pg 15046, 2004). *J Am Chem Soc* **127**, 11196-11196 (2005).
14. Debets, M.F. et al. Aza-dibenzocyclooctynes for fast and efficient enzyme PEGylation via copper-free (3+2) cycloaddition. *Chem Commun* **46**, 97-99 (2010).
15. Butkevich, A.N. et al. Fluorescent Rhodamines and Fluorogenic Carbopyronines for Super-Resolution STED Microscopy in Living Cells. *Angew Chem Int Edit* **55**, 3290-3294 (2016).
16. Bottanelli, F. et al. Two-colour live-cell nanoscale imaging of intracellular targets. *Nat Commun* **7** (2016).
17. Neumann, D., Buckers, J., Kastrup, L., Hell, S.W. & Jakobs, S. Two-color STED microscopy reveals different degrees of colocalization between hexokinase-I and the three human VDAC isoforms. *PMC Biophys* **3**, 4 (2010).

18. Grimm, J.B. et al. A general method to fine-tune fluorophores for live-cell and in vivo imaging. *Nat Methods* **14**, 987-994 (2017).
19. Lukinavicius, G. et al. Fluorogenic Probes for Multicolor Imaging in Living Cells. *J Am Chem Soc* **138**, 9365-9368 (2016).
20. Grimm, J.B. et al. A general method to improve fluorophores for live-cell and single-molecule microscopy. *Nat Methods* **12**, 244-250, 243 p following 250 (2015).
21. Phillips, M.J. & Voeltz, G.K. Structure and function of ER membrane contact sites with other organelles. *Nat Rev Mol Cell Bio* **17**, 69-82 (2016).
22. Murray, L.M.A. & Krasnodembskaya, A.D. Concise Review: Intercellular Communication Via Organelle Transfer in the Biology and Therapeutic Applications of Stem Cells. *Stem Cells* **37**, 14-25 (2019).
23. Rustom, A., Saffrich, R., Markovic, I., Walther, P. & Gerdes, H.H. Nanotubular highways for intercellular organelle transport. *Science* **303**, 1007-1010 (2004).
24. Kukic, I., Rivera-Molina, F. & Toomre, D. The IN/OUT assay: a new tool to study ciliogenesis. *Cilia* **5**, 23 (2016).

Chapter 3. Extremely bright, near-IR emitting spontanteously blinking fluorophores enable ratiometric multicolor nanoscopy in live cells

This chapter describes the the design, synthesis, and biological evaluation of Yale676sb, a photostable, near-IR emitting fluorophore that achieves these goals in the context of an exceptional quantum yield (0.59). When used alongside HMSiR, Yale676sb enables simultaneous, live-cell, two-color SMLM of two intracellular organelles (ER + mitochondria) with only a single laser and no chemical additives. This article was published as an article and is reproduced with permission: ***Tyson, J.**, Hu, K., Zheng, S., Kidd, P., Dadina, N., Chu, L., Toomre, D., Bewersdorf, J. & Schepartz, A. Bright, Near-IR Emitting Spontaneously Blinking Fluorophores Enable Ratiometric Multicolor Nanoscopy in Live Cells. ACS Cent. Sci. 2021, in press https://doi.org/10.1021/acscentsci.1c00670.*

3.1 Introduction

Single-molecule localization microscopy (SMLM)[1–4] is a powerful technique for visualizing intracellular architecture at the nanoscale[5] and across large field of view (FOV).[6] The technique is characterized by the detection and localization of fluorescent markers that cycle rapidly between emissive (ON) and non-emissive (OFF) states. For optimal results, the sample and imaging conditions must maintain the majority of fluorescent markers in the OFF state, such that the neighboring molecules in the emissive ON state can be treated as sparse single emitters.[7–11] Organic fluorophores are favored over fluorescent proteins for SMLM because they are generally brighter, more photostable, and because their photophysical properties can be fine- tuned using chemistry.[7,12–17,17–21] The challenge is that many SMLM-compatible organic fluorophores require the addition of exogenous nucleophiles, redox modulators, and/or oxygen depletion systems to switch efficiently between ON and OFF states. These additives can be cytotoxic and damage or alter biological samples.[7,12,13,15,17] An additional challenge is that many established SMLM-compatible fluorophores are cell-impermeant[7,12,13,20,22,23] and/or require cytotoxic high-power and/or short-wavelength lasers.[7,12,16,18,22,24,25]

The spontaneously blinking fluorophore (SBF) hydroxymethyl Si-rhodamine (HMSiR)[15] (Figure 1A) reported by Urano and coworkers overcomes many of these limitations. It is cell-permeant, photostable, and has been proposed to cycle rapidly between ON and OFF states by virtue of a pH-dependent spirocyclization reaction that occurs in the absence of chemical additives[15] (Figure 1A). For HMSiR, the midpoint of this pH-dependent equilibrium (referred to as pK_{cycl}) occurs at approximately pH 6.0. Thus, at pH 7.4 roughly 98% of the HMSiR molecules in solution occupy the OFF state, which enables facile detection and localization of the sparse subset of molecules that are emissive (ON).[15] HMSiR's cell permeability, photostability, and ability to blink in the absence of chemical additives has enabled multiple minimally invasive single-color SMLM experiments, including those that visualize organelle membrane dynamics in live cells for extended times,[26] others that resolve the morphology of dopaminergic neurons in an intact *Drosophila melanogaster* adult brain,[27] and still others that enable turn-on visualization of intracellular protein targets.[28]

Despite these advances, there remains a need for new SBFs that effectively partner with HMSiR to enable multicolor live-cell SMLM experiments without the need for chemical additives or photoactivation[13]. Although two green-emitting SBFs whose emission spectra are separable from HMSiR have been reported (Figure 1B),[18,19] including one (HEtetTFER) that can be paired with HMSiR for two-color SMLM in fixed cells,[18] their use demands high-intensity lasers that excite at 488 and 561 nm, respectively, which can

induce substantial cytotoxicity as phototoxicity is especially pronounced in the blue and green spectrum.[14] Two other previously reported SBFs are excitable in the far-red/near-IR (Figure 1C),[20,21] but they are spectrally indistinguishable from HMSiR and are therefore not suitable for two-color experiments. Although both the fluorescent protein mEos3.2 as well as CP550 (Figure 1D), a carbopyronin fluorophore that reacts irreversibly with intracellular glutathione[20] have been paired with HMSiR for two-color live cell SMLM,[15,20] these experiments require an additional ~560 nm laser, which is inferior to red-light excitation for live-cell microscopy.[10,14] Furthermore, sequential multi-color imaging with multiple lasers is slow, making it more prone to sample motion artifacts. Finally, the spontaneously blinking carborhodamine, HMCR550, which was designed using quantum calculations, has an excitation maximum at 560 nm and would likewise require multiple lasers to pair with HMSiR (650 nm excitation) for a two-color live cell SMLM experiment.

Here we report the rational design of a new near-IR emitting SBF that pairs effectively with HMSiR to enable simplified two-color SMLM experiments in live cells (Figure 1D). Yale676sb emits at 694 nm, the longest wavelength of any reported SBF, and possesses, to our knowledge, a higher quantum yield (0.59) than any previously reported nanoscopy-compatible Si-rhodamine (SiR) fluorophore. Yale676sb and HMSiR can be excited simultaneously with a single 642-nm laser and imaged ratiometrically for simultaneous multicolor SMLM of two distinct intracellular organelles (ER + mitochondria) in live cells.

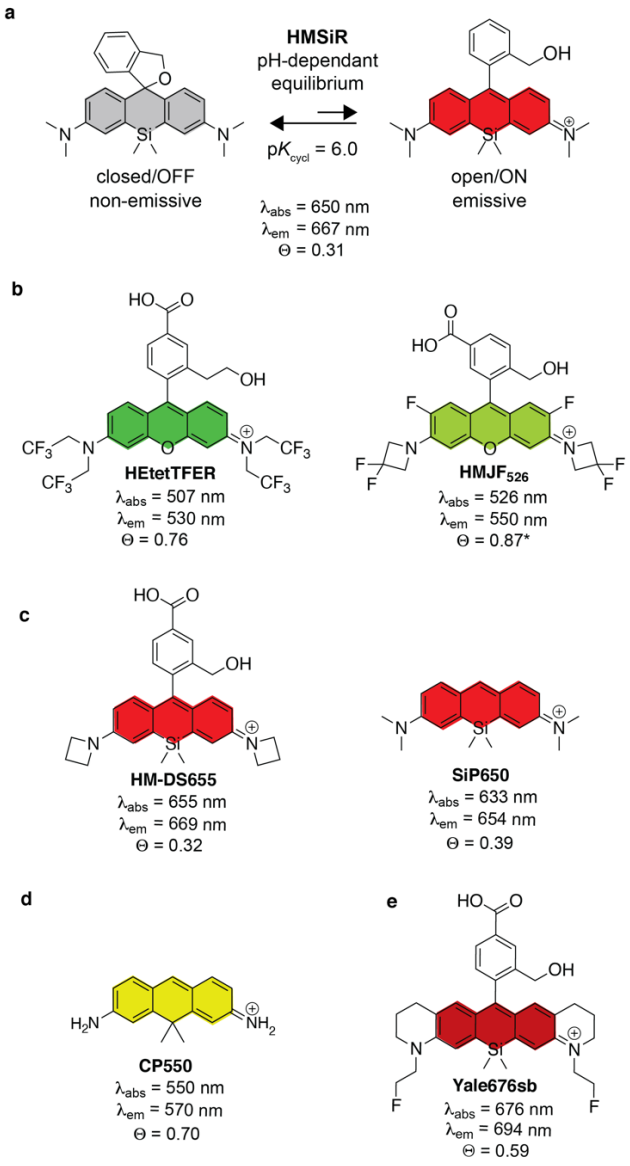

Figure 3.1. (A) Structure and pH- dependent equilibrium of the spontaneously blinking fluorophore HMSiR.[15] (B-D) Structures of previously reported fluorophores considered as potential HMSiR partners for multicolor live-cell SMLM[16,18,21,29] (E) Structure of the spontaneously blinking fluorophore reported herein, Yale676sb.

3.2 Results

3.2.1 New spontaneously blinking fluorophores: Design considertations

Three distinct chemical and photophysical properties are needed to ensure compatibility with HMSiR for ratiometric two- color, live-cell SMLM. The first is an emission maximum >690 nm to ensure adequate separation from HMSiR (emission maximum = 670 nm) *via* ratiometric imaging.[5,30,31] The second is a pK_{cycl} value between 5.3 and 6.0 to ensure the sparsity of emissive/ON molecules.[15,21] The third requirement is a high quantum yield; although a quantum yield >0.2 can yield respectable SMLM images, higher values are always more desirable.[13,22] The challenge is that the quantum yields of rhodamine-based fluorophores typically decrease as the absorption and emission maxima increase (Supplemental Figure 1). As a result, molecules that absorb and emit at higher, less cytotoxic wavelengths that are compatible with live-cells are relatively dim. This correlation is reflected in the relatively low quantum yield of HMSiR (0.31) when compared to those of the green-light emitting SBFs HMJF526 (0.87)[16] and HEtetTFER (0.76)[18]. We therefore sought a design approach that would yield fluorophores possessing both long-wavelength emission and high quantum yield.

3.2.2 HMSiR$_{indol}$, HMSiR$_{julol}$, and HMSiR$_{THQ}$

Previous work has demonstrated that introduction of heterocyclic indoline[32,33], julolidine[34], or tetrahydroquinoline[32] moieties into the core of a SiR chromophore can shift the excitation and emission maxima by up to 50 nm relative to SiR itself (Figure 2A). To evaluate whether these effects would be preserved in the context of a HMSiR core, we synthesized HMSiR, as well as the heterocyclic derivatives HMSiR$_{indol}$, HMSiR$_{julol}$, and HMSiR$_{THQ}$ (Figure 2B and Supplementary Schemes 1-4) according to a recently reported general method for Si-rhodamine fluorophore synthesis.[35] We then characterized the photophysical properties and aqueous spirocyclization equilibrium (pK_{cycl}) of each new fluorophore (Figure 2B-D).

Each of the new fluorophores displayed absorption (Figure 2B) and emission (Figure 2C) maxima that were red-shifted by at least 23 nm relative to HMSiR, with the emission maxima increasing in the order HMSiR < HMSiR$_{THQ}$ < HMSiR$_{julol}$ < HMSiR$_{indol}$. As expected, the absorption and emission maxima of the HMSiR series were nearly identical to those of the analogous SiR variants reported previously.[32–34] The pK_{cycl} of each new HMSiR analog was determined from a plot of the pH-dependence of the absorption of each fluorophore at the absorption maximum of the open/ON form (Figure 2D and Supplementary Figure 2); the pK_{cycl} is the pH at which the concentration of the open/ON state equals that of the closed/OFF state.[15]

The pK_{cycl} values of HMSiR$_{indol}$ and HMSiR$_{THQ}$ were 6.4 and 6.9, respectively, both significantly higher than the value for HMSiR (6.0). The pK_{cycl} value of HMSiR$_{julol}$ (pK_{cycl} = 9.0) was shifted even more dramatically, presumably because the additional electron-donating alkyl groups disfavor cyclization. A related previously reported rhodamine analog with julolidine groups also displayed a high p$K_{cycl.}$ value.[15] The absorbance *versus* pH curves for HMSiR$_{indol}$, HMSiR$_{julol}$, and HMSiR$_{THQ}$ are sigmoidal, whereas that of HMSiR is bell-shaped due to cyclization of the protonated fluorophore at low pH; this protonation is disfavored when the exocyclic amine is constrained by a 5- or 6-membered ring.[15,36]

The final criterion needed to ensure compatibility with HMSiR for ratiometric two-color, live-cell SMLM is a high quantum yield. The quantum yields measured for HMSiR$_{indol}$, HMSiR$_{julol}$, and HMSiR$_{THQ}$ also paralleled the values for the analogous SiR variants; the quantum yield of HMSiR$_{indol}$, like SiR700, was low (0.13), whereas those of HMSiR$_{julol}$ and HMSiR$_{THQ}$ (0.43 and 0.38, respectively) were comparable to that of HMSiR (0.31) (Supplementary Figure 3).

These data indicate that neither HMSiR$_{THQ}$, HMSiR$_{julol}$, nor HMSiR$_{indol}$ possess the characteristics necessary to partner with HMSiR for two-color SMS nanoscopy. Although all three fluorophores exhibit emission maxima that are shifted by at least 23 nm from that of HMSiR, and HMSiR$_{julol}$ and HMSiR$_{THQ}$ display acceptable quantum yields (0.43 and 0.38), none feature pK_{cycl} values low enough to prevent significant multi-emitter artifacts at physiological pH. In each case, chemical modifications are needed to increase the electrophilicity of the xanthene core, favor spirocyclization, and decrease pK_{cycl}. Ideally, these modifications should also increase quantum yield to increase brightness and resolution, but as outlined below, this goal is complicated by the complex interplay between emission maximum, pK_{cycl} and quantum yield.

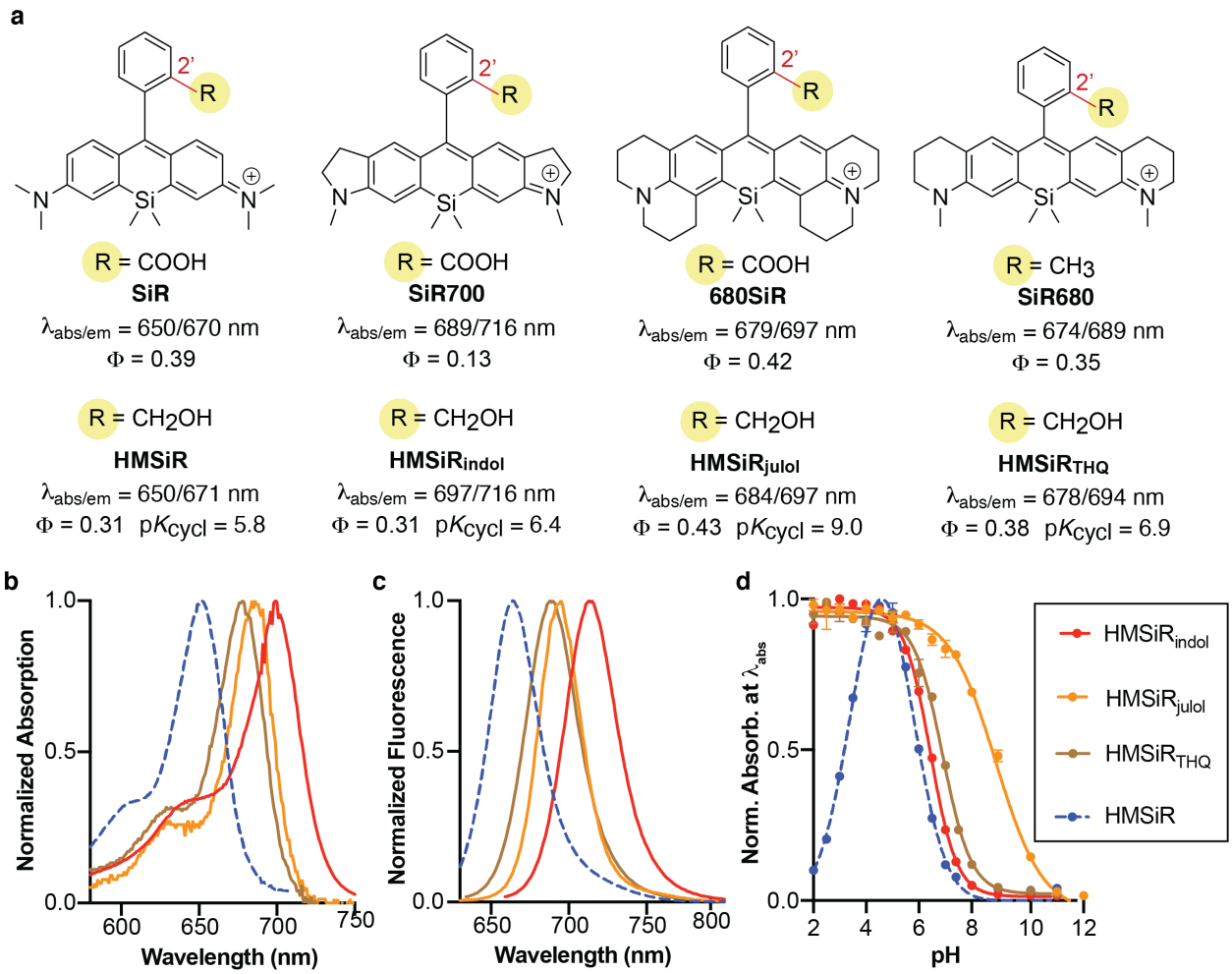

Figure 3.2. (A) Structures and photophysical properties (ƛabs, ƛem, and ϕ) of previously reported SiR fluorophores with red-shifted absorption and emission spectra and HMSiR analogs HMSiR, HMSiRindol, HMSiRjulol, and HMSiRTHQ. Normalized (B) absorption and (C) emission spectra of HMSiR, HMSiRindol, HMSiRjulol, and HMSiRTHQ in 0.2 M sodium phosphate (pH = 4.5 for HMSiR, pH = 2.0 for HMSiRindol, HMSiRjulol and HMSiRTHQ). (D) pH-dependent change in absorbance of 2 μM HMSIR (650 nm), HMSiRindol (697 nm), HMSiRjulol (684 nm), and HMSiRTHQ (678 nm) as a function of pH in 0.2 M sodium phosphate buffer at room temperature. The absorbance of each fluorophore was monitored at the wavelength of maximal absorbance in (B).

3.2.3 Interplay between emission maximum, p*K*cycl and quantum yield. The quantum yields of rhodamine fluorophores are limited by a non-radiative decay process known as twisted intramolecular charge transfer (TICT)[37–39]. TICT involves the excited-state transfer of an electron from the exocyclic nitrogen of the fluorophore to the neighboring carbon pi system with concomitant twisting of the C_{aryl}-N bond; the charge-separated state subsequently decays to the ground state without emission of a photon. Processes that decrease the C_{aryl}-N bond rotation increase the quantum yield. For example, the quantum yields of rhodamine B and tetramethyl rhodamine (TMR) are higher in viscous solvents[37] and at low temperature where C_{aryl}-N bond rotation is inhibited[37,40]. Indeed, the modestly increased quantum yields of HMSiR$_{julol}$ (0.43) and HMSiR$_{THQ}$ (0.38) relative to HMSiR (0.31) can also be ascribed to restricted C_{aryl}-N bond rotation[34], although these effects appear to be less dramatic in the SiR series than with conventional rhodamines: Rhodamine 101, the rhodamine analog of HMSiR$_{julol}$, displays a near- perfect quantum yield of 0.99.[40]

TICT is also inhibited in fluorophores in which the ionization potential (IP) of the exocyclic nitrogen is increased by electron-withdrawing groups (EWGs).[18,38,41] Addition of EWGs to a fluorophore core also decreases pK_{cycl} by lowering the energy of the fluorophore's lowest unoccupied molecular orbital (LUMO).[15,18] However, addition of EWGs typically induces moderate to large decreases in excitation and emission wavelength maxima. For example, an EWG-containing fluorophore reported by Lv *et al.* possesses an exceptional quantum yield (0.66) but is blue-shifted by ~20 nm relative to HMSiR ($\lambda_{abs}/\lambda_{em}$ = 631/654 nm).[41] We hypothesized that combining the effects of restricted aryl-N bond rotation with an EWG would simultaneously reduce pK_{cycl} and increase quantum yield by inhibiting TICT. If these changes were introduced into the HMSiR$_{THQ}$ scaffold, even a moderate decrease in excitation and emission maxima would not jeopardize the emission shift needed to remain orthogonal to HMSiR. HMSiR$_{THQ}$ was preferred as a starting point because its pK_{cycl} (6.9) and quantum yield (0.38) are both close to that of HMSiR, in contrast to HMSiR$_{indol}$, whose quantum yield is low (0.13) or HMSiR$_{julol}$, whose pK_{cycl} is very high (9.0).

3.2.4 Design of the bright, near-IR emitting SBF, Yale$_{676sb}$. To test this hypothesis, we synthesized Yale$_{676sb}$, a variant of HMSiR$_{THQ}$ in which two N-methyl groups were replaced symmetrically by mono-fluorinated N-ethyl groups (Figure 3 and Supplementary Scheme 5). As predicted, Yale$_{676sb}$ was characterized by a 10-fold more favorable spirocyclization equilibrium than HMSiR$_{THQ}$ (pK_{cycl} = 5.9 *vs.* 6.9) and a greatly improved quantum yield (0.59 *vs.* 0.38) (Supplementary Figure 3). Interestingly, Yale$_{676sb}$ exhibited absorption and emission λ_{max} that are both virtually identical to those of HMSiR$_{THQ}$. Addition of a stronger di-fluorinated N-ethyl group to generate Cal$_{664sb}$ resulted in a further increase in quantum yield to 0.74 (Supplementary Figure 3), but in

this case led to an emission λ_{max} that was too close to that of HMSiR (667 nm *vs.* 677 nm) to support two-color ratiometric imaging. These photophysical properties associated with Yale676sb suggest that it should be an ideal partner for HMSiR: an emission maximum >690 nm, a pK_{cycl} value between 5.3 and 6.0, and a high quantum yield. The quantum yield of Yale676sb (0.59) is, to our knowledge, higher than any Si-rhodamine derivative prepared and utilized for fluorescence nanoscopy. To deconvolute the effects of aryl-N bond rotation and the mono-fluoro electron withdrawing group, we also prepared HMSiR2-FlEt, which carries the same mono-fluorinated N-ethyl groups but allows aryl-N bond rotation (Supplementary Scheme S7). HMSiR2-FlEt was characterized by a minimal change in absorption and emission λ_{max} relative to HMSiR; however, it displayed a 10-fold more favorable spirocyclization equilibrium than HMSiR (pK_{cycl} = 5.0 *vs.* 6.0), a value too low for efficient blinking at physiological pH of 7.4.[21] Its improvement in quantum yield was more modest relative to Yale676sb (0.51 vs 0.59). These comparisons emphasize the benefits of combining restricted aryl-N bond rotation with an EWG.

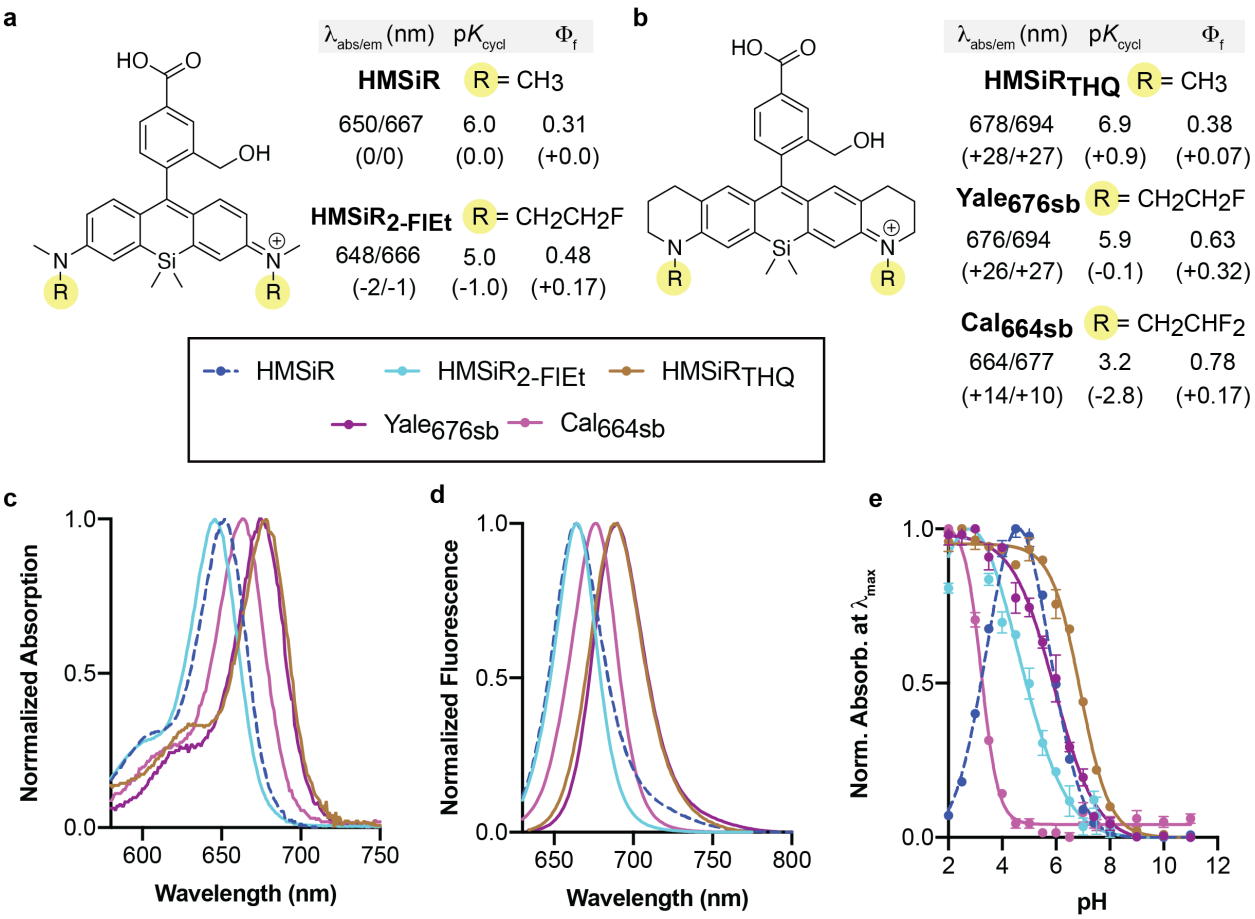

Figure 3.3. Structures and photophysical properties (ƛabs, ƛem, and ϕ) of (A) HMSiR, HMSiR2-FlEt, (B) HMSiRTHQ Yale676sb and Cal664sb. Normalized (C) absorption and (D) emission spectra of HMSiR, HMSiRindol, HMSiRjulol, and HMSiRTHQ in 0.2 M sodium phosphate (pH = 4.5 for HMSiR, pH = 2.0 for HMSiRindol, HMSiRjulol and HMSiRTHQ). € pH-dependent spirocycliation equilibria. Normalized absorptions of open form of 2 μM HMSiR, HMSiR2-FlEt, HMSiRTHQ,Yale676sb and Cal664sb as a function of pH in 0.2 M sodium phosphate buffer at room temperature.

3.2.5 Evaluation of the single molecule properties of Yale676sb. To ensure that the bulk photophysical parameters of Yale676sb would translate into efficient single-molecule parameters, we evaluated its properties under SMLM imaging conditions. We quantified the 'on-time' to determine the dye's compatibility with HMSiR by imaging single dye molecules immobilized on glass coverslips (Supplementary Figure 4). By monitoring individual molecules, we were able to determine the on-time to evaluate the compatibility of Yale676sb and HMSiR. Because both dyes are imaged on the same camera using ratiometric imaging, similar on-times allow a single camera integration time to acquire data effectively from both fluorophores.[42] From these data, we determined that Yale676sb has an on-time of 4.5 ms at pH 7.4, which is close to the ~10 ms on-time reported for HMSiR, and in theory should allow even faster imaging.[15] This short on- time, combined with the high quantum yield, also makes the Yale676sb/HMSiR combination suitable for high-speed imaging, with camera frame rates as high as 400 frames per second (fps). With an off-time of 3.8 s, we expect an on-fraction or duty cycle of 0.0012.

3.2.6 Single-color live-cell SMLM with Yale676sb. We next tested whether Yale676sb would support single-color, live-cell SMLM imaging. U2-OS cells that were engineered to overexpress the endoplasmic reticulum (ER)-localized protein Halo-Sec61β[43] were treated with 300 nM Yale676sb- CA (Supplementary Scheme S8) for 30 min, then washed and immersed in a standard live-cell imaging solution using a custom-built SMLM instrument (see Supplementary Methods). Figure 4A shows a representative super-resolution image (out of n = 16 images) acquired over 5 seconds. These images revealed multiple tubules in the cell periphery that were ~99 ± 15 nm (mean ± s.d.) wide, a value comparable to ER morphology metrics acquired using both STED and 4Pi-SMS.[44] A time series illustrates changes in ER morphology that occur over the course of 10 seconds (Figure 4B). On average, we detected ~800 photons per blink, corresponding to a localization precision distribution with a peak at ~20 nm (Figure 4C, D).

3.2.7 Ratiometric two-color live-cell SMLM with Yale676sb and HMSiR. Next we sought to evaluate whether Yale676sb would support live-cell multicolor imaging in combination with HMSiR. U2-OS cells were transiently transfected with Halo-Sec61β (to reveal the ER) and SNAP-OMP25 (to reveal the outer mitochondrial membrane), treated with Yale676sb-CA and HMSiR-BG, and imaged using the identical SMLM setup. As predicted from the absorption and emission maxima of Yale676sb and HMSiR, both dyes could be excited with the same 642-nm laser and ratiometrically separated from two simultaneously acquired images detecting the emission wavelength ranges of 650-680 nm and 680-750 nm, respectively (Supplementary Figure 5). Figure 4E shows a resulting two-color super-resolution image, accumulated over 5 s, revealing the intertwined mitochondrial and ER networks of the cell. We detected comparable average photon numbers per frame for the two dyes (~500 and 590 photons for Yale676sb and HMSiR, respectively), especially given that the filters and excitation wavelength were optimized for HMSiR.

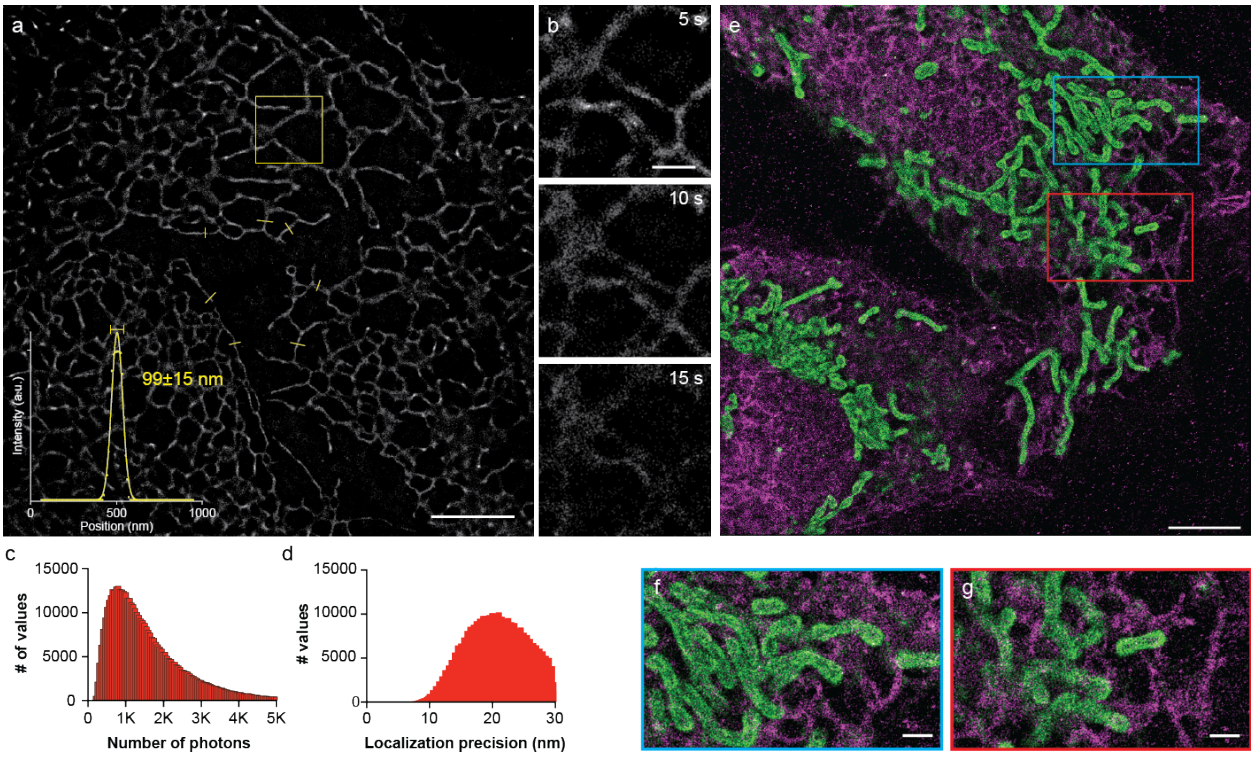

Figure 3.4. (A) Super-resolution image of the ER in U2-OS cells using Yale676sb. Average reconstructed signal as a function of position along the seven line profiles indicated by yellow lines is shown. Inset (B) shows dynamic ER network remodeling. Histograms illustrating the range in the number of photons (C) and localization precision (D) associated with single- molecules in (A). (E) Two-color super-resolution image of the ER and mitochondria in U2-OS cells using Yale676sb (magenta) in conjunction with HMSiR (green). Insets (F-G) show super- resolved mitochondrial and ER networks in close proximity. Scale bars 5 µm for (A) and (E), 1 µm for (B) and (F). All reconstructions using 5 s of acquired frames.

3.3 Conclusions

In summary, here we report a new spontaneously blinking Si-rhodamine, Yale676sb that can be used alongside HMSiR to enable two-color ratiometric SMLM in living cells in physiological media. This new experiment was facilitated by three unique photophysical metrics associated with Yale676sb: (1) an exceptionally high quantum yield for a silicon rhodamine derivative (0.59); (2) an unusually long emission maximum (694 nm); and (3) a pK_{cycl} value (5.9) that is nearly identical to that of HMSiR (6.0).

The unique photophysical metrics associated with Yale676sb result from the simultaneous introduction of *both* heterocyclic rings *as well as* electron withdrawing dialkyl amino groups (DAGs) into the silicon rhodamine core. When either of these structural features is introduced in isolation, at least one of the three critical photophysical metrics required for two-color SMLM becomes non-optimal. Silicon-rhodamine dyes with only heterocycle-containing dialkyl amino groups (such as HMSiR$_{indol}$, HMSiR$_{THQ}$ and HMSiR$_{julol}$) display long wavelength emission (689 – 716 nm) but resist spirocyclization. As a result, their pK_{cycl} values (6.4 – 9.0) are too high to ensure adequate distribution of single-molecule emitters (Figure 2). By contrast, silicon rhodamine dyes with only electron-withdrawing substituents, such as HMSiR2-FlEt, display a high quantum yield, but their spirocyclization equilibrium is too favorable, and their pK_{cycl} values are too low (Figure 3). By combining these two substitution patterns in Yale676sb, the competing effects on pK_{cycl} are balanced, while the redshift from the heterocycle-containing DAG is maintained (Figure 3). Moreover, because both the rotational restriction from the heterocycle- containing DAGs and the electron-withdrawing capacity of the 2-fluoroethyl substituent inhibit twisted intramolecular charge transfer (TICT), the quantum yield increase from the latter is not only maintained, but enhanced (0.51 vs 0.59).

As expected, switching from a 2-fluoroethyl to a more electron-withdrawing 2'2-difluoroethyl substituent at the nitrogen in Cal664sb further increases the quantum yield, though at the expense of both pK_{cycl} and emission wavelength (Figure 3). This pattern would likely continue with increasingly electron-withdrawing substituents. Despite these blue-shifts, Cal664sb displays a comparable quantum yield to a previously reported and exceptionally bright Si-rhodamine fluorophore (compound **9** in reference 41), but with a >30 nm longer emission maximum.[41]

Finally, we note that while the quantum yield increase relative to HMSiR observed with HMSiR$_{2\text{-}FlEt}$ is not as dramatic as that observed with Yale676sb, it is comparable to that observed from more commonly used azetidinyl substituents.[16,35,38,46,47] Being that the former requires only one position at each aniline nitrogen to be substituted, whereas the latter requires two, use of the 2- fluoroethyl substituent may serve as an alternative method for increasing quantum yield of rhodamine derivatives, especially those with more complex DAGs. This approach and others described herein may serve as versatile methods for the preparation of even more greatly enhanced fluorescent labels.

3.4 Methods

3.4.1 Materials and general information. Chemicals used for synthesis were purchased from commercial sources and used without further purification. Flash chromatography was performed using a Teledyne Isco CombiFlash Rf using pre-packed columns with RediSep Rf silica (40–60 μm). ^{1}H NMR and ^{13}C NMR spectra were recorded on either an Agilent DD2 NMR spectrometer (400 or 500 MHz for ^{1}H and 100 or 125 MHz for ^{13}C) or Bruker NEO500 NMR spectrometer (500 MHz for ^{1}H and 125 MHz for ^{13}C). The values of chemical shifts (δ) are reported in p.p.m. relative to the solvent residual signals of CD_3OD (3.31 p.p.m. for ^{1}H, 49.00 p.p.m. for ^{13}C), $CDCl_3$ (7.26 p.p.m. for ^{1}H, 77.36 p.p.m. for ^{13}C) or $(CD_3)_2O$ (2.05 p.p.m. for ^{1}H, 29.84, 206.26 p.p.m. for ^{13}C). Coupling constants (*J*) are reported in Hz. High-resolution mass spectra (HRMS) were recorded on an Agilent 6530QTOF LCMS. HPLC purifications were performed on a reverse-phase column (GL Sciences, Inertsil ODS-3 10 mm × 250 mm and Inertsil ODS-3 20 mm × 250 mm) using a HPLC system composed of a pump (Jasco PU-2080 or PU-2087) and a detector (Jasco MD-2010 or MD-2018).

3.4.2 Note on the preparation of NMR samples of Yale$_{676sb}$ and HMSiR Derivatives To simplify the ^{1}H and ^{13}C NMR spectra of fluorophores **7**, **11**, **15**, **19**, a single drop of NaOD was added to the NMR sample to fully shift the pK_{cycl} equilibrium of each into the non-emissive closed/OFF form.

3.4.3 Synthesis of HMSiR

Supplementary Scheme S1. Synthesis of HMSiR

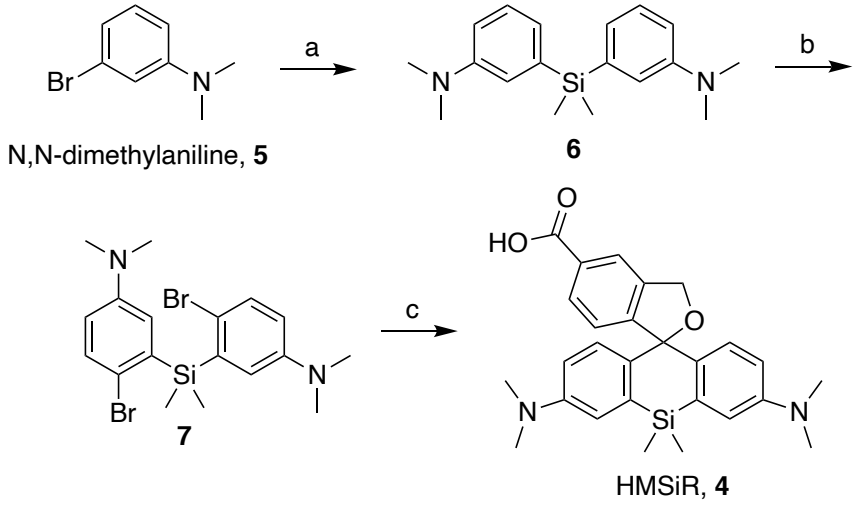

a) n-BuLi, Me_2SiCl_2, -78 ˚C to RT, b) NBS, DMF, RT,
c) i. tert-BuLi, **3**, -78 ˚C to RT, ii. TFA, RT

***tert*-butyl-1-oxo-1,3-dihydroisobenzofuran-5-carboxylate 3.**

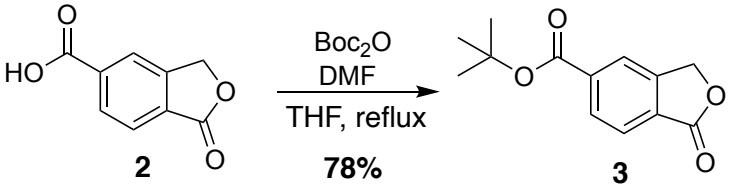

5'-carboxyphthalide **2** (1.0 g, 2.81 mmol, 1 equiv), $(Boc)_2O$ (3.2 g, 7.02 mmol, 2.5 equiv) and DMAP (140 mg, 0.56 mmol, 0.2 equiv) were dissolved in dry THF (15 mL) and heated to reflux overnight. After cooling to room temperature and evaporation of solvent, the residue was dissolved in Et_2O, washed with saturated aqueous $NaHCO_3$, water, and brine, dried over Na_2SO_4, filtered, and evaporated. The residue was purified by flash column chromatography on silica (100% hexanes to EtOAc: hexanes 70:30) to obtain **3** as a white powder (78%). ^{1}H-NMR (MeOD, 500 MHz) δ 8.21 (s, 1 H), 8.17 (d, *J* = 8.0 Hz, 1 H), 7.96 (d, *J* = 8.0 Hz, 1 H), 5.45 (s, 2 H), 1.64 (s, 9 H). ^{13}C-NMR (MeOD, 125 MHz) δ 164.5, 147.4, 137.2, 129.6, 128.7, 124.8, 123.3, 82.0, 70.1, 26.9. HRMS calc'd for $C_{13}H_{15}O_4$ $[M+H]^+$ *m/z* 235.0942, found 235.0971.

3,3'-(dimethylsilanediyl)bis(*N*,*N*-dimethylaniline) 6.

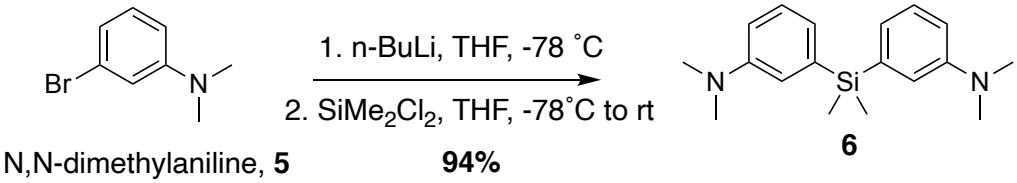

3-bromo-N,N-dimethylaniline **5** (5.0 g, 25 mmol, 2.4 equiv) was dissolved in THF (45 mL) in a flame dried round bottom flask and cooled to -78 °C under nitrogen. *n*-Butyllithium (2.5 M in cyclohexane, 10.0 mL, 25 mmol, 2.4 eq) was added and the reaction was stirred at -78 °C for 30 min. Dichlorodimethylsilane (1.26 mL, 10.42 mmol) in THF (5 mL) was then added, the dry ice bath was removed, and the reaction was stirred at room temperature for 3 h. Once no remaining starting material was detectable by TLC analysis, the reaction was quenched with saturated NH_4Cl, diluted with water, and extracted twice with EtOAc. The combined organic extracts were washed with brine, dried over anhydrous Na_2SO_4, filtered, and concentrated under vacuum. The crude product was purified by flash chromatography on silica (100% hexanes to EtOAc:hexanes 15:85) to yield **6** as a faintly colored oil (94%). ^{1}H-NMR ($CDCl_3$, 400 MHz) δ 7.23 (t, *J* = 7.2 Hz, 2 H), 6.92 (m, 4 H), 6.76 (dd, 8.4, 1.6 Hz), 4.60 (t, *J* = 6.0 Hz, 2 H), 4.48 (t, *J* = 6.0 Hz, 2 H), 3.57 (t, *J* = 5.2 Hz, 2 H), 3.51 (t, 5.2 Hz, 2 H), 3.35 (t, *J* = 5.2 Hz, 4 H), 2.91 (s, 12 H), 0.52 (s, 6 H); ^{13}C NMR ($CDCl_3$, 100 MHz) δ 152.2, 141.2, 130.7, 125.1, 120.6, 115.9, 55.6, 43.0, 0.0. HRMS calc'd for $C_{18}H_{27}N_2Si$ $[M+H]^+$ *m/z* 299.1944, found 299.2323.

3,3'-(dimethylsilanediyl)bis(4-bromo-*N,N*-dimethylaniline) 7.

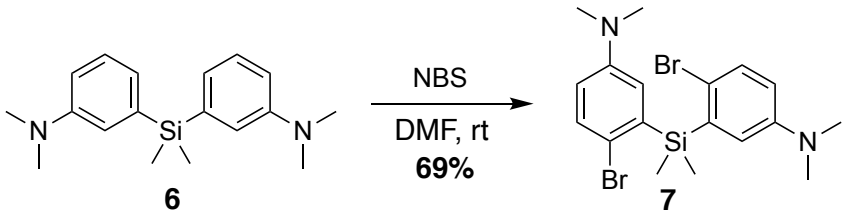

Silane **6** (1.0 g, 3.35 mmol) was taken up in DMF (22 mL). N-Bromosuccinimide (1.2 g, 6.70 mmol, 2.0 equiv) was added portionwise over 5 min. The reaction was stirred at room temperature overnight. Product formation was confirmed by LCMS, and then the resulting residue was concentrated in vacuo, diluted with water and extracted twice with EtOAc. The combined organic extracts were washed with water and brine, dried over anhydrous $MgSO_4$, filtered, and concentrated in vacuo. Silica gel chromatography (100% hexanes to EtOAc:hexanes 15:85) afforded **7** as a white solid (69%). ^{1}H-NMR ($CDCl_3$, 500 MHz) δ 7.27 (d, *J* = 8.6 Hz, 2 H), 6.77 (d, *J* = 3.3 Hz, 2 H), 6.54 (dd, J = 8.6, 3.2 Hz, 2 H), 2.80 (s, 12 H), 0.69 (s, 6 H). ^{13}C NMR ($CDCl_3$, 125 MHz) δ 149.7, 139.7, 134.0, 122.8, 117.9, 116.4, 41.6, 0.0. HRMS calc'd for $C_{18}H_{25}Br_2N_2Si$ $[M+H]^+$ *m/z* 455.0154, found 455.0198.

HMSiR 4.

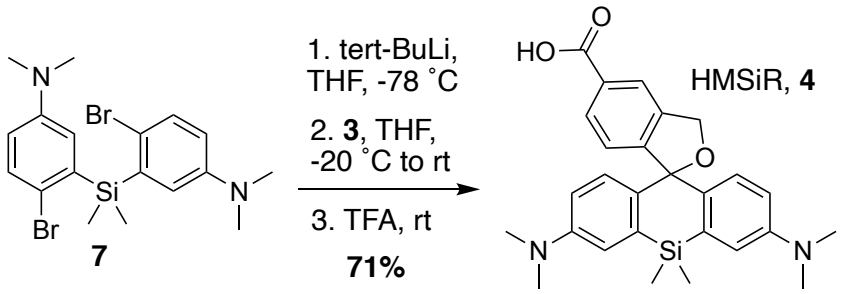

A solution of dibromide **7** (192 mg, 0.42 mmol) in THF (10 mL) in a flame-dried round bottom flask was cooled to -78 °C under nitrogen. *tert*-Butyllithium (1.7 M in pentane, 1.10 mL, 1.85 mmol, 4.4 eq) was added, and the reaction was stirred at -78 °C for 30 min. The reaction was warmed to -20 °C and then a solution of **3** (216 mg, 0.93 mmol, 2.2 eq) in THF (10 mL) was added dropwise over 30 min. The reaction was allowed to warm to room temperature overnight. Product formation was confirmed by LCMS, and then the reaction was diluted with saturated NH_4Cl and water and extracted with EtOAc (2×). The combined organic extracts were washed with brine, dried over anhydrous $MgSO_4$, filtered, and concentrated *in vacuo*. The resulting residue was redissolved in MeOH (10 mL), and AcOH (100 µL) was added. After stirring for 10 min, the solution was concentrated to dryness and purified by flash chromatography on silica (100% CH_2Cl_2 to CH_2Cl_2:MeOH 90:10). The resultant material was stirred in TFA for 30 min, concentrated *in vacuo* and

re-purified by column chromatography (100% CH_2Cl_2 to CH_2Cl_2:MeOH 90:10) to afford **HMSiR** as a dark blue solid (71%). ^{1}H-NMR (MeOD, 400 MHz) δ 7.90 (s, 1 H), 7.77 (d, *J* = 8.06 Hz, 1 H), 6.98 (d, *J* = 8.9 Hz, 2 H), 6.95 (d, *J* = 2.9 Hz, 2 H), 6.79 (d, *J* = 8.0 Hz, 1 H), 6.67 (dd, J = 8.9, 2.9 Hz, 2 H), 5.53 (s, 2 H), 2.89 (s, 12 H), 0.51 (d, *J* = 40.0 Hz, 6 H). ^{13}C NMR ($CDCl_3$, 125 MHz) δ 176.4, 171.8, 151.9, 151.6, 140.9, 140.1, 139.6, 136.7, 131.0, 125.1, 124.4, 118.7, 116.8, 74.9, 42.1, 1.4, 0.8. HRMS calc'd for $C_{27}H_{31}N_2O_3Si$ $[M]^+$ *m/z* 459.2104, found 459.2214.

3.4.4 Synthesis of $HMSiR_{indol}$

Supplementary Scheme S2. Synthesis of $HMSiR_{indol}$

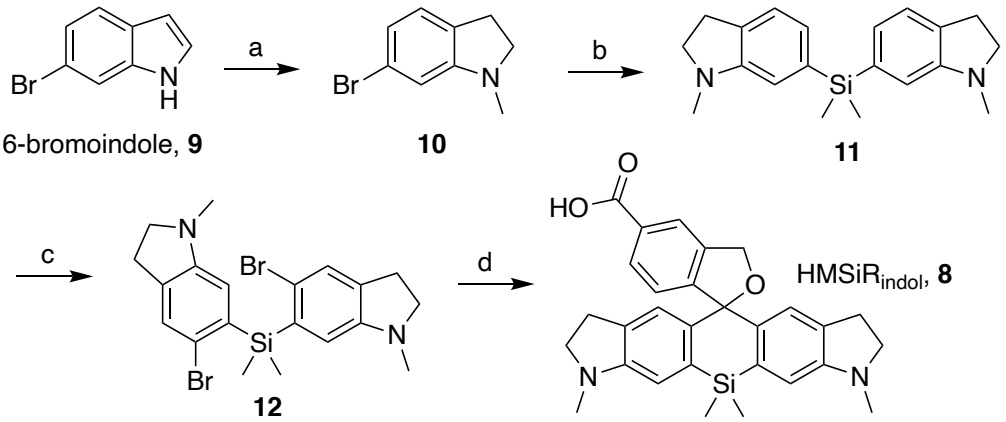

a) formadelhyde, $NaBH_3CN$, r.t., b) n-BuLi, Me_2SiCl_2, -78 ˚C to rt,
c) NBS, DMF, rt, d) i. tert-BuLi, **3**, -78 ˚C to rt, ii. TFA, rt

6-bromo-1-methylindoline 10.

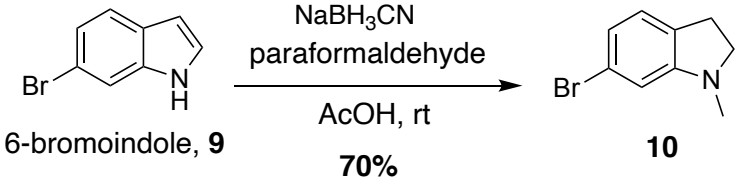

6-bromoindole, **9** — **10**

A suspension of 6-bromoindole **9** (2.0 g, 10.20 mmol), paraformaldehyde (3.1 g, 102.02 mmol), and $NaBH_3CN$ (3.2 g, 51.01 mmol) in AcOH (50 mL) was stirred for 3 h at r.t., and the reaction was quenched by adding NaOH. The whole was extracted with CH_2Cl_2, and washed with brine. The organic layer was dried over Na_2SO_4 and evaporated. Purification of the residue by flash chromatography on silica (100% hexanes to EtOAc:hexanes 15:85) provided **10** as a golden oil (70%). ^{1}H NMR ($CDCl_3$, 500 MHz) δ 6.92 (d, *J* = 7.5 Hz, 1 H), 6.79 (dd, *J* = 7.5, 1.7 Hz, 1 H), 6.60 (d, *J* = 1.1 Hz, 1 H), 3.37 (t, *J* = 8.1 Hz, 2 H), 2.92 (t, *J* = 8.1 Hz, 2 H), 2.77 Hz (s, 3 H) . ^{13}C NMR ($CDCl_3$, 125 MHz) δ 129.5, 125.3, 121.1, 120.6, 110.5, 101.2, 56.2, 35.9, 32.9, 28.2. HRMS calc'd for $C_9H_{11}BrN$ $[M+H]^+$ *m/z* 212.0075, found 212.0149.

dimethylbis(1-methylindolin-6-yl)silane 11.

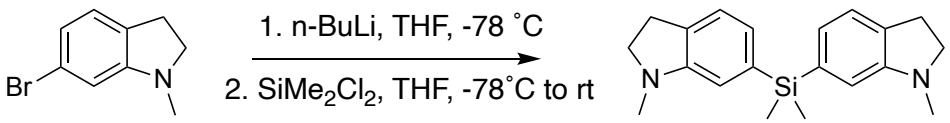

10 **99%** **11**

Bromide **10** (1.5 g, 7.07 mmol, 2.4 equiv) was dissolved in THF (13.5 mL) in a flame-dried round bottom flask and cooled to -78 °C under nitrogen. *n*-Butyllithium (2.5 M in cyclohexane, 2.83 mL, 7.07 mmol, 2.4 eq) was added, and the reaction was stirred at -78 °C for 30 min. Dichlorodimethylsilane (0.356 mL, 2.95 mmol) in THF (5 mL) was then added, the dry ice bath was removed, and the reaction was stirred at room temperature for 3 h. It was subsequently quenched with saturated NH_4Cl, diluted with water, and extracted with EtOAc (2×). The combined organic phase was washed with brine, dried over anhydrous Na_2SO4, filtered, and concentrated under vacuum. The crude product was purified by flash chromatography on silica (100% hexanes to EtOAc:hexanes 15:85) to yield **11** as a colorless oil (99%). ^{1}H-NMR ($CDCl_3$, 400 MHz) δ 7.07 (d, J = 7.1 Hz, 2 H), 6.85 (d, J = 7.3 Hz, 2 H), 6.64 (s, 2 H), 3.27 (t, 7.90 Hz, 4 H), 2.92 (t, 8.20 Hz, 4 H), 2.73 (s, 6 H), 0.49 (s, 6H). HRMS calc'd for $C_{20}H_{27}N_2Si$ $[M+H]^+$ *m/z* 323.1944, found 323.1925.

bis(5-bromo-1-methylindolin-6-yl)dimethylsilane 12.

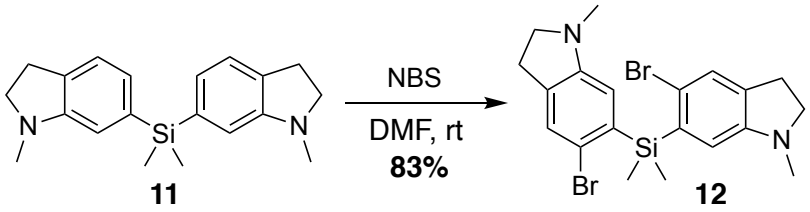

11 **12**

Silane **11** (1.05 g, 3.26 mmol) was taken up in DMF (10 mL). N-Bromosuccinimide (1.16 g, 6.52 mmol, 2 eq) was dissolved in 10 mL DMF and added dropwise over 5 min at 0 ˚C. The reaction was then stirred at room temperature overnight. Product formation was confirmed by LCMS, and then the resulting residue was concentrated in vacuo, diluted with water and extracted twice with EtOAc. The combined organic extracts were washed with water and brine, dried over anhydrous $MgSO_4$, filtered, and concentrated in vacuo. Silica gel chromatography (100% hexanes to EtOAc:hexanes 15:85) afforded **12** as a reddish brown solid (83%). ^{1}H NMR ($CDCl_3$, 400 MHz) δ 7.18 (s, 2 H), 6.54 (s, 2 H), 3.27 (t, J = 8.1 Hz, 4 H), 2.91 (t, J = 8.2 Hz, 4 H), 2.68 (s, 6 H), 0.70 (s, 6 H). HRMS calc'd for $C_{20}H_{25}Br_2N_2Si$ $[M+H]^+$ *m/z* 479.0154, found 479.0185. ^{13}C NMR ($CDCl_3$, 125 MHz) δ 137.7, 134.9, 129.5, 118.9, 116.1, 100.9, 56.8, 37.1, 29.1, 0.0. HRMS calc'd for $C_{20}H_{25}Br_2N_2Si$ $[M+H]^+$ *m/z* 479.0154, found 479.0185.

HMSiR$_{indol}$ 8.

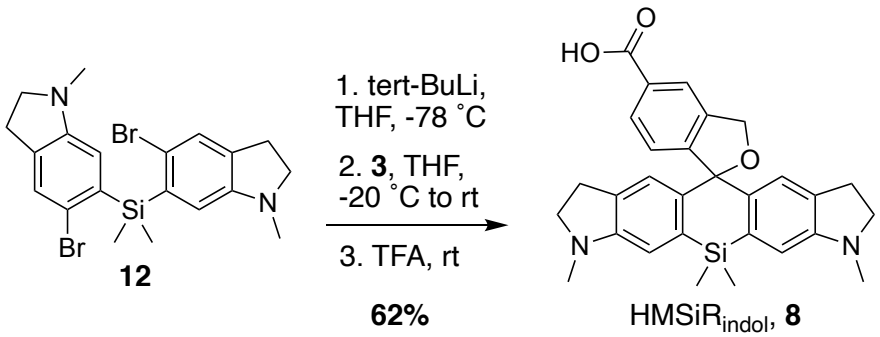

A solution of dibromide **8** (428 mg, 0.89 mmol) in THF (16 mL) was cooled to -78 °C under nitrogen. *tert*-Butyllithium (1.7 M in pentane, 2.29 mL, 3.9 mmol, 4.4 eq) was added, and the reaction was stirred at -78 °C for 30 min. A solution of **3** (435 mg, 1.78 mmol, 2.2 eq) in THF (16 mL) was added dropwise over 30 min. The reaction was allowed to warm to room temperature overnight. Product formation was confirmed by LCMS, and it was subsequently diluted with saturated NH4Cl and water and extracted with EtOAc (2×). The combined organic extracts were washed with brine, dried over anhydrous $MgSO_4$, filtered, and concentrated *in vacuo*. The resulting residue was redissolved in MeOH (10 mL), and AcOH (100 µL) was added. After stirring for 10 min, the solution was concentrated to dryness and purified by flash chromatography on silica (100% CH_2Cl_2 to CH_2Cl_2:MeOH 90:10). The resultant material was stirred in TFA for 30 min, concentrated *in vacuo* and re-purified by column chromatography (100% CH_2Cl_2 to CH_2Cl_2:MeOH 90:10) to afford **HMSiR$_{indol}$** as a bluish green solid (62%). ^{1}H-NMR (MeOD, 500 MHz) δ 8.39 (s, 1 H), 8.06 (dd, 7.6, 1.8 Hz, 1 H), 7.20 (d, *J* = 7.8 Hz, 1 H), 7.13 (s, 2 H), 6.59 (s, 2 H), 4.34 (s, 2 H), 3.80 (t, *J* = 8.1 Hz, 4H), 3.21 (s, 6 H), 2.89 (t, *J* = 8.1 Hz, 4H), 0.55 (d, *J* = 5.7 Hz, 6 H). ^{13}C NMR ($CDCl_3$, 125 MHz) δ 167.8, 162.6, 157.0, 150.2, 142.5, 140.0, 134.9, 133.3, 131.9, 131.1, 129.1, 127.9, 127.7, 114.6, 60.4, 54.2, 32.3, 25.7, -2.6, -2.9. HRMS calc'd for $C_{29}H_{31}N_2O_3Si$ $[M]^+$ *m/z* 483.2104, found 483.1947.

3.4.5 Synthesis of $HMSiR_{julol}$

Supplementary Scheme S3. Synthesis of $HMSiR_{julol}$.

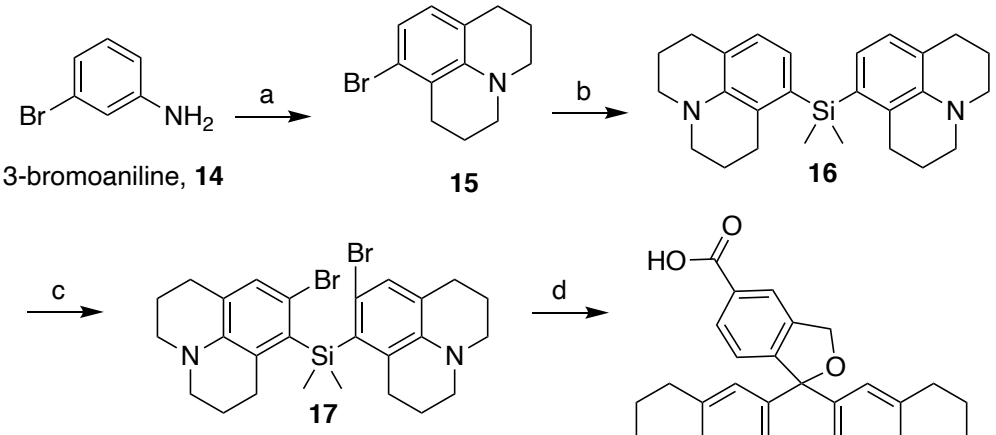

a) 1-bromo-3-chloropropane, K_2CO_3, 140 ˚C,
b) n-BuLi, Me_2SiCl_2, -78 ˚C to rt,
c) NBS, DMF, rt,
d) i. tert-BuLi, **3**, -78 ˚C to rt, ii. TFA, rt

8-bromojulolidine 15.

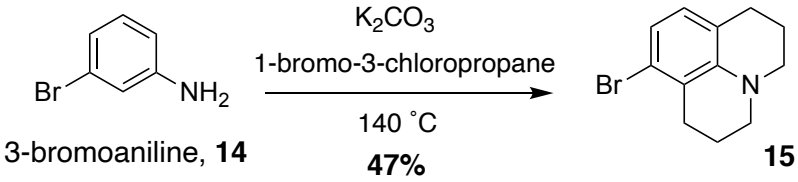

3-bromoaniline, **14** — **15**

A round-bottom flask was charged with 3-bromoaniline **14** (3.95 g, 22.96 mmol), 1-bromo-3-chloropropane (16.27 mL, 103.33 mmol, 4.5 eq.), and K_2CO_3 (6.35 g, 45.93 mmol, 2.0 eq.). After stirring at 140 °C for 48 h, the reaction was cooled to room temperature, transferred to a separatory funnel, and extracted with CH_2Cl_2 3x. The combined organic fractions were dried (Na_2SO_4), filtered, and concentrated under reduced pressure. Residual 1-bromo-3-chloropropane was removed via flash column chromatography (100% hexanes to EtOAc:hexanes 5:95). The crude mixture (containing some product, and some dialkylated intermediate) was dissolved in DMF (5.0 mL) and stirred at 160 °C for 48 hrs. After cooling to room temperature, the solution was concentrated under reduced pressure, washed with water, and extracted with CH_2Cl_2 3x.

The combined organic fractions were dried over Na_2SO_4, filtered, and concentrated under reduced pressure. The crude residue was purified via flash chromatography on silica (100% hexanes to EtOAc:hexanes 5:95 very slowly) to afford **15** as a reddish oil (47%). ^{1}H NMR (500 MHz, $CDCl_3$) δ 6.70 (d, J = 8.0 Hz, 1H), 6.57 (d, J = 8.0 Hz, 1H), 3.05 (m, 4H), 2.70 (t, J = 6.7 Hz, 2H), 2.63 (t, J = 6.5 Hz, 2H), 1.9 (m, 4H). ^{13}C NMR (125 MHz, CDCl3) δ 144.5, 127.8, 122.9, 120.7, 120.6, 119.5, 50.0, 49.7, 28.8, 27.6, 21.9, 21.8. HRMS calc'd for $C_{12}H_{15}BrN$ $[M+H]^+$ *m/z* 252.0388, found 252.0566.

dimethylbis(2,3,6,7-tetrahydro-1*H*,5*H*-pyrido[3,2,1-*ij*]quinolin-8-yl)silane 16.

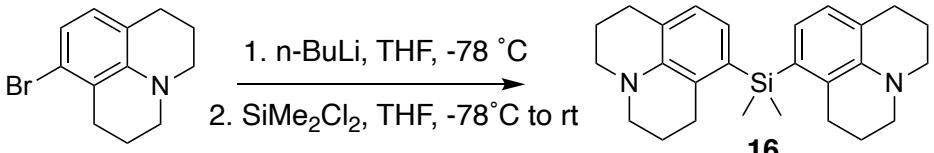

15 **16**

Bromide 15 (1.513 g, 6.0 mmol, 2.4 equiv) was dissolved in THF (12 mL) in a flame dried round bottom flask and cooled to -78 °C under nitrogen. *n*-Butyllithium (2.5 M in cyclohexane, 2.4 mL, 6.0 mmol, 2.4 eq) was added, and the reaction was stirred at -78 °C for 30 min. Dichlorodimethylsilane (0.304 mL, 2.5 mmol) in THF (1.2 mL) was then added dropwise, the dry ice bath was removed, and the reaction was slowly warmed up to room temperature for 3 h. It was subsequently quenched with saturated NH_4Cl, diluted with water, and extracted with EtOAc (2×). The combined organic phase was washed with brine, dried over anhydrous Na_2SO_4, filtered, and concentrated under vacuum. The crude product was purified by flash chromatography on silica (100% hexanes to EtOAc:hexanes 5:95) to yield 16 as a colorless oil (352 mg, 35%).^{1}H-NMR ($CDCl_3$, 400 MHz) δ 6.77 (d, *J* = 7.4 Hz, 2H), 6.69 (d, *J* = 7.4 Hz, 2H), 3.13 (t, *J* = 5.5 Hz, 4H), 3.07 (t, *J* = 5.8 Hz, 4H), 2.76 (t, *J* = 6.5 Hz, 4H), 2.67 (t, *J* = 6.4 Hz, 4H), 1.96 (dt, *J* = 12.2, 6.4 Hz, 4H), 1.85 (dt, *J* = 12.4, 6.3 Hz, 4H), 0.51 (s, 6H). ^{13}C NMR ($CDCl_3$, 125 MHz) δ142.9, 135.3, 127.7, 126.7, 123.3, 122.9, 50.7, 50.2, 28.7, 28.2, 22.5, 22.2, 0.2. HRMS calc'd for $C_{26}H_{35}N_2Si$ $[M+H]^+$ *m/z* 403.2564, found: 403.2519.

bis(9-bromo-2,3,6,7-tetrahydro-1H,5H-pyrido[3,2,1-ij]quinolin-8-yl)dimethylsilane

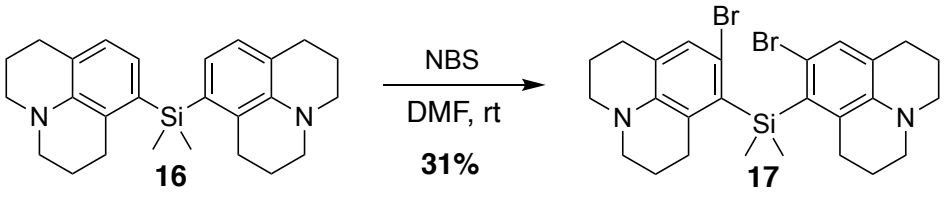

17. Silane 16 (350.2 mg, 0.87 mmol) was taken up in DMF (4 mL). N-Bromosuccinimide (309.6 mg, 1.74 mmol, 2 eq) was dissolved in 2 mL DMF and added dropwise over 5 min at 0 ˚C. The reaction was then stirred at room temperature overnight. Product formation was confirmed by LCMS, and then the resulting residue was concentrated in vacuo, diluted with water and extracted twice with EtOAc. The combined organic extracts were washed with brine(3x), dried over anhydrous Na_2SO_4, filtered and concentrated in vacuo. Silica gel chromatography (100% hexanes to EtOAc:hexanes 5:95) afforded 17 as a white solid (31%). ^{1}H NMR ($CDCl_3$, 500 MHz) δ 6.94 (s, 2H), 3.10 (t, *J* = 5.6 Hz, 4H), 3.04 (t, *J* = 6.0 Hz, 4H), 2.82 – 2.57 (m, 8H), 1.91 (dt, *J* = 12.3, 6.2 Hz, 4H), 1.81 (dt, *J* = 12.4, 6.1 Hz, 4H), 0.78 (s, 6H). ^{13}C NMR ($CDCl_3$, 125 MHz) δ 142.0, 137.7, 131.9, 129.5, 124.7, 115.5, 50.6, 49.7, 29.2, 27.8, 22.5, 21.9, 7.7. HRMS calc'd for $C_{26}H_{33}Br_2N_2Si$ $[M+H]^+$ *m/z* 559.0774, found: 559.0749.

HMSiR$_{julol}$ 13.

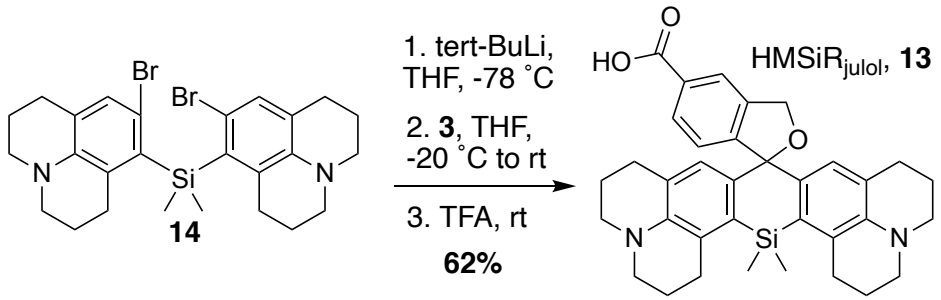

A solution of dibromide **14** (56 mg, 0.10 mmol) in THF (2 mL) was cooled to -78 °C under nitrogen. *tert*-Butyllithium (1.7 M in pentane, 0.26 mL, 0.44 mmol, 4.4 eq) was added, and the reaction was stirred at -78 °C for 30 min. A solution of **3** (51.5 mg, 0.22 mmol, 2.2 eq) in THF (2.2 mL) was added dropwise over 30 min. The reaction was allowed to warm to room temperature overnight. Product formation was confirmed by LCMS, and the reaction mixture was subsequently quenched with saturated NH_4Cl and extracted with EtOAc (2×). The combined organic extracts were washed with brine, dried over anhydrous Na_2SO_4, filtered, and concentrated *in vacuo*. The resulting residue was redissolved in MeOH (2 mL), and TFA (50 µL) was added. After stirring for 10 min, the solution was concentrated to dryness. The resultant material was subsequently stirred in TFA (1 mL) for 30 min, concentrated *in vacuo* and purified by column chromatography (100% CH_2Cl_2 to

CH_2Cl_2:MeOH 95:5) to afford $HMSiR_{julol}$ as a bluish green solid (42.1 mg, 62%). ^{1}H-NMR (MeOD with 0.1% NaOD, 500 MHz) δ 7.82 (d, *J* = 1.4 Hz, 1H), 7.63 (dd, *J* = 8.0, 1.5 Hz, 1H), 6.70 (s, 2H), 6.58 (d, *J* = 8.0 Hz, 1H), 5.51 (s, 2H), 3.16 (t, *J* = 6.0 Hz, 4H), 3.11 (td, *J* = 5.0, 2.8 Hz, 4H), 2.95 – 2.82 (m, 4H), 2.66 – 2.44 (m, 4H), 1.99 (tt, *J* = 6.7, 4.7 Hz, 4H), 1.86 (tt, *J* = 6.8, 4.7 Hz, 4H), 0.73 (s, 3H), 0.55 (s, 3H). ^{13}C NMR ($CDCl_3$, 125 MHz) δ 175.4, 163.2, 153.4, 143.0, 139.3, 138.0, 136.4, 130.4, 129.9, 127.7, 127.0, 125.3, 123.3, 123.0, 95.8, 75.0, 51.5, 51.0, 30.3, 29.4, 23.5, 23.2, 2.5, 2.1. HRMS calc'd for $C_{35}H_{39}N_2O_3Si$ $[M]^+$ *m/z* 563.2724, found: 563.2701.

3.4.6 Synthesis of $HMSiR_{THQ}$

F. Supplementary Scheme S4. Synthesis of $HMSiR_{THQ}$.

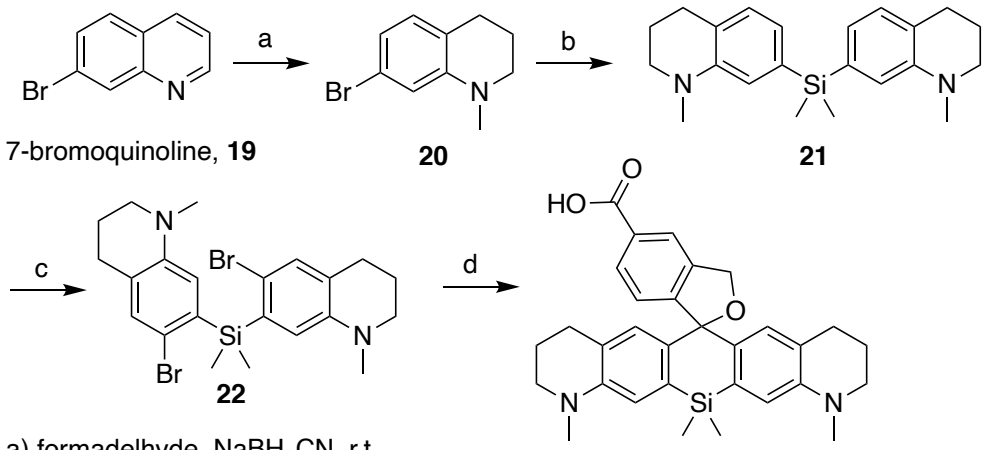

7-bromo-1-methyl-1,2,3,4-tetrahydroquinoline 20.

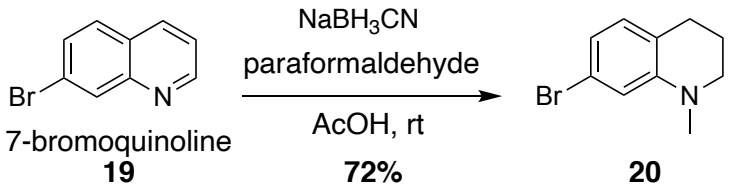

A suspension of 7-bromoquinoline **19** (5.2 g, 25.0 mmol), paraformaldehyde (7.5 g, 250.0 mmol, 10 equiv), and $NaBH_3CN$ (7.9 g, 125.0 mmol, 5.0 equiv) in AcOH (125 mL) was stirred for 3 h at RT, and the reaction was quenched by adding NaOH. The whole was extracted with CH_2Cl_2, and washed with brine. The organic layer was dried over Na_2SO_4 and evaporated. Purification of the residue by flash chromatography on silica (100% hexanes to EtOAc:hexanes 15:85) provided **20** as a golden oil (70%). ^1H NMR ($CDCl_3$, 400 MHz) δ 6.81 (d, J = 7.8 Hz, 1 H), 6.72 (m, 2 H), 3.25 (t, J = 5.7 Hz, 2 H), 2.90 Hz (s, 3 H), 2.71 (t, J = 6.4 Hz, 2 H), 1.98 (m, 2 H) . ^{13}C NMR ($CDCl_3$, 125 MHz) δ 130.6, 129.9, 121.7, 120.6, 118.8, 113.6, 50.9, 39.1, 27.3, 22.0. HRMS calc'd for $C_{10}H_{13}BrN$ $[M+H]^+$ *m/z* 226.0231, found 226.0105.

Dimethylbis(1-methyl-1,2,3,4-tetrahydroquinolin-7-yl)silane 21.

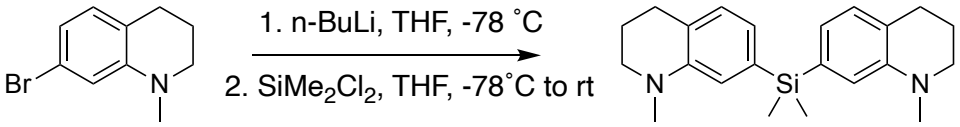

20 **98%** **21**

Aniline **20** (2.12 g, 9.40 mmol, 2.4 equiv) was dissolved in THF (18 mL) in a flame-dried round bottom flask and cooled to -78 °C under nitrogen. *n*- Butyllithium (2.5 M in cyclohexane, 3.60 mL, 9.40 mmol, 2.4 eq) was added, and the reaction was stirred at -78 °C for 30 min. Dichlorodimethylsilane (0.50 mL, 3.90 mmol) in THF (5 mL) was then added, the dry ice bath was removed, and the reaction was stirred at room temperature for 3 h. It was subsequently quenched with saturated NH_4Cl, diluted with water, and extracted with EtOAc (2×). The combined organic phase was washed with brine, dried over anhydrous Na_2SO_4, filtered, and concentrated under vacuum. The crude product was purified by flash chromatography on silica (100% hexanes to EtOAc:hexanes 15:85) to yield **21** as a colorless oil (99%). ^{1}H NMR ($CDCl_3$, 400 MHz) δ 6.92 (d, J = 7.2 Hz, 2 H), 6.78 (m, 4 H), 4.02 (t, J = 5.6, 4 H), 2.85 (s, 6 H), 2.74 (t, 6.1 Hz, 4 H), 4.10 (m, 4 H), 0.47 (s, 6 H). ^{13}C NMR ($CDCl_3$, 125 MHz) δ 148.1, 138.72, 130.4, 125.9, 124.5, 118.6, 53.5, 41.2, 29.9, 24.4, 0.00. HRMS calc'd for $C_{22}H_{31}N_2Si$ $[M+H]^+$ *m/z* 351.2257, found 351.2358.

bis(6-bromo-1-(2,2-difluoroethyl)-1,2,3,4-tetrahydroquinolin-7-yl)dimethylsilane 22.

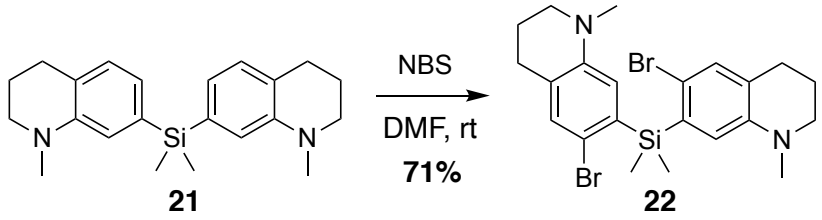

21 **22**

Silane **21** (89 mg, 0.25 mmol) was taken up in DMF (0.8 mL). N-Bromosuccinimide (90.37 mg, 0.51 mmol, 2.0 eq) was dissolved in 0.8 mL DMF and added dropwise over 5 min at 0 ˚C. The reaction was then stirred at room temperature overnight. Product formation was confirmed by LCMS, and then the resulting residue was concentrated in vacuo, diluted with water and extracted twice with EtOAc. The combined organic extracts were washed with water and brine, dried over anhydrous $MgSO_4$, filtered, and concentrated in vacuo. Silica gel chromatography (100% hexanes to EtOAc:hexanes 15:85) afforded **22** as a reddish brown solid (69%). ^{1}H-NMR ($CDCl_3$, 400 MHz) δ 7.07 (s, 2 H), 6.67 (s, 2 H), 3.16 (t, J = 5.6 Hz, 4 H), 2.77 (s, 6 H), 2.70 (t, J = 6.4 Hz, 4 H), 1.93 (p, J = 6.0 Hz, 4 H), 0.69 (s, 6 H). ^{13}C NMR ($CDCl_3$, 125 MHz) δ 145.9, 137.1, 133.3, 127.0, 120.9, 117.01, 52.0,

39.8, 28.2, 22.9, 0.00. HRMS calc'd for $C_{22}H_{29}Br_2N_2Si$ $[M+H]^+$ *m/z* 507.0467, found 507.0157.

HMSiR$_{THQ}$ 18.

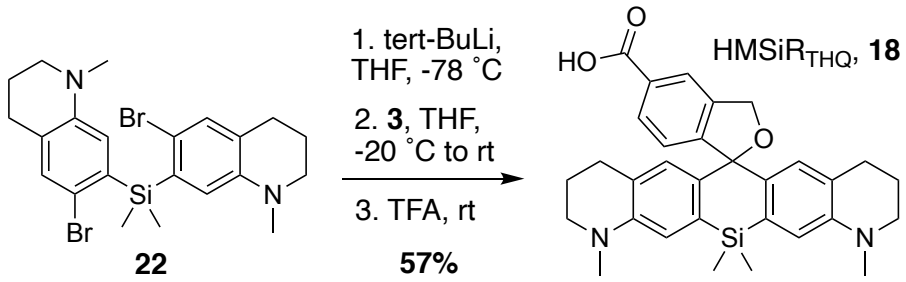

A solution of dibromide **22** (428 mg, 0.89 mmol) in THF (16 mL) was cooled to -78 °C under nitrogen. *tert*-Butyllithium (1.7 M in pentane, 2.29 mL, 3.9 mmol, 4.4 eq) was added, and the reaction was stirred at -78 °C for 30 min. A solution of **3** (435 mg, 1.78 mmol, 2.2 eq) in THF (16 mL) was added dropwise over 30 min. The reaction was allowed to warm to room temperature overnight. Product formation was confirmed by LCMS, and it was subsequently diluted with saturated NH_4Cl and water and extracted with EtOAc (2×). The combined organic extracts were washed with brine, dried over anhydrous $MgSO_4$, filtered, and concentrated *in vacuo*. The resulting residue was redissolved in MeOH (10 mL), and AcOH (100 µL) was added. After stirring for 10 min, the solution was concentrated to dryness and purified by flash chromatography on silica (100% CH_2Cl_2 to CH_2Cl_2:MeOH 90:10). The resultant material was stirred in TFA for 30 min, concentrated *in vacuo* and re-purified by column chromatography (100% CH_2Cl_2 to CH_2Cl_2:MeOH 90:10) to afford **HMSiR$_{THQ}$** as a bluish green solid (57%). ^{1}H-NMR (MeOD, 500 MHz) δ 7.97 (s, 1 H), 7.90 (s, 1 H), 7.75 (d, *J* = 8.0 Hz, 1 H), 6.76 (s, 2 H), 6.69 (s, 2 H), 5.38 (s, 2 H), 3.17 (t, *J* = 5.3 Hz), 2.90 (s, 6 H), 4.57 (m, 4 H), 1.88 (m, 4 H), 0.48 (d, *J* = 48.0 Hz, 6 H). ^{13}C NMR (151 MHz, MeOD) δ 173.94, 150.07, 145.34, 138.35, 137.06, 131.61, 128.47, 128.15, 124.70, 122.34, 121.81, 114.33, 92.83, 72.63, 69.09, 51.04, 48.16, 48.02, 47.87, 47.73, 47.59, 47.45, 47.31, 47.16, 37.96, 28.12, 27.74, 22.14, -1.18, -1.35. HRMS calc'd for $C_{31}H_{35}N_2O_3Si$ $[M]^+$ *m/z* 511.2417, found 511.2417.

3.4.7 Synthesis of Yale676$_{sb}$

Supplementary Scheme S5. Synthesis of Yale$_{676sb}$.

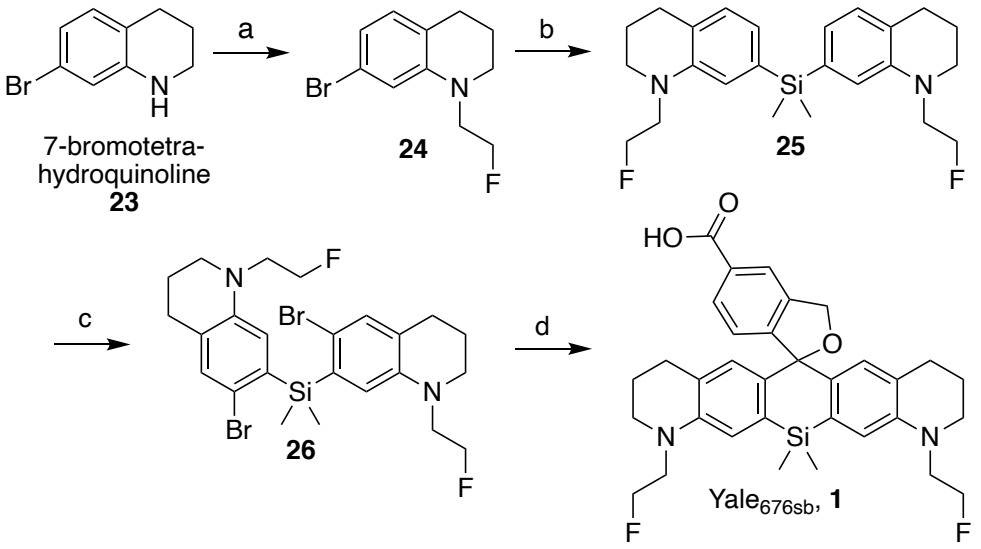

a) 1-fluoro-2-iodoethane, K_2CO_3, DMF, 70˚C, b) n-BuLi, Me_2SiCl_2, -78 ˚C to rt, c) NBS, DMF, rt, d) i. tert-BuLi, **3**, -78 ˚C to rt, ii. TFA, rt

7-bromo-1-(2-fluoroethyl)-1,2,3,4-tetrahydroquinoline 24.

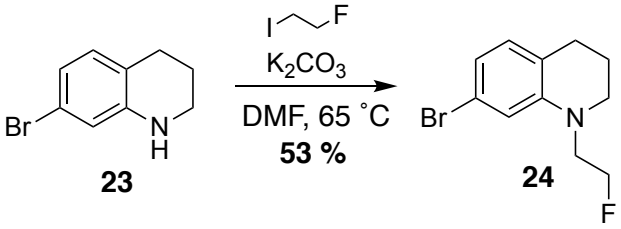

Potassium carbonate (1.33 g, 9.6 mmol, 1.5 equiv) was added to a solution of 7-bromo-1,2,3,4-tetrahydroquinoline **23** (1.36 g, 6.4 mmol, 1.0 equiv) in DMF (5.5 mL). 1-bromo-2-fluoroethane (7.7 mmol, 1.2 equiv) was added, and the reaction was stirred at 65 °C for 18 h. The mixture was allowed to cool to room temperature, diluted with water, and acidified with 1 M HCl. The aqueous phase was extracted with ethyl acetate, and the combined organic phases were washed 3x with water and brine and dried over Na_2SO_4. The solvent was evaporated under vacuum, and the crude product was purified by flash column chromatography on silica (100% hexanes to EtOAc:hexanes 5:95) to yield **24** (53%) as a yellow oil. ^{1}H-NMR ($CDCl_3$, 400 MHz) δ 6.78 (d, *J* = 7.7 Hz, 1 H), 6.68 (dd, *J* = 7.9, 1.7 Hz, 1 H), 6.61 (d, *J* = 1.8 Hz, 1 H), 4.66 (t, *J* = 5.2 Hz, 1 H), 4.54 (t, *J* = 5.2 Hz, 1 H), 3.58 (t, *J* = 5.2 H, 1 H), 3.52 (t, *J* = 5.2 H, 1 H), 3.35 (t, *J* = 5.8 Hz, 2 H), 2.68 (t, *J* = 6.4, 2 H), 1.92 (m, *J* = 5.8, 6.2 Hz, 2 H). ^{13}C NMR ($CDCl_3$, 125 MHz) δ 146.0, 130.5,

121.4, 120.6, 118.7, 112.9, 82.1, 80.7, 51.5, 51.3, 50.3, 27.7, 21.9. HRMS calc'd for $C_{10}H_{13}BrN$ $[M+H]^+$ *m/z* 226.0231, found 226.0105.

bis(1-(2-fluoroethyl)-1,2,3,4-tetrahydroquinolin-7-yl)dimethylsilane 25.

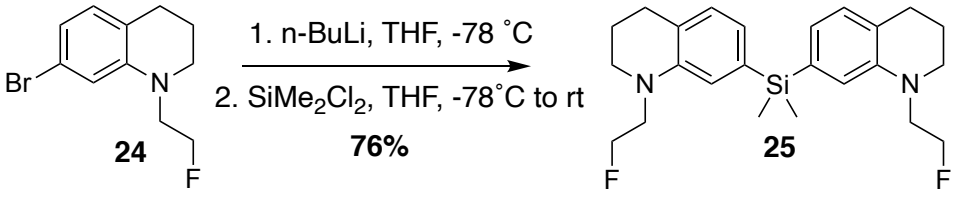

Aniline **24** (398 mg, 1.54 mmol, 2.4 equiv) was dissolved in THF (3.6 mL) in a flame-dried round bottom flask and cooled to -78 °C under nitrogen. *n*- Butyllithium (2.5 M in cyclohexane, 0.62 mL, 1.54 mmol, 2.4 eq) was added, and the reaction was stirred at -78 °C for 30 min. Dichlorodimethylsilane (0.08 mL, 0.64 mmol) in THF (0.4 mL) was then added, the dry ice bath was removed, and the reaction was stirred at room temperature for 3 h. It was subsequently quenched with saturated NH_4Cl, diluted with water, and extracted with EtOAc (2×). The combined organic phase was washed with brine, dried over anhydrous Na_2SO4, filtered, and concentrated under vacuum. The crude product was purified by flash chromatography on silica (100% hexanes to EtOAc:hexanes 15:85) to yield **25** as a bronze oil (76%). ^{1}H-NMR ($CDCl_3$, 400 MHz) δ 6.93 (d, *J* = 7.2 Hz, 2 H), 6.75 (d, *J* = 7.3 Hz, 2 H), 6.65 (s, 2 Hz), 4.60 (t, *J* = 6.0 Hz, 2 H), 4.48 (t, *J* = 6.0 Hz, 2 H), 3.57 (t, *J* = 5.2 Hz, 2 H), 3.51 (t, 5.2 Hz, 2 H), 3.35 (t, *J* = 5.2 Hz, 4 H), 2.74 (t, *J* = 6.3 Hz, 4 H), 1.93 (m, 4 H), 0.45 (s, 6 H); ^{13}C NMR ($CDCl_3$, 125 MHz) δ 146.4, 138.9, 131.1, 126.0, 124.5, 118.3, 84.4, 83.1, 53.9, 53.7, 52.9, 30.27, 24.27, 0.0. HRMS calc'd for $C_{24}H_{33}F_2N_2Si$ $[M+H]^+$ *m/z* 415.2381, found 415.2366.

bis(6-bromo-1-(2-fluoroethyl)-1,2,3,4-tetrahydroquinolin-7-yl)dimethylsilane 26.

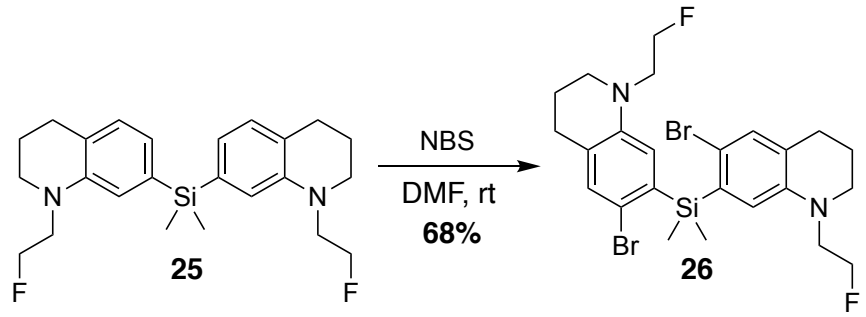

Silane **25** (35.5 mg, 0.086 mmol) was taken up in DMF (0.8 mL). N-Bromosuccinimide (30.5 mg, 0.17 mmol, 2 eq) was dissolved in 0.8 mL DMF and added dropwise over 5 min at 0 ˚C. The reaction was then stirred at room temperature overnight. Product formation was confirmed by LCMS, and then the resulting residue was concentrated in vacuo, diluted with water and extracted twice with EtOAc. The combined organic extracts were washed with water and brine, dried over anhydrous $MgSO_4$, filtered, and concentrated in vacuo. Silica gel chromatography (100% hexanes to EtOAc:hexanes 15:85) afforded **26** as a reddish brown solid (68%). ^{1}H-NMR ($CDCl_3$, 400 MHz) δ 7.09 (s, 2 H), 6.51 (s, 2 H), 4.53 (t, *J* = 5.3 Hz, 2 H), 4.41 (*J* = 5.3 Hz, 2 H), 3.47 (t, *J* = 5.2 Hz, 2 H), 3.41 (t, *J* = 5.2 Hz, 2H), 3.32 (t, *J* = 5.5 Hz, 4 H), 2.71 (t, *J* = 6.3 Hz, 4 H), 1.91 (m, 4 H), 0.69 (s, 6 H). ^{13}C NMR ($CDCl_3$, 125 MHz) δ 144.1 (C), 137.4 (CH), 133.7 (CH), 126.9 (C), 120.3 (C), 116.7 (C), 82.9 (CH_2F), 81.5 (CH_2F), 52.6 (CH_2), 52.4 (CH_2), 51.4 (CH_2), 28.4 (CH_2), 22.7 (CH_2), 0.00 (CH_3). HRMS calc'd for $C_{24}H_{31}Br_2F_2N_2Si$ $[M+H]^+$ *m/z* 571.0591, found 571.0268.

Yale$_{676sb}$ 1.

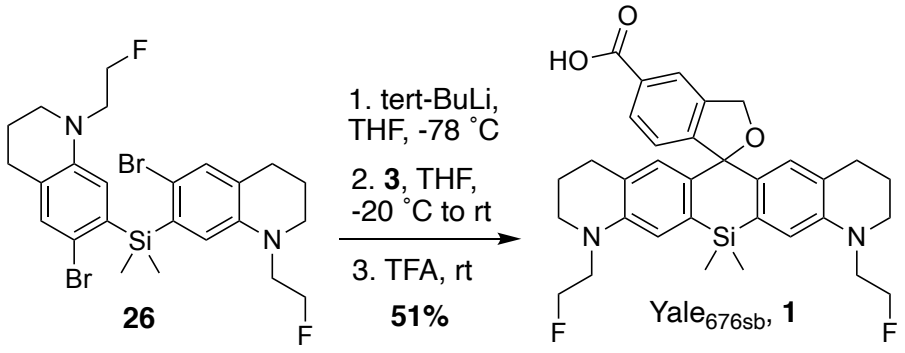

A solution of dibromide **26** (52.5 mg, 0.092 mmol) in THF (2.5 mL) was cooled to -78 °C under nitrogen. *tert*-Butyllithium (1.7 M in pentane, 0.24 mL, 0.404 mmol, 4.4 eq) was added, and the reaction was stirred at -78 °C for 30 min. A solution of **3** (47.3 mg, 0.202 mmol, 2.2 eq) in THF (2.5 mL) was added dropwise over 30 min. The reaction was allowed to warm to room temperature overnight. Product formation was confirmed by LCMS, and it was subsequently diluted with saturated NH_4Cl and water and extracted with EtOAc (2×). The combined organic extracts were washed with brine, dried over anhydrous MgSO4, filtered, and concentrated *in vacuo*. The resulting residue was redissolved in MeOH (3 mL), and AcOH (100 µL) was added. After stirring for 10 min, the solution was concentrated to dryness and purified by flash chromatography on silica (100% CH_2Cl_2 to CH_2Cl_2:MeOH 90:10). The resultant material was stirred in TFA for 30 min, concentrated *in vacuo* and re-purified by column chromatography (100% CH_2Cl_2 to CH_2Cl_2:MeOH 90:10) to afford **Yale$_{676sb}$** as a bluish green solid (51%). ^{1}H-NMR (MeOD, 500 MHz) δ 7.93 (s, 1 H), 7.79 (d, *J* = 7.9 Hz, 1 H),6.76 (d, *J* = 8.0 Hz, 1 H), 6.71 (s, 2 H), 6.65 (s, 2 H), 5.36 (s, 2 H), 4.62 (dt, *J* = 47.9, 4.5 Hz, 4), 3.61 (m, 4 H), 3.34 (m, 4 H), 2.53 (m, 4 H), 1.83 (m, 4 H), 0.43 (d, *J* = 44.8 Hz, 6 H). ^{13}C NMR ($CDCl_3$, 125 MHz) δ 174.0, 149.9, 143.6, 137.8, 137.2, 137.0, 131.7, 128.6, 128.5, 124.2, 122.5, 121.8, 114.1, 92.8, 82.1, 80.8, 72.5, 51.2, 51.1, 50.2, 28.1, 22.0, -1.2, -1.5. HRMS calc'd for $C_{33}H_{37}F_2N_2O_3Si$ $[M]^+$ *m/z* 575.2542, found 575.2616.

3.4.8 Synthesis of $HMSiR_{2\text{-}FlEt}$

H. Supplementary Scheme S6. Synthesis of $HMSiR_{2Fl\text{-}Et}$.

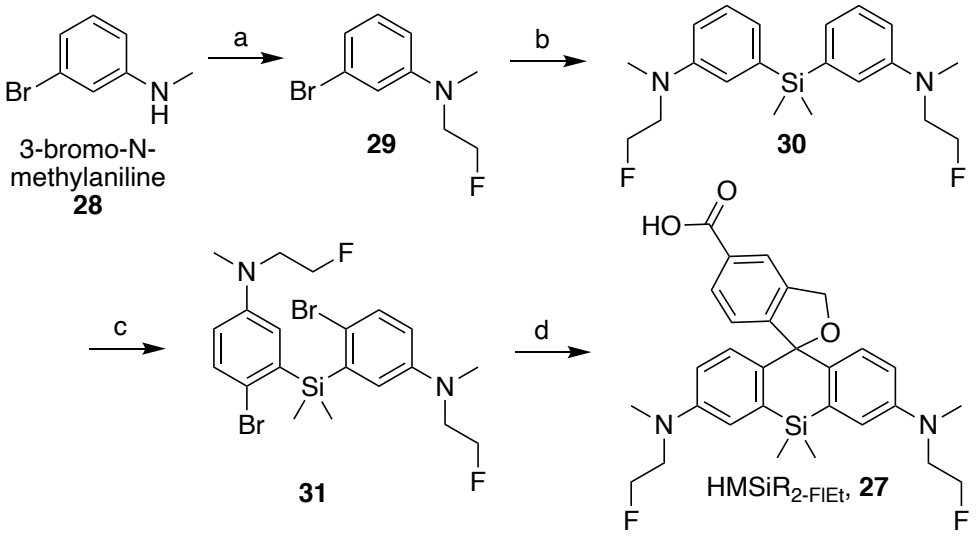

a) 1-fluoro-2-iodoethane, K_2CO_3, DMF, 70˚C, b) n-BuLi, Me_2SiCl_2, -78 ˚C to rt, c) NBS, DMF, rt, d) i. tert-BuLi, **3**, -78 ˚C to rt, ii. TFA, rt

3-bromo-*N*-(2-fluoroethyl)-*N*-methylaniline 29.

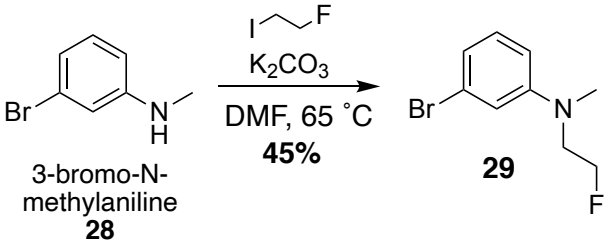

Potassium carbonate (1.1 g, 8.06 mmol, 1.5 equiv) was added to a solution of 3-bromo-N-methylaniline **28** (1.0 g, 5.38 mmol, 1.0 equiv) in DMF (4.8 mL). 1-bromo-2-fluoroethane (0.53 mL, 6.45 mmol, 1.2 equiv) was added, and the reaction was stirred at 65 °C for 18 h. The mixture was allowed to cool to room temperature, diluted with water, and acidified with 1 M HCl. The aqueous phase was extracted with ethyl acetate, and the combined organic phases were washed 3x with water and brine and dried over Na_2SO_4. The solvent was evaporated under vacuum, and the crude product was purified by flash column chromatography on silica (100% hexanes to EtOAc:hexanes 5:95) to yield **29** (53%) as a dark oil. ^{1}H-NMR ($CDCl_3$, 400 MHz) δ 7.06 (t, J = 7.8 Hz, 1 H), 6.82 (m, 2 H), 6.60 (m, 1 H), 4.63 (t, J = 5.2 Hz, 1 H), 4.51 (t, J = 5.2 Hz, 1 H), 3.64 (t, J = 5.2 H, 1 H), 2.98 (s, 3 H). ^{13}C NMR (101 MHz, $CDCl_3$) δ 150.17, 130.58, 123.68, 119.74, 115.19, 110.98, 82.58, 80.90, 77.48, 77.16, 76.84, 52.83, 52.62, 39.21.

3,3'-(dimethylsilanediyl)bis(*N*-(2-fluoroethyl)-*N*-methylaniline) 30.

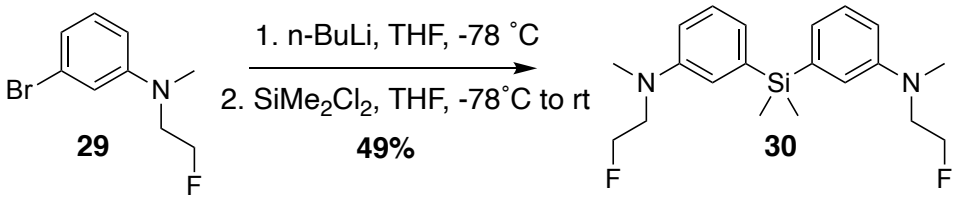

Aniline **29** (478 mg, 2.06 mmol, 2.4 equiv) was dissolved in THF (4.5 mL) in a flame-dried round bottom flask and cooled to -78 °C under nitrogen. *n*-Butyllithium (2.5 M in cyclohexane, 0.82 mL, 2.06 mmol, 2.4 eq) was added, and the reaction was stirred at -78 °C for 30 min. Dichlorodimethylsilane (0.11 mL, 0.86 mmol) in THF (0.5 mL) was then added, the dry ice bath was removed, and the reaction was stirred at room temperature for 3 h. It was subsequently quenched with saturated NH_4Cl, diluted with water, and extracted with EtOAc (2×). The combined organic phase was washed with brine, dried over anhydrous Na_2SO4, filtered, and concentrated under vacuum. The crude product was purified by flash chromatography on silica (100% hexanes to EtOAc:hexanes 15:85) to yield **30** as a golden oil (49%). ^{1}H-NMR ($CDCl_3$, 400 MHz) δ 7.24 (m, 2 H), 6.90 (m, 4 H), 6.75 (d, J = 8.6 Hz, 2 Hz), 4.64 (t, *J* = 6.0 Hz, 2 H), 4.52 (t, *J* = 6.0 Hz, 2 H), 3.67 (t, *J* = 5.2 Hz, 2 H), 3.50 (t, 5.2 Hz, 2 H), 3.0 (s, 6 H), 0.53 (s, 6 H). ^{13}C NMR (101 MHz, $CDCl_3$) δ 148.26, 139.24, 128.77, 122.91, 117.99, 113.33, 82.71, 81.02, 77.42, 77.10, 76.79, 53.00, 52.79, 39.12, -2.20.

3,3'-(dimethylsilanediyl)bis(4-bromo-*N*-(2-fluoroethyl)-*N*-methylaniline) 31.

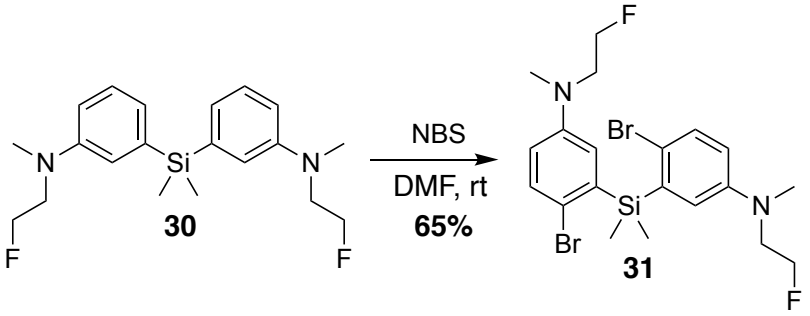

Silane **30** (105.8 mg, 0.28 mmol) was taken up in DMF (1.0 mL). N-Bromosuccinimide (103.89 mg, 0.58 mmol, 2.0 eq) was dissolved in 1.0 mL DMF and added dropwise over 5 min at 0 ˚C. The reaction was then stirred at room temperature overnight. Product formation was confirmed by LCMS, and then the resulting residue was concentrated in vacuo, diluted with water, and extracted twice with EtOAc. The combined organic extracts were washed with water and brine, dried over anhydrous MgSO4, filtered, and concentrated in vacuo. Silica gel chromatography (100% hexanes to EtOAc:hexanes 15:85) afforded **31** as a reddish brown solid (65%). ^{1}H-NMR ($CDCl_3$, 400 MHz) δ 7.40 (d,

J = 8.8 Hz, 2 H), 6.82 (d, J = 3.3 Hz, 2 H), 6.65 (dd, J = 8.9, 3.3 Hz, 2 H), 4.63 (t, *J* = 5.3 Hz, 2 H), 4.51 (*J* = 5.3 Hz, 2 H), 3.62 (t, *J* = 5.2 Hz, 2 H), 3.56 (t, *J* = 5.2 Hz, 2H), 2.99 (s, 6 H), 0.79 (s, 6 H). ^{13}C NMR (101 MHz, $CDCl_3$) δ 147.44, 139.05, 133.33, 121.60, 117.01, 115.22, 82.68, 80.99, 77.48, 77.16, 76.84, 53.15, 52.95, 39.20, -0.79.

HMSiR$_{2\text{-FlEt}}$ 27.

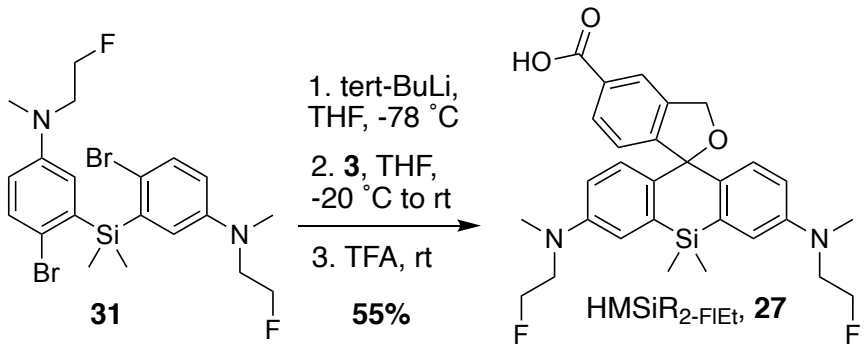

A solution of dibromide **31** (48.0 mg, 0.092 mmol) in THF (1.6 mL) was cooled to -78 °C under nitrogen. *tert*-Butyllithium (1.7 M in pentane, 0.24 mL, 0.406 mmol, 4.4 eq) was added, and the reaction was stirred at -78 °C for 30 min. A solution of **31** (47.5 mg, 0.203 mmol, 2.2 eq) in THF (1.6 mL) was added dropwise over 30 min. The reaction was allowed to warm to room temperature overnight. Product formation was confirmed by LCMS, and it was subsequently diluted with saturated NH4Cl and water and extracted with EtOAc (2×). The combined organic extracts were washed with brine, dried over anhydrous MgSO4, filtered, and concentrated *in vacuo*. The resulting residue was redissolved in MeOH (3 mL), and AcOH (100 µL) was added. After stirring for 10 min, the solution was concentrated to dryness and purified by flash chromatography on silica (100% CH_2Cl_2 to CH_2Cl_2:MeOH 90:10). The resultant material was stirred in TFA for 30 min, concentrated *in vacuo* and re-purified by column chromatography (100% CH_2Cl_2 to CH_2Cl_2:MeOH 90:10) to afford **HMSiR$_{2\text{FlEt}}$** as a bluish green solid (55%). ^{1}H-NMR (MeOD, 400 MHz) δ 7.97 (s, 1 H), 7.80 (d, *J* = 7.8 Hz, 1 H), 7.04 (d, *J* = 8.7 Hz, 2 H), 6.98 (d, *J* = 2.9 Hz, 2 H), 6.89 (d, *J* = 7.9 Hz, 1 H), 6.64 (dd, J = 9.0, 2.9 Hz, 2 H), 5.41 (s, 2 H), 4.60 (t, J = 5.1 Hz, 2 H), 4.49 (t, J = 5.1 Hz, 2 H), 3.66 (t, J = 5.1 Hz, 2 H), 3.61 (t, J = 5.1 Hz, 2 H) 2.95 (s, 6 H), 0.55 (s, 3 H), 0.42 (s, 3 H). HRMS calc'd for $C_{29}H_{33}F_2N_2O_3Si$ $[M]^+$ *m/z* 523.2229, found 523.2320.

3.4.9 Synthesis of Cal664sb

Supplementary Scheme S7. Synthesis of Cal_{664sb}.

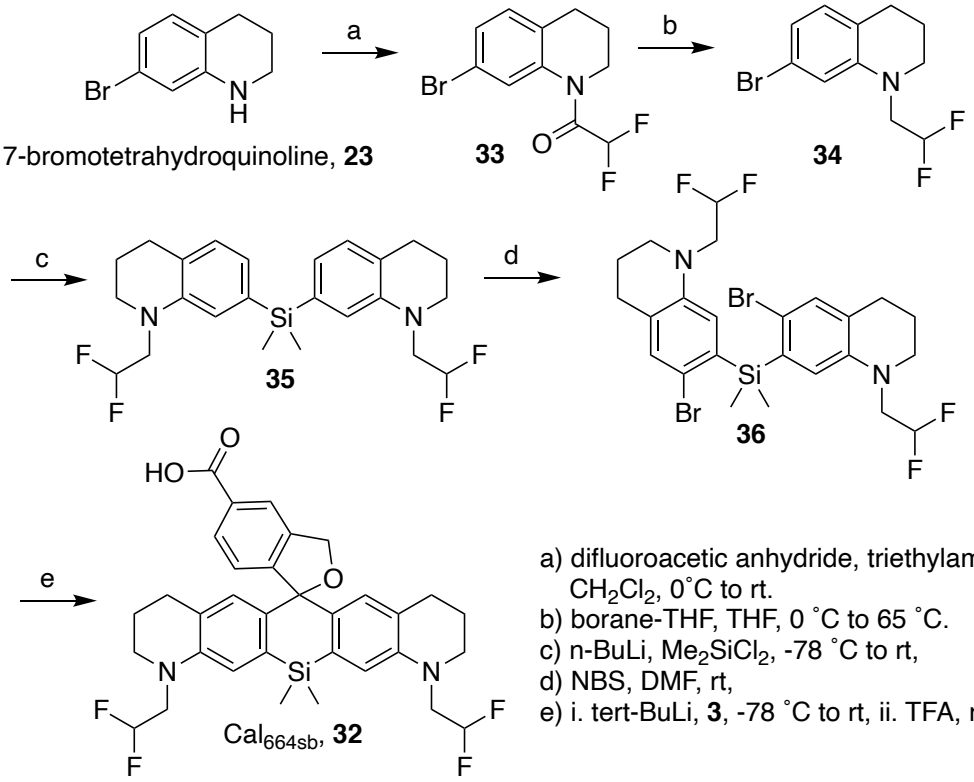

a) difluoroacetic anhydride, triethylamine, CH_2Cl_2, 0˚C to rt.
b) borane-THF, THF, 0 ˚C to 65 ˚C.
c) n-BuLi, Me_2SiCl_2, -78 ˚C to rt,
d) NBS, DMF, rt,
e) i. tert-BuLi, **3**, -78 ˚C to rt, ii. TFA, rt

1-(7-bromo-3,4-dihydroquinolin-1(2*H*)-yl)-2,2-difluoroethan-1-one 33.

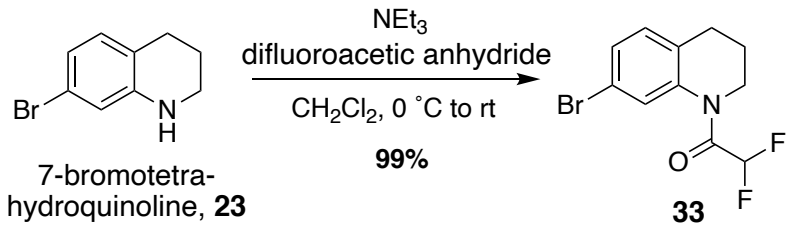

7-bromotetrahydroquinoline **23** (318.1 mg, 1.5 mmol) was dissolved in CH_2Cl_2 (10 mL) and Et_3N (0.44 mL, 3.15 mmol, 2.1 eq) was added. An aliquot of $(CF_2CO)_2O$ (0.23 mL, 1.8 mmol, 1.2 eq) was added dropwise at 0 °C, and the mixture was stirred for 24 h at room temperature. The reaction mixture was washed with saturated $NaHCO_3$(aq). The organic layer was separated, and the aqueous layer was back-extracted twice with CH_2Cl_2. The combined organic extracts were dried over Na_2SO_4 and evaporated to yield **33** as a light yellow solid (430 mg, 99%). The product was used in the following synthetic step without further purification.

7-bromo-1-(2,2-difluoroethyl)-1,2,3,4-tetrahydroquinoline 34.

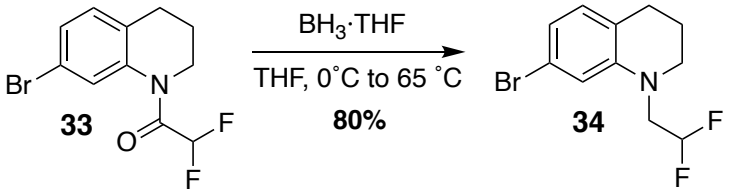

To a solution of **33** (290.1 mg, 1.0 mmol) in dry THF (1 mL) at 0°C was added an aliquot of 1M solution BH_3 in THF (2 mL, 2.0 eq). The mixture was then heated at reflux for 16 hr. The reaction mixture was cooled to 0°C and the excess BH_3 carefully quenched upon addition of MeOH (1 mL) followed by 1 M aq. NaOH (1 mL). After stirring at room temperature for 20 min, the mixture was diluted with ether (10 mL), and the organic layer was separated. The aqueous layer was extracted with ether (3×10 mL); combined organic solutions were washed with sat. aq. $NaHCO_3$, brine, dried and the solvent was evaporated in vacuo. The desired product was purified by flash column chromatography (220.0 mg, 80%)

bis(1-(2,2-difluoroethyl)-1,2,3,4-tetrahydroquinolin-7-yl)dimethylsilane 35.

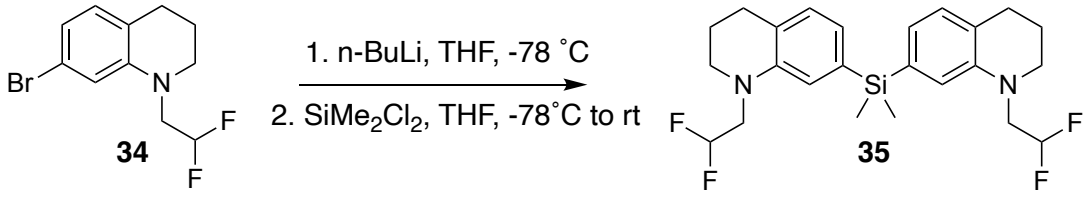

7-bromo-1-(2,2-difluoroethyl)-1,2,3,4-tetrahydroquinoline **34** (198.8 mg, 0.72 mmol, 2.4 eq) was dissolved in 1.5 mL THF in a flame-dried round-bottom flask and cooled to -78 °C under nitrogen. *n*-Butyllithium (0.29 mL, 2.5 M in cyclohexane, 2.4 eq) was added, and the reaction was stirred at -78 °C for 30 min. Dichlorodimethylsilane (36.5 uL, 0.3 mmol, dissolved in 0.2 mL THF) was then added, the dry ice bath was removed, and the reaction was stirred at room temperature for 3 h. It was subsequently quenched with saturated NH_4Cl, diluted with water, and extracted with EtOAc (2×10 mL). The combined organic phase was washed with brine, dried over anhydrous Na_2SO4, filtered, and concentrated under vacuum. The crude product was purified by flash chromatography on silica (100% hexanes to EtOAc:hexanes 15:85) to yield **35** as a colorless oil (83.9 mg, 62%).

bis(6-bromo-1-(2,2-difluoroethyl)-1,2,3,4-tetrahydroquinolin-7-yl)dimethylsilane 36.

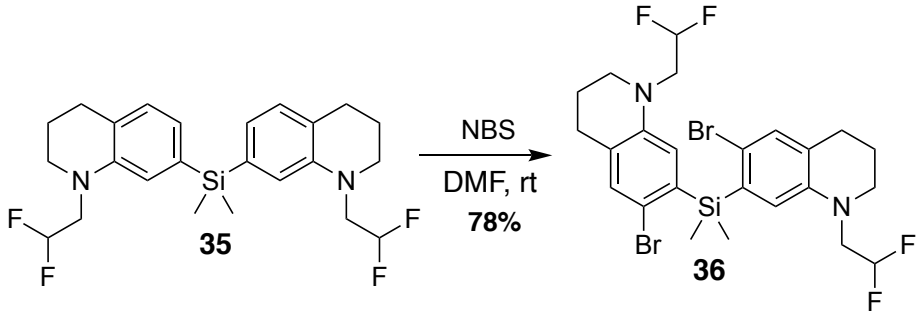

Silane **35** (120.1 mg, 0.267 mmol) was taken up in 2 mL DMF. N-Bromosuccinimide (94.9 mg, 0.533 mmol, 2.0 eq) was dissolved in 1 mL DMF and added dropwise over 5 min at 0 ˚C. The reaction was then stirred at room temperature overnight. Product formation was confirmed by LCMS, and then the resulting residue was concentrated in vacuo, diluted with water and extracted twice with EtOAc (20 mL). The combined organic extracts were washed with water and brine, dried over anhydrous $MgSO_4$, filtered, and concentrated in vacuo. Silica gel chromatography (100% hexanes to EtOAc:hexanes 15:85) afforded **26** as a white solid (126.7 mg, 78%)

Cal$_{664sb}$, 32.

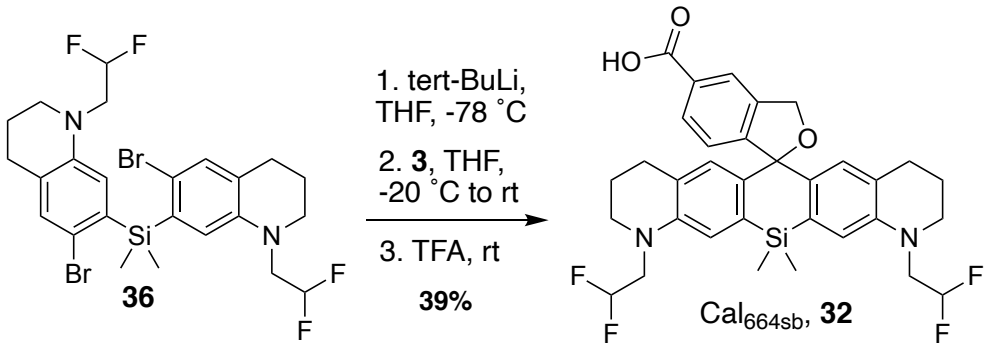

A solution of dibromide **36** (41.5 mg, 0.068 mmol) in THF was cooled to -78 °C under nitrogen. *tert*-Butyllithium (0.18 mL, 0.30 mmol, 1.7 M in pentane, 4.4 eq) was added, and the reaction was stirred at -78 °C for 30 min. A solution of **3** (35.2 mg, 0.15 mmol, 2.2 eq) in 1.5 mL THF was added dropwise over 30 min. The reaction was allowed to warm to room temperature overnight. Product formation was confirmed by LCMS. The reaction was subsequently diluted with saturated NH_4Cl and water and extracted twice with EtOAc. The combined organic extracts were washed with brine, dried over anhydrous $MgSO_4$, filtered, and concentrated *in vacuo*. The resulting residue was redissolved in MeOH (3 mL), and AcOH (100 µL) was added. After stirring for 10 min, the solution was concentrated to dryness and purified by flash chromatography on silica (100% CH_2Cl_2 to CH_2Cl_2:MeOH 90:10). The resultant material was stirred in TFA for 30 min, concentrated *in vacuo* and re-purified by column chromatography (100% CH_2Cl_2 to CH_2Cl_2:MeOH 90:10) to afford **Cal$_{664sb}$** as a bright blue solid (16.2 mg, 39% over two steps).

3.4.10 Synthesis of Yale676sb-CA

J. Supplementary Scheme S8. Synthesis of Yale$_{676sb}$-CA.

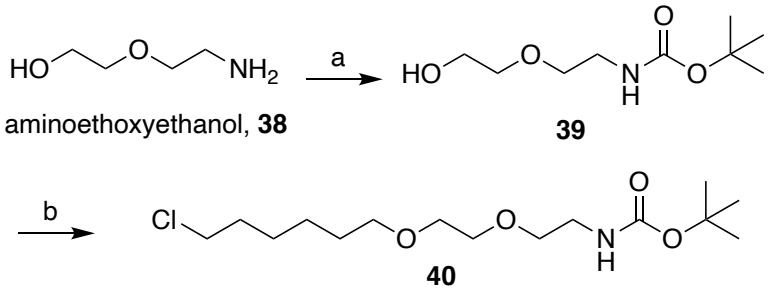

***tert*-butyl (2-(2-hydroxyethoxy)ethyl)carbamate 39.**

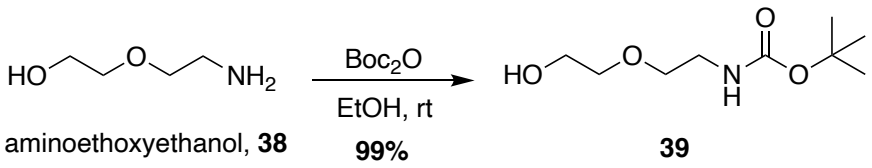

aminoethoxyethanol, **38** **99%** **39**

To a solution of 2-(2-aminoethoxy)ethanol (2.0 g, 19.02 mmol) in anhydrous EtOH (40 mL) was added Boc_2O (4.36 g, 19.02 mmol) at 0 °C. After stirring at room temperature 2 h, the reaction mixture was evaporated. The product was then extracted thrice with CH_2Cl_2. The combined organic layers were dried over Na_2SO_4 and evaporated under vacuum to obtain the product as colorless oil (99%), which was used for the next step without further purification. ^{1H}NMR: (400 MHz, $CDCl_3$, δ): 5.28 (br, 1H), 3.68-3.52 (m, 2H), 3.52-3.48 (m, 4H), 3.28-3.26 (m, 2H), 1.39 (s, 9H). ^{13}CNMR: (100MHz, CDCl3, δ): 156.32, 79.41, 72.37, 70.37, 61.62, 40.42, 28.48. HRMS (ESI, m/z): [M+Na] calcd for $C_9H_{19}NNaO_4$, 228.1212; found 228.1207.

***tert*-butyl (2-(2-((6-chlorohexyl)oxy)ethoxy)ethyl)carbamate.**

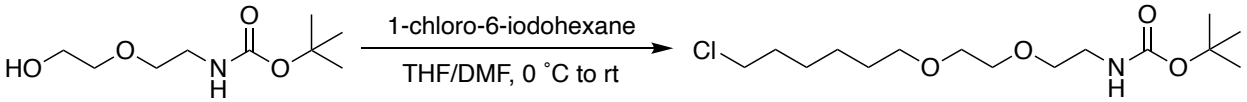

39 **69%** **40**

To a solution of **39** (1.0 g, 4.88 mmol) in THF (7 mL) and DMF (3.5 mL) at 0 °C was added NaH (233.78 mg, 60% in mineral oil, 5.85 mmol). After stirring at 0 °C for 30 min, 6-chloro-1-iodohexane (1.0 mL, 6.82 mmol) was added to the above solution. The reaction mixture was stirred overnight and quenched with saturated NH4Cl. The mixture was extracted with EtOAc (3x), washed with H_2O and brine. The combined organic layers were dried over Na_2SO_4 and concentrated. The crude product was purified by silica gel column chromatography (100% hexanes to 35:65 EtOAc:Hexanes) to yield pure **40** (69%) as colorless oil. 1H NMR: (400MHz, CDCl3, δ): 5.03 (br, 1H), 3.59-3.57 (m, 2H), 3.55-3.49 (m, 6H), 3.43 (t, J = 6.6 Hz,, 2H), 3.31-3.27 (m, 2H), 1.79-1.72 (m, 2H), 1.62-1.55 (m, 2H), 1.47-1.33 (m, 13H); 13CNMR: (100MHz, CDCl3, δ): 156.13, 79.28, 71.39, 70.36, 70.32, 70.14, 45.16, 40.45, 32.65, + 29.54, 28.54, 26.80, 25.53; HRMS (ESI, m/z): [M+Na] calcd for C15H30ClNNaO4, 346.1761; found 346.1752.

Yale$_{676sb}$-CA, 37.

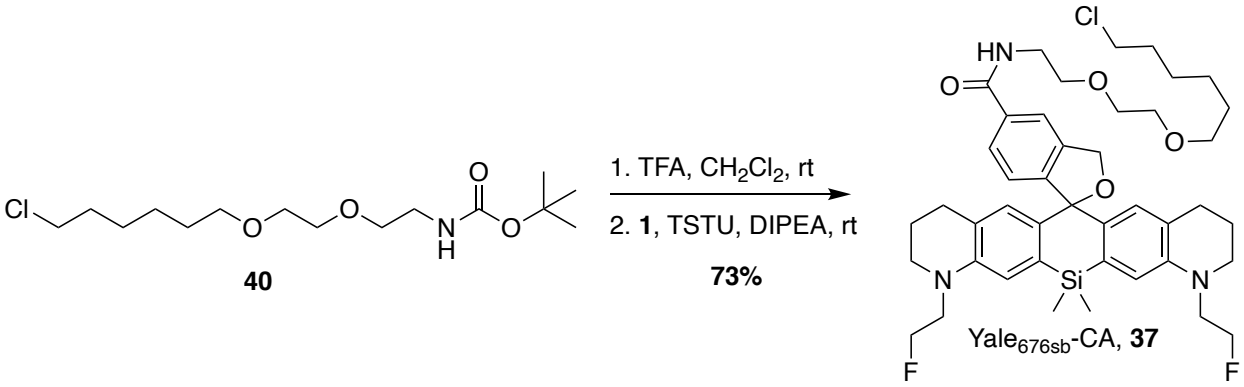

To a solution of **40** in CH_2Cl_2 was added TFA. The solution was stirred at room temperature for 1 hr and the progress of the reaction was monitored by TLC. After completion of the reaction, the reaction mixture was concentrated *in vacuo*. To the crude residue was added a pre-mixed solution (for 15 min) of **1**, TSTU and DIPEA. Additional DIPEA was added and then the reaction was stirred at room temperature for 3 h. Following completion of the reaction, as monitored by LCMS, the product was purified *via* reverse-phase HPLC to yield Yale$_{676sb}$-CA as a blue solid. ^{1}H-NMR ($CDCl_3$, 400 MHz) δ 6.78 (d, J = 7.7 Hz, 1 H), 6.68 (dd, J = 7.9, 1.7 Hz, 1 H), 6.61 (d, J = 1.8 Hz, 1 H), 4.66 (t, J = 5.2 Hz, 1 H), 4.54 (t, J = 5.2 Hz, 1 H), 3.58 (t, J = 5.2 H, 1 H), 3.52 (t, J = 5.2 H, 1 H), 3.35 (t, J = 5.8 Hz, 2 H), 2.68 (t, J = 6.4, 2 H), 1.92 (m, J = 5.8, 6.2 Hz, 2 H). ^{13}C NMR ($CDCl_3$, 125 MHz) δ 146.0, 130.5, 121.4, 120.6, 118.7, 112.9, 82.1, 80.7, 51.5, 51.3, 50.3, 27.7, 21.9. HRMS calc'd for $C_{10}H_{13}BrN$ $[M+H]^+$ *m/z* 226.0231, found 226.0105.

3.4.11 Biophysical experiments

3.4.11.1 Absorption and fluorescence spectra. Solutions used for absorption and emission spectra were obtained by diluting a 5 mM stock solution of each fluorophore with 0.2 M aqueous sodium phosphate buffer to a final concentration of 0.5 μM. Absorption spectra were measured at room temperature using a Beckman Coulter DU 730 UV/Vis spectrophotometer and 1 cm pathlength, 0.1 mL microcuvettes. Fluorescence spectra were measured at room temperature using a TCSPC TD-Fluor Horiba Fluorolog 3 Time Domain Fluorimeter using 1 cm pathlength, 3.5 mL cuvettes. All absorption and fluorescence spectra were acquired at a pH that maximized the concentration of the open/emissive form of each fluorophore (pH = 2.0 for HMSiR$_{indol}$, HMSiR$_{julol}$, HMSiR$_{THQ}$ and Yale$_{676sb}$; pH = 2.5 for HMSiR$_{2\text{-}FlEt}$; pH = 4.5 for HMSiR).

3.4.11.2 Plot of Quantum Yield *vs.* Absorption Maxima for Rhodamine-derived Fluorophores

3.4.11.3 Table of Quantum Yield and Absorption Maxima for Rhodamine-derived Fluorophores

Supplementary Table 3.1.

Name:	Type	λ_{abs} (nm)	λ_{em} (nm)	Quantum Yield [solvent]	Extinction Coefficient(M^{-1} cm^{-1})	Reference
2-Me TokyoGreen	fluorescein	491	510	0.85 (0.1 M NaOH)	N/R	1
Fluorescein	fluorescein	492	511	0.85 (N/R)	90 000	2
500R	rhodamine	501	523	0.93 (PBS)	88 000	3
HMRG	rhodamine	500	523	0.9 (0.2 M sodium phosphate)	74 000	4
HMbisTFER	rhodamine	502	526	0.85 (0.2 M sodium phosphate)	81 000	4
JF503	rhodol	503	529	0.87 (N/R)	95 000	5
HEtetTFER	rhodamine	507	530	0.76 (0.2 M sodium phosphate)	80 000	4
HMtetTFER	rhodamine	507	532	0.89 (0.2 M sodium phosphate)	57 000	4

520R	rhodamine	521	543	0.79 (PBS)	52 000	3
515R	rhodamine	515	543	0.86 (PBS)	56 000	3
JF519	rhodol	519	546	0.85 (N/R)	69 000	5
JF525	rhodamine	525	549	0.91 (N/R)	122 000	5
530RH	rhodamine	532	553	0.89 (PBS)	56 000	6
Molecule #11	rhodamine	533	557	0.89 (N/R)	133 000	5
Molecule #10	rhodamine	536	560	0.87 (N/R)	141 000	5
Molecule #9	rhodamine	541	564	0.88 (N/R)	137 000	5
Molecule #8	rhodamine	542	565	0.57 (10 mM sodium citrate)	127 000	5
Molecule #7	rhodamine	545	568	0.87 (N/R)	130 000	5
JF549	rhodamine	549	571	0.88 (N/R)	134 000	5
Molecule #6	rhodamine	549	572	0.87 (N/R)	138 000	5
Molecule #5	rhodamine	550	572	0.83 (N/R)	143 000	5
TMR	rhodamine	550	574	0.7 (N/R)	85 000	7
560CP	C-rhodamine	561	588	0.76 (PBS)	61000	6
575RH	rhodamine	574	597	0.74 (PBS)	55 000	6
570CPH	C-rhodamine	571	600	0.71 (PBS)	79 000	6
580CP	C-rhodamine	582	607	0.69 (PBS)	90 000	3
580R	rhodamine	581	607	0.95 (PBS)	58 000	3
JF585	C-rhodamine	585	609	0.78 (N/R)	156 000	5
Maryland Red	Si-fluorescein	597	613	0.67 (0.1 M NaOH)	65 000	8

Molecule #26	Si-fluorescein	598	614	0.5 (0.1 M NaOH)	84 100	8
Molecule #24	Si-fluorescein	596	618	0.42 (0.1 M NaOH)	60 900	8
SnP	pyronine	614	628	0.43 (PBS)	N/R	9
JF608	C-rhodamine	608	631	0.67 (N/R)	121 000	5
610CP	C-rhodamine	609	634	0.59 (PBS)	100 000	10
GeP	pyronine	621	634	0.4	N/R	9
Molecule #27	Si-fluorescein	617	635	0.32 (0.1 M NaOH)	67 900	8
620SiR	Si-rhodamine	617	638	0.49 (PBS)	80 000	10
620CP	C-rhodamine	617	647	0.17 (PBS)	73 000	10
Molecule #50	pyronine	636	649	0.62 (10 mM HEPES)	97 100	8
GeR	Ge-rhodamine	635	649	0.34 (PBS)	N/R	9
630GeRH	Ge-rhodamine	631	651	0.6	61 000	6
JF635	Si-rhodamine	635	652	0.56 (N/R)	167 000	5
GeR	X-rhodamine	634	655	0.43 (PBS)	97 000	6
Molecule #51	pyronine	641	657	0.26 (10 mM HEPES)	120 000	8
TMDHS	pyronine	641	659	0.39 (DCM)	102 623	11
630CP	C-rhodamine	628	660	0.06 (PBS)	6700	3
SiR-Me	Si-rhodamine	646	660	0.31 (PBS)	N/R	9
Molecule #44	rosamine	648	662	0.2 (10 mM HEPES)	116 000	8
Molecule #48	Si-rhodamine	651	666	0.48 (10 mM HEPES)	136 000	8

640SiRH	Si-rhodamine	641	662	0.42 (PBS)	51 000	6
Molecule #45	Si-rhodamine	649	663	0.47 (10 mM HEPES)	118 000	8
JF646	Si-rhodamine	646	664	0.54 (N/R)	152 000	5
Molecule #41	Si-rhodamine	650	667	0.4 (10 mM HEPES)	149 000	8
carboxy-SiR	Si-rhodamine	645	667	0.4 (N/R)	100 000	7
Molecule #43	Si-rhodamine	652	668	0.25 (10 mM HEPES)	126 000	8
Molecule #42	Si-rhodamine	654	670	0.51 (10 mM HEPES)	139 000	8
HMSiR	Si-rhodamine	650	671	0.31 (0.2 M sodium phosphate)	110 000	4
650SiR	Si-rhodamine	650	672	0.36 (PBS)	42 000	3
JF669	Si-rhodamine	669	682	0.37 (10 mM HEPES)	116 000	8
Molecule #37	Si-rhodamine	667	682	0.31 (10 mM HEPES)	139 000	8
Molecule #39	Si-rhodamine	674	685	0.14 (10 mM HEPES)	84 5000	8
NR666	X-rhodamine	666	685	0.38 (10 mM PBS)	165 000	12
SiR680	Si-rhodamine	674	689	0.35 (PBS)	130 000	13
670SiR	Si-rhodamine	670	696	0.03 (PBS)	150	3
680SiR	Si-rhodamine	679	697	0.42 (PBS)	86 000	10
Molecule #38	Si-rhodamine	683	698	0.1 (10 mM HEPES)	215 000	8

SiR700-Me	Si-rhodamine	691	712	0.12 (PBS)	100 000	13
NR698	X-rhodamine	698	712	0.32 (10 mM PBS)	25 900	12
carboxy-SiR700	Si-rhodamine	687	716	0.13 (N/R)	100 000	7
NR700	X-rhodamine	700	722	0.11 (10 mM PBS)	71 000	12
SiR720	Si-rhodamine	721	740	0.05 (PBS)	160 000	13
NR744	X-rhodamine	744	764	0.16 (10 mM PBS)	80 000	12

3.4.11.4 Determination of pK_{cycl}. The pK_{cycl} of each fluorophore was determined from a plot of the absorbance of the open/emissive form as a function of pH. Samples of each fluorophore at 2 μM in 0.2 M sodium phosphate were prepared at half-integral pH values between 2 and 12 and in triplicate using a 96-well plate. The absorbance of each solution at each pH at the wavelength corresponding to the emission λ_{max} was measured at room temperature. The data was plotted using GraphPad Prism 8.0. The normalized curves for fluorophores with a single titratable group in this pH range (Yale$_{676sb}$, HMSiR$_{indol}$, HMSiR$_{julol}$, and Cal$_{664sb}$) were fit using the following equation:

$$abs = (c_0 + c_1 * 10^{pH - pKcycl})/(1 + 10^{pH - pKcycl})$$

The normalized curves for fluorophores with two titratable groups in this pH range (HMSiR and HMSiR$_{2\text{-FlEt}}$) were fit using the following equation:

$$abs = (c_0 + c_1 * 10^{pH - pKcycl1} + c_2 * 10^{2*pH - pKcycl1 - pKcycl2})/(1 + 10^{pH - pKcycl})$$

All curves were fit such that the value of pK_{cycl}, pK_{cycl1} and pK_{cyl2} were set to the value of pH at which the normalized absorbance = 0.5. For fluorophores with both pK_{cycl1} and pK_{cycl2} (HMSiR and HMSiR$_{2\text{-FlEt}}$), pK_{cycl2} was arbitrarily set as greater than pK_{cycl1}, and pK_{cycl2} was reported.

3.4.11.5 Determination of Quantum Yield. Absolute fluorescence quantum yield values were measured under identical conditions using a Quantaurus-QY Plus spectrometer (model C13534, Hamamatsu). This instrument uses an integrating sphere to determine photons absorbed and emitted by a sample. Measurements were carried out using 5 μM samples in PBS +0.01% DMSO buffered at pH = 4.5 (HMSiR) or pH = 2.5 (HMSiR$_{indol}$,

$HMSiR_{julol}$, $HMSiR_{THQ}$, $Yale_{676sb}$, $HMSiR_{2\text{-}FlEt}$, and Cal_{664sb}). Reported values are averages (n = 3).

3.4.11.6 Meausrement of Extinction Coefficient. Extinction coefficients were determined using Beer-Lambert's law from plots of absorbance as a function of fluorophore concentration in PBS, at a pH for which the 'ON' form was determined to be maximal.

Supplementary Table 3.2.

Molecule	**pH**	**Extinction Coefficien (M^{-1} cm^{-1})**
HMSiR	4.5	110 000
$HMSiR_{indol}$	2.0	110 000
$HMSiR_{julol}$	2.0	97 000
$HMSiR_{THQ}$	2.0	104 000
$Yale_{676sb}$	2.0	88 000
$HMSiR_{2\text{-}FlEt}$	2.5	81 000
Cal_{664sb}	2.0	74 00

4.4.11.7 Single-molecule kinetics measurements. Kinetic data were acquired using dye molecules immobilized on glass and imaged with a variety of laser powers at an acquisition rate of 400 Hz. During analysis, consecutive frames over which a molecule was detected were grouped into 'emissions'. On-times were determined from the duration of emissions. Off-times correspond to the number of frames between two consecutive emissions of the same molecule. Numbers of switching cycles were determined by the number of emissions throughout the acquisition, over which all molecules were bleached.

3.4.12 Microscopy

4.4.12.1 Cross-talk measurements. Cross-talk was determined using single-color control samples labeled, imaged, and analyzed as in the two-color imaging. Under these conditions, $Yale_{676sb}$ exhibited 6.4% crosstalk at a 13% rejection rate while HMSiR had 5.6% crosstalk at a 20% rejection rate (n = 3 for $Yale_{676sb}$, n = 5 for HMSiR, with at least 1 million localizations per acquisition).

4.4.12.2 Labeling Halo-and-SNAP-fusion proteins. U-2 OS HTB-96 cells (ATCC) were electroporated with Halo-Sec61β (and SNAP-OMP25) for two-color samples) then seeded into a mattek dish (MatTek Corporation, P35G-1.5-20-C).[14] After incubating overnight, the cells were live labeled with 300nM Yale676sb-CA (and 300nM HMSiR-BG for two-color samples) diluted in McCoy's 5A (ThermoFisher Scientific, 12330031) with

1% casein for 1 hour. Cells were rinsed three times and then the media was changed once more after 30 minutes. The cells were imaged in Live Cell Imaging Solution (ThermoFisher Scientific, A14291DJ) that was supplemented with 15mM glucose. Prior to seeding, Mattek dishes were sonicated for 15 minutes in 1M KOH, rinsed three times with Milli-Q water, sterilized with 100% ethanol, and then air dried in a biological safety cabinet.

3.4.12.3 Super-resolution microscopy and image analysis. 2D super-resolution images were recorded using a custom-built ratiometric setup running custom LabVIEW software. A 642 nm laser (2W; MPB Communications) was used to excite Yale676 and HMSiR. Laser power was controlled using an acousto-optic tunable filter (AOTFnC-400.650-TN; AA Opto Electronic). Fluorescence was collected using an oil immersion objective lens (63x, 1.47 NA; Leica), passed through a quad-band filter (ZET405/488/561/647m; Chroma) and a bandpass filter (FF01-709/167; Semrock) before being imaged on a sCMOS camera (Orca Flash 4.0; HamamatsuPhotonics). For two-color imaging, channels were split by a bandpass filter (FF01-694/SP; Semrock) and the transmitted channel additionally passed through another bandpass filter (FF01-670/30; Semrock). A pair of relay lenses was used to achieve an effective pixel size of 99 nm. Images were acquired at 400 frames per second under even wide-field illumination of 10 kW/cm^2 with a 40 µm square field of view. A custom-built focus lock system was used to prevent axial drift of the sample during data acquisition. A 850 *nm* fiber-coupled diode laser (L850P010; Thorlabs) was introduced using total internal reflection and its reflection from the coverglass-media interface was imaged onto a USB CMOS camera (DCC1545M; Thorlabs). The position of the reflected light was localized and used as feedback to adjust a piezoelectric objective positioner (P726; Physik Instrumente). Samples were incubated at 37 C using a stagetop incubator system (STXF-WSKMX-SET; Tokai Hit). All localization, visualization, and image analysis were performed using PYthon Microscopy Environment (PYME).

3.5 Supplementary Figures

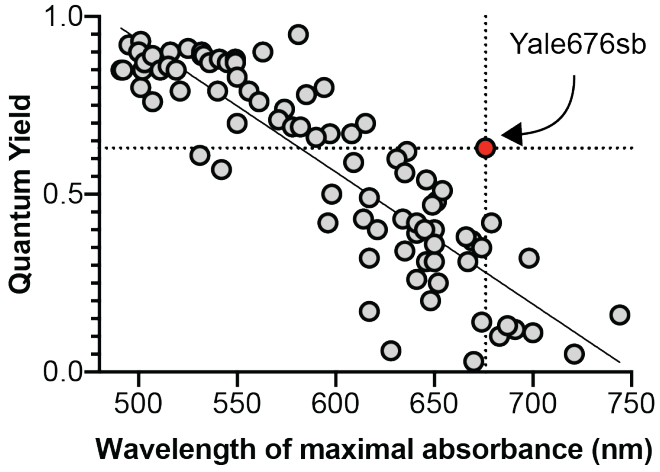

Supplementary Figure 3.1 Plot of quantum yield as a function of the wavelength of maximal absorbance (λ_{abs}) for previously reported rhodamine-derived fluorophores and $Yale_{676sb}$.

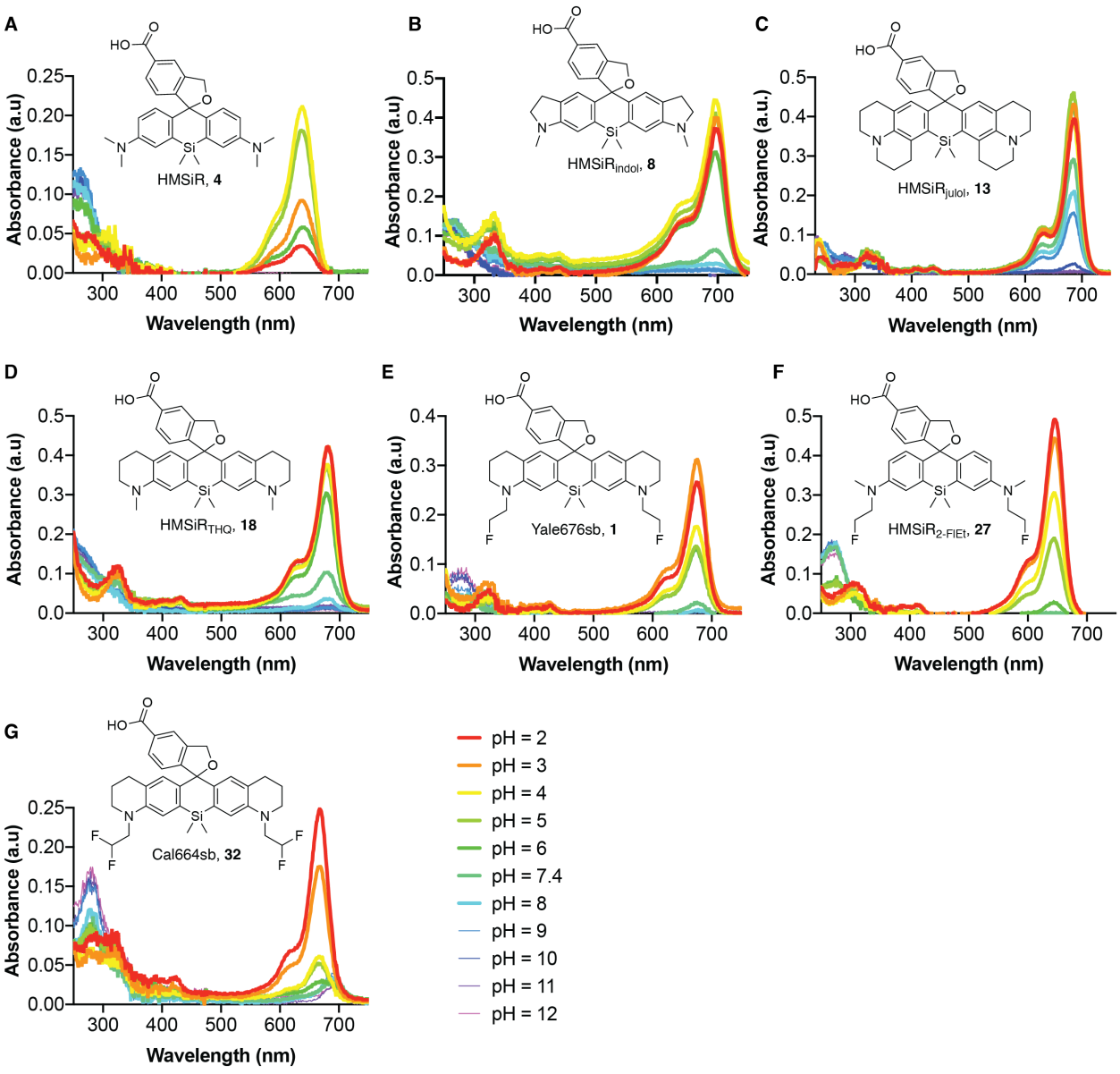

Supplementary Figure 3.2 pH-dependent absorption spectra of (a) HMSiR, (b) HMSiR$_{indol}$, (c) HMSiR$_{julol}$, (d) HMSiR$_{THQ}$, (e) Yale$_{676sb}$, (f) HMSiR$_{2\text{-}FlEt}$, and (g) Cal$_{664sb}$ at concentrations between 2 to 5 μM and at various pH values in 0.2 M sodium phosphate buffer containing 0.1% DMSO as a cosolvent.

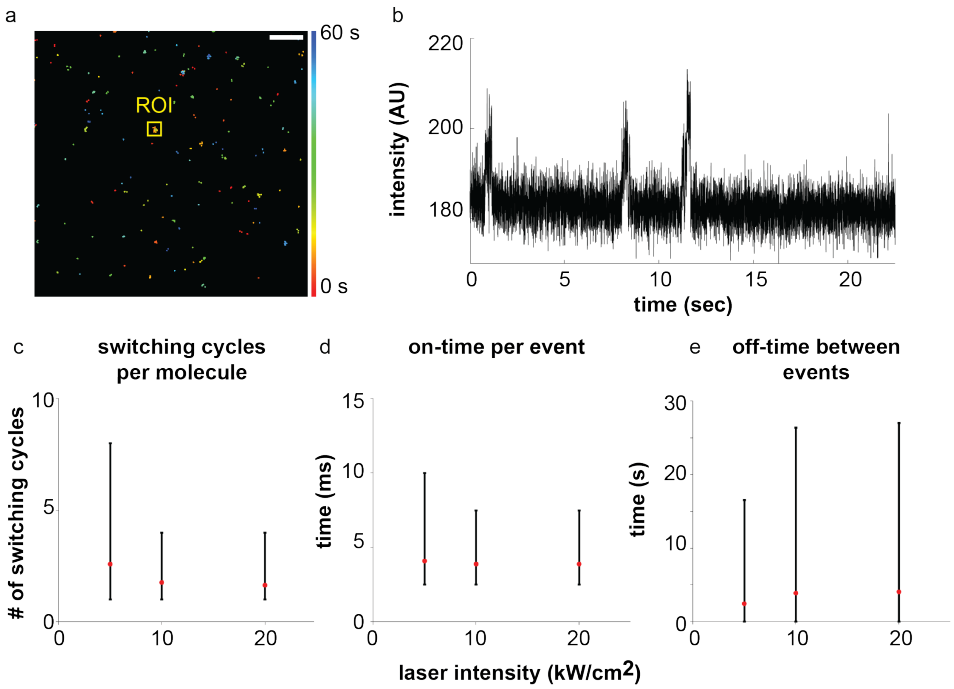

Supplementary Figure 3.3 (A) Super-resolved image of Yale$_{676sb}$ immobilized on glass colored by time of emission. Intensity trace (B) of single molecule shown in ROI of (A). Plots showing mean, 5th, and 95th percentiles for number of switching cycles (C), on-times (D), and off-times (E) for single molecules. Scale bar 1 µm. All kinetics data used 120 s of acquired frames.

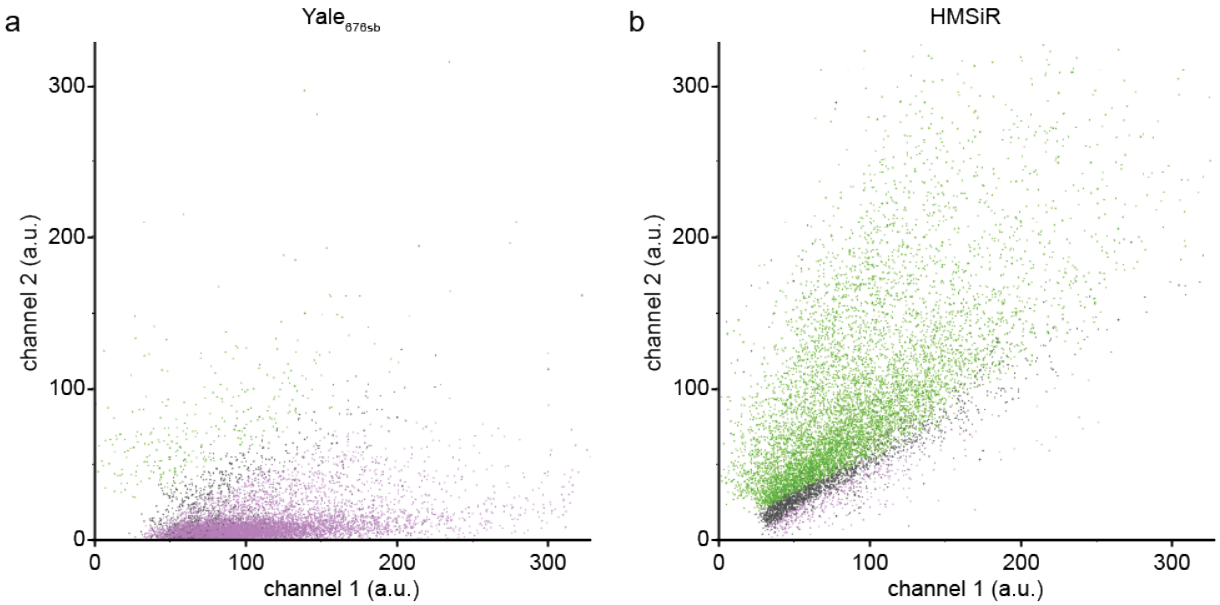

Supplementary Figure 3.4 Intensity in two camera channels for single-molecules in representative Yale$_{676sb}$ (a) and HMSiR (b) one-color samples. Molecules highlighted in purple are assigned to Yale$_{676sb}$ while those in green are assigned to HMSiR and those in black are rejected.

4.6 References

1. (1) Betzig, E.; Patterson, G. H.; Sougrat, R.; Lindwasser, O. W.; Olenych, S.; Bonifacino, J. S.; Davidson, M. W.; Lippincott-Schwartz, J.; Hess, H. F. Imaging Intracellular Fluorescent Proteins at Nanometer Resolution. *Science* **2006**, *313* (5793), 1642–1645. https://doi.org/10.1126/science.1127344.
2. (2) Rust, M. J.; Bates, M.; Zhuang, X. Sub-Diffraction-Limit Imaging by Stochastic Optical Reconstruction Microscopy (STORM). *Nat. Methods* **2006**, *3* (10), 793 796. https://doi.org/10.1038/nmeth929.
3. (3) Hess, S. T.; Girirajan, T. P. K.; Mason, M. D. Ultra-High Resolution Imaging by Fluorescence Photoactivation Localization Microscopy. *Biophys. J.* **2006**, *91* (11), 4258 4272. https://doi.org/10.1529/biophysj.106.091116.
4. (4) Heilemann, M.; van de Linde, S.; Schüttpelz, M.; Kasper, R.; Seefeldt, B.; Mukherjee, A.; Tinnefeld, P.; Sauer, M. Subdiffraction-Resolution Fluorescence Imaging with Conventional Fluorescent Probes. *Angew. Chem. Int. Ed.* **2008**, *47* (33), 6172–6176. https://doi.org/10.1002/anie.200802376.
5. (5) Zhang, Y.; Schroeder, L. K.; Lessard, M. D.; Kidd, P.; Chung, J.; Song, Y.; Benedetti, L.; Li, Y.; Ries, J.; Grimm, J. B.; Lavis, L. D.; Camilli, P. D.; Rothman, J. E.; Baddeley, D.; Bewersdorf, J. Nanoscale Subcellular Architecture Revealed by Multicolor Three- Dimensional Salvaged Fluorescence Imaging. *Nat. Methods* **2020**, *17* (2), 225–231. https://doi.org/10.1038/s41592-019-0676-4.
6. (6) Stehr, F.; Stein, J.; Schueder, F.; Schwille, P.; Jungmann, R. Flat-Top TIRF Illumination Boosts DNA-PAINT Imaging and Quantification. *Nat. Commun.* **2019**, *10* (1), 1268. https://doi.org/10.1038/s41467-019-09064-6.
7. (7) Wang, L.; Frei, M. S.; Salim, A.; Johnsson, K. Small-Molecule Fluorescent Probes for Live-Cell Super-Resolution Microscopy. *J. Am. Chem. Soc.* **2019**, *141* (7), 1 12. https://doi.org/10.1021/jacs.8b11134.
8. (8) Huang, B.; Bates, M.; Zhuang, X. Super-Resolution Fluorescence Microscopy. *Annu. Rev. Biochem.* **2009**, *78* (1), 993–1016. https://doi.org/10.1146/annurev.biochem.77.061906.092014.
9. (9) Toomre, D.; Bewersdorf, J. A New Wave of Cellular Imaging. *Annu. Rev. Cell Dev. Biol.* **2010**, *26* (1), 285–314. https://doi.org/10.1146/annurev-cellbio-100109-104048.
10. (10) Schermelleh, L.; Ferrand, A.; Huser, T.; Eggeling, C.; Sauer, M.; Biehlmaier, O.;

    Drummen, G. P. C. Super-Resolution Microscopy Demystified. *Nat. Cell Biol.* **2019**, *21*

    (1), 72–84. https://doi.org/10.1038/s41556-018-0251-8.

11. (11) Schermelleh, L.; Heintzmann, R.; Leonhardt, H. A Guide to Super-Resolution

    Fluorescence Microscopy. *J. Cell Biol.* **2010**, *190* (2), 165–175.

    https://doi.org/10.1083/jcb.201002018.

12. (12) Jradi, F. M.; Lavis, L. D. Photosensitive Fluorophores for Single-Molecule Localization

Microscopy. *ACS Chem. Biol.* **2019**. https://doi.org/10.1021/acschembio.9b00197.

13. (13) Li, H.; Vaughan, J. C. Switchable Fluorophores for Single-Molecule Localization

Microscopy. *Chem. Rev.* **2018**, *118* (18), 9412 9454. https://doi.org/10.1021/acs.chemrev.7b00767.

14. (14) Fernández-Suárez, M.; Ting, A. Y. Fluorescent Probes for Super-Resolution Imaging in Living Cells. *Nat. Rev. Mol. Cell Biol.* **2008**, *9* (12), 929–943.

https://doi.org/10.1038/nrm2531.

15. (15) Uno, S.; Kamiya, M.; Yoshihara, T.; Sugawara, K.; Okabe, K.; Tarhan, M. C.; Fujita, H.;

Funatsu, T.; Okada, Y.; Tobita, S.; Urano, Y. A Spontaneously Blinking Fluorophore Based on Intramolecular Spirocyclization for Live-Cell Super-Resolution Imaging. *Nat. Chem.* **2014**, *6* (8), 681 689. https://doi.org/10.1038/nchem.2002.

16. (16) Zheng, Q.; Ayala, A. X.; Chung, I.; Weigel, A. V.; Ranjan, A.; Falco, N.; Grimm, J. B.; Tkachuk, A. N.; Wu, C.; Lippincott-Schwartz, J.; Singer, R. H.; Lavis, L. D. Rational Design of Fluorogenic and Spontaneously Blinking Labels for Super-Resolution Imaging. *ACS Cent. Sci.* **2019**, *5* (9), 1602–1613. https://doi.org/10.1021/acscentsci.9b00676.
17. (17) Tachibana, R.; Kamiya, M.; Suzuki, S.; Morokuma, K.; Nanjo, A.; Urano, Y. Molecular Design Strategy of Fluorogenic Probes Based on Quantum Chemical Prediction of Intramolecular Spirocyclization. *Commun. Chem.* **2020**, *3* (1). https://doi.org/10.1038/s42004-020-0326-x.
18. (18) Uno, S.; Kamiya, M.; Morozumi, A.; Urano, Y. A Green-Light-Emitting, Spontaneously Blinking Fluorophore Based on Intramolecular Spirocyclization for Dual-Colour Super- Resolution Imaging. *Chem. Commun.* **2017**, *54* (1), 102–105. https://doi.org/10.1039/c7cc07783a.
19. (19) Halabi, E. A.; Pinotsi, D.; Rivera-Fuentes, P. Photoregulated Fluxional Fluorophores for Live-Cell Super-Resolution Microscopy with No Apparent Photobleaching. *Nat. Commun.* **2019**, *10* (1), 1232. https://doi.org/10.1038/s41467-019-09217-7.
20. (20) van de Linde, S.; Heilemann, M.; Sauer, M. Live-Cell Super-Resolution Imaging with Synthetic Fluorophores. *Annu. Rev. Phys. Chem.* **2012**, *63* (1), 519–540. https://doi.org/10.1146/annurev-physchem-032811-112012.
21. (21) Chi, W.; Qiao, Q.; Wang, C.; Zheng, J.; Zhou, W.; Xu, N.; Wu, X.; Jiang, X.; Tan, D.; Xu, Z.; Liu, X. Descriptor ΔGC-O Enables the Quantitative Design of

Spontaneously Blinking Rhodamines for Live-Cell Super-Resolution Imaging. *Angew. Chem.* **2020**, *132* (45), 20390–20398. https://doi.org/10.1002/ange.202010169.
22. (22) Dempsey, G. T.; Vaughan, J. C.; Chen, K. H.; Bates, M.; Zhuang, X. Evaluation of Fluorophores for Optimal Performance in Localization-Based Super-Resolution Imaging. *Nat. Methods* **2011**, *8* (12), 1027 1036. https://doi.org/10.1038/nmeth.1768.
23. (23) Jones, S. A.; Shim, S.-H.; He, J.; Zhuang, X. Fast, Three-Dimensional Super-Resolution Imaging of Live Cells. *Nat. Methods* **2011**, *8* (6), 499 505. https://doi.org/10.1038/nmeth.1605.
24. (24) Wäldchen, S.; Lehmann, J.; Klein, T.; van de Linde, S.; Sauer, M. Light-Induced Cell Damage in Live-Cell Super-Resolution Microscopy. *Sci. Rep.* **2015**, *5*, 15348.
25. (25) Zheng, Y.; Ye, Z.; Liu, Z.; Yang, W.; Zhang, X.; Yang, Y.; Xiao, Y. Nitroso-Caged Rhodamine: A Superior Green Light-Activatable Fluorophore for Single-Molecule Localization Super-Resolution Imaging. *Anal. Chem.* **2021**, acs.analchem.1c00175. https://doi.org/10.1021/acs.analchem.1c00175.
26. (26) Takakura, H.; Zhang, Y.; Erdmann, R. S.; Thompson, A. D.; Lin, Y.; McNellis, B.; Rivera- Molina, F.; Uno, S.; Kamiya, M.; Urano, Y.; Rothman, J. E.; Bewersdorf, J.; Schepartz, A.; Toomre, D. Long Time-Lapse Nanoscopy with Spontaneously Blinking Membrane Probes. *Nat. Biotechnol.* **2017**, *35* (8), 773 780. https://doi.org/10.1038/nbt.3876.
27. (27) Chu, L.-A.; Lu, C.-H.; Yang, S.-M.; Liu, Y.-T.; Feng, K.-L.; Tsai, Y.-C.; Chang, W.-K.; Wang, W.-C.; Chang, S.-W.; Chen, P.; Lee, T.-K.; Hwu, Y.-K.; Chiang, A.-S.; Chen, B.-C. Rapid Single-Wavelength Lightsheet Localization Microscopy for Clarified Tissue. *Nat. Commun.* **2019**, *10* (1), 4762. https://doi.org/10.1038/s41467-019-12715-3.
28. (28) Werther, P.; Yserentant, K.; Braun, F.; Kaltwasser, N.; Popp, C.; Baalmann, M.; Herten, D.; Wombacher, R. Live-Cell Localization Microscopy with a Fluorogenic and Self- Blinking Tetrazine Probe. *Angew. Chem. Int. Ed.* **2020**, *59* (2), 804–810. https://doi.org/10.1002/anie.201906806.
29. (29) Morozumi, A.; Kamiya, M.; Uno, S.; Umezawa, K.; Kojima, R.; Yoshihara, T.; Tobita, S.; Urano, Y. Spontaneously Blinking Fluorophores Based on Nucleophilic Addition/Dissociation of Intracellular Glutathione for Live-Cell Super-Resolution Imaging. *J. Am. Chem. Soc.* **2020**, *142* (21), 9625–9633. https://doi.org/10.1021/jacs.0c00451.

30. (30) Lampe, A.; Haucke, V.; Sigrist, S. J.; Heilemann, M.; Schmoranzer, J. Multi-colour Direct STORM with Red Emitting Carbocyanines. *Biol. Cell* **2012**, *104* (4), 229–237. https://doi.org/10.1111/boc.201100011.
31. (31) Winterflood, C. M.; Platonova, E.; Albrecht, D.; Ewers, H. Dual-Color 3D Superresolution Microscopy by Combined Spectral-Demixing and Biplane Imaging. *Biophys. J.* **2015**, *109* (1), 3–6. https://doi.org/10.1016/j.bpj.2015.05.026.
32. (32) Koide, Y.; Urano, Y.; Hanaoka, K.; Piao, W.; Kusakabe, M.; Saito, N.; Terai, T.; Okabe, T.; Nagano, T. Development of NIR Fluorescent Dyes Based on Si–

Rhodamine for in Vivo Imaging. *J. Am. Chem. Soc.* **2012**, *134* (11), 5029 5031. https://doi.org/10.1021/ja210375e.
33. (33) Lukinavičius, G.; Reymond, L.; Umezawa, K.; Sallin, O.; D'Este, E.; Göttfert, F.; Ta, H.; Hell, S. W.; Urano, Y.; Johnsson, K. Fluorogenic Probes for Multicolor Imaging in Living Cells. *J. Am. Chem. Soc.* **2016**, *138* (30), 9365–9368. https://doi.org/10.1021/jacs.6b04782.
34. (34) Butkevich, A. N.; Ta, H.; Ratz, M.; Stoldt, S.; Jakobs, S.; Belov, V. N.; Hell, S. W. Two- Color 810 Nm STED Nanoscopy of Living Cells with Endogenous SNAP-Tagged Fusion Proteins. *ACS Chem. Biol.* **2018**, *13* (2), acschembio.7b00616 6. https://doi.org/10.1021/acschembio.7b00616.
35. (35) Grimm, J. B.; Brown, T. A.; Tkachuk, A. N.; Lavis, L. D. General Synthetic Method for Si- Fluoresceins and Si-Rhodamines. *ACS Cent. Sci.* **2017**, *3* (9), 975–985. https://doi.org/10.1021/acscentsci.7b00247.
36. (36) Belov, V. N.; Bossi, M. L.; Fölling, J.; Boyarskiy, V. P.; Hell, S. W. Rhodamine Spiroamides for Multicolor Single-Molecule Switching Fluorescent Nanoscopy. *Chem. - Eur. J.* **2009**, *15* (41), 10762–10776. https://doi.org/10.1002/chem.200901333.
37. (37) Rettig, W. STRUCTURAL RELAXATION OF RHODAMINE DYES WITH DIFFERENT N- SUBSTITUTION PAITERNS: A STUDY OF FLUORESCENCE DECAY TIMES AND QUANTUM YIELDS. *Chem. Phys.* **1988**, 452 460.
38. (38) Grimm, J. B.; English, B. P.; Chen, J.; Slaughter, J. P.; Zhang, Z.; Revyakin, A.; Patel, R.; Macklin, J. J.; Normanno, D.; Singer, R. H.; Lionnet, T.; Lavis, L. D. A General Method to Improve Fluorophores for Live-Cell and Single-Molecule Microscopy. *Nat. Methods* **2015**, *12* (3), 244 250. https://doi.org/10.1038/nmeth.3256.
39. (39) Grabowski, Z. R.; Rotkiewicz, K.; Rettig, W. Structural Changes Accompanying Intramolecular Electron Transfer: Focus on Twisted Intramolecular Charge-Transfer States and Structures. *Chem. Rev.* **2003**, *103* (10), 3899–4032. https://doi.org/10.1021/cr940745l.
40. (40) Karstens, T.; Kobs, K. Rhodamine B and Rhodamine 101 as Reference Substances for Fluorescence Quantum Yield Measurements. *J. Phys. Chem.* **1980**, *84* (14), 1871–1872. https://doi.org/10.1021/j100451a030.
41. (41) Lv, X.; Gao, C.; Han, T.; Shi, H.; Guo, W. Improving the Quantum Yields of Fluorophores by Inhibiting Twisted Intramolecular Charge Transfer Using Electron-Withdrawing Group- Functionalized Piperidine Auxochromes. *Chem. Commun.* **2019**, *56* (5), 715–718. https://doi.org/10.1039/c9cc09138f.
42. (42) Diekmann, R.; Kahnwald, M.; Schoenit, A.; Deschamps, J.; Matti, U.; Ries, J. Optimizing Imaging Speed and Excitation Intensity for Single-Molecule Localization Microscopy. *Nat. Methods* **2020**, *17* (9), 909–912. https://doi.org/10.1038/s41592-020-0918-5.
43. (43) Bottanelli, F.; Kromann, E. B.; Allgeyer, E. S.; Erdmann, R. S.; Wood Baguley, S.; Sirinakis, G.; Schepartz, A.; Baddeley, D.; Toomre, D. K.; Rothman, J. E.; Bewersdorf, J. Two-Colour Live-Cell Nanoscale Imaging of Intracellular Targets. *Nat. Commun.* **2016**, *7* (1), 10778. https://doi.org/10.1038/ncomms10778.

44. (44) Schroeder, L. K.; Barentine, A. E. S.; Merta, H.; Schweighofer, S.; Zhang, Y.; Baddeley, D.; Bewersdorf, J.; Bahmanyar, S. Dynamic Nanoscale Morphology of the ER Surveyed by STED Microscopy. *J. Cell Biol.* **2019**, *218* (1), 83–96. https://doi.org/10.1083/jcb.201809107.

45. (45) Zhou, X.; Lai, R.; Beck, J. R.; Li, H.; Stains, C. I. Nebraska Red: A Phosphinate-Based near-Infrared Fluorophore Scaffold for Chemical Biology Applications. *Chem. Commun.* **2016**, *52* (83), 12290–12293. https://doi.org/10.1039/C6CC05717A.
46. (46) Grimm, J. B.; Muthusamy, A. K.; Liang, Y.; Brown, T. A.; Lemon, W. C.; Patel, R.; Lu, R.; Macklin, J. J.; Keller, P. J.; Ji, N.; Lavis, L. D. A General Method to Fine-Tune Fluorophores for Live-Cell and in Vivo Imaging. *Nat. Methods* **2017**, *14* (10), e04236 14. https://doi.org/10.1038/nmeth.4403.
47. (47) Grimm, J. B.; Tkachuk, A. N.; Xie, L.; Choi, H.; Mohar, B.; Falco, N.; Schaefer, K.; Patel, R.; Zheng, Q.; Liu, Z.; Lippincott-Schwartz, J.; Brown, T. A.; Lavis, L. D. A General Method to Optimize and Functionalize Red-Shifted Rhodamine Dyes. *Nat. Methods* **2020**, *17* (8), 815–821. https://doi.org/10.1038/s41592-020-0909-6.

Chapter 4. Summary of Future Directions

This chapter summarizes a series of projects designed and proposed, but never fully realized during my graduate degree. The goal of this chapter is to carefully outline three experiment which I envision to be areas of high interest to any future graduate students and post-docs looking to expand upon the work described in this dissertation.

4.1 Fluoroethyl functionalization as a versatile strategy for generating optimized rhodamine fluorophores

Bright and photostable fluorophores are essential tools for cellular imaging due to their ability to increase contrast and resolution[1–3]. Generally, fluorophores emitting at shorter, greener wavelengths tend to possess higher fluorescence quantum yields and accordingly higher brightnesses[4]. Unfortunately, these molecules are often incompatible with live cell imaging as they require excitation with high energy lasers such as commonly utilized 488 nm lasers that are cytotoxic at even moderate intensities[5]. Over the past few years, N'N-azetidinyl-containing rhodamines have began to see use as alternatives to commonly utilized tetramethyl rhodamines, since the former generally possess higher quantum yields while absorbing and emitting at similar wavelengths[6–10]. For example, the tetramethyl-containing carboxy-SiR emits at 662 nm with a quantum yield of 0.41, while the azetidinyl-containing JF646 emits at 664 nm with a quantum yield of 0.54[10]. This technique is limited; however, in that it necessitates substitution at all available nitrogen substitution sites to be effective. We have recently demonstrated that similar effects can be observed when a single N-methyl substituent on each nitrogen of a rhodamine fluorophore is substituted for a 2-fluoroethyl substituent[4]. For example, whereas HMSiR emits at 667 nm with a quantum yield of 0.31, $HMSiR_{2\text{-}FlEt}$ emits at 666 nm with a quantum yield of 0.51[4]. This effect is analogous to that observed via N'N-azetidinyl substitution while requiring half as many substitution sites. If generalized, this strategy may be a versatile alternative, enabling brighter alternatives to molecules like HMSiRindol, a feat currently unachievable via azetidinyl substitution.

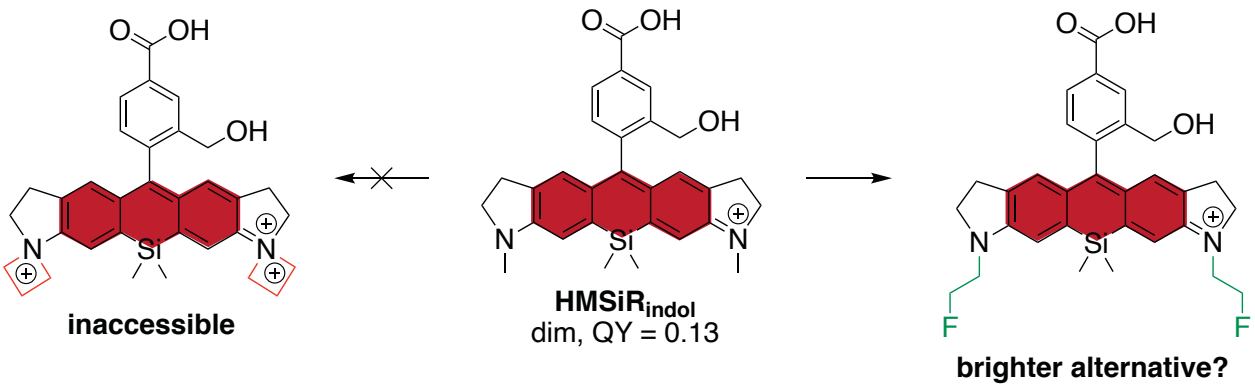

Figure 4.1 Fluoroethyl rhodamines as a general strategy. In contrast to N,N-azetidinyl substitution of N-methyl substituents, which requires two positions on each N, 2-fluoroethyl substitution requires only one substitution on each, but induces a similar effect.

4.2 Optimized rhodamines across the visible spectrum

One of the defining features of rhodamine fluorophores is their ability to exist in equilibrium between open, fluorescent and closed, non-fluorescent forms[11]. This equilibrium confers several favorable properties, including cell permeance[4,12–17], fluorogenicity[12,18,19] and spontaneous blinking[4,17,20,21]. The position of this equilibrium is particularly sensitive to the identity of the atom at the bridgehead of the fluorophore. For example, conventional rhodamines with O at the bridgehead generally have equilibriums that greatly favor the open form of the molecule. C-rhodamines have equilibriums that favor the closed form slightly more than conventional O-rhodamines. These are followed by Si-rhodamines, who themselves are followed by phosphinate-containing rhodamines and finally sulfonate-containing rhodamines, which are generally nearly completely closed at equilibrium[6]. These differences come into play when one must consider how to further functionalize these fluorophores. A common method for increasing the brightness of rhodamines is via the inclusion of electron withdrawing groups (EWGs) into the dialkylamino group (DAG) of the xanthene core[4,9,10,22]. This modification increases fluorescence quantum yield via the inhibition of twister intamolecular charge transfer (TICT), one of the primary quenching mechanism in rhodamine fluorophores. This increased electron-withdrawing capacity; however, further shifts the open-closed equilibrium to the closed form[4], which can be detrimental to the sensitive equilibria of Si-rhodamines, phosphinate rhodamines and sulfonate rhodamines. Recently, we have demonstrated that combining EWGs with heterocyclic DAGs can offset the effects on ring closure[4]. For example, whereas the electron-withdrawing HMSiR2-FlEt possesses a low pKcycl of 5.0, Yale676sb, which combines the electron withdrawing 2-fluoroethyl groups with the more electron donating tetrahydroquinolinyl DAGs has a pKcycl of 5.9, nearly identical to HMSiR's pKcycl of 6.0, while possessing the highest quantum yield of the three[4]. As phosphinate and sulfonate esters possess open-closed equilibria that even more strongly favor the closed form, I have proposed installing even more electron-donating morpholino and piperazino groups respectively. On the other hand, for rhodamines and carborhodamines, more electron withdrawing trifluoroethyl and difluoroethyl groups, respectively, would help to close the ring enough to improve the ability of these fluorophores to blink spontaneously and/or serve as fluorogenic labels, all while receiving an increase in brightness.

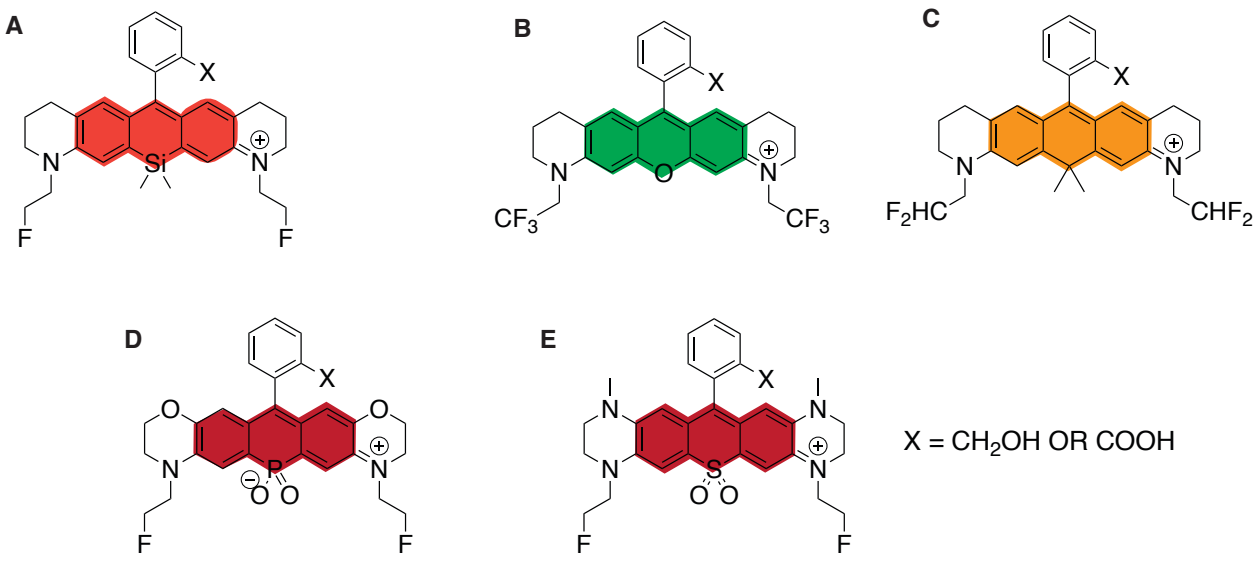

Figure 4.2 Proposed structures for optimized rhodamines across the visible spectrum. (A) Si-rhodamines bearing heterocyclic tetrahydroquinolino and 2-fluoroethyl DAGs possess high quantum yield and favorable open-closed equilibrium. (B) Rhodamines are naturally much more open at equilibrium than Si-rhodamines. Accordingly, addition of trifluoroethyl groups should hopefully simultaneously increase brightness and bring open-closed equilibrium into a similar range as structure seen in A. (C) Carborhodamines have open-closed equilibria intermediate between rhodamines and Si-rhodamines. Accordingly, an electron withdrawing group intermediate between those used for A and B should increase brightness while simultaneously maintaining open-closed equilibrium in fair range. (D) Phophinate-containing rhodamines are more closed than Si-rhodamines at equilibrium, therefore replacement of tetrahydroquinolino DAG for more electron-donating morpholino DAG should help to maintain open-closed equilibrium in fair range. (E) Sulfonate-containing rhodamines have open-closed equilibria that nearly completely favor the closed form. Installation of the very electron-donating piperazino DAG should help to push open-closed equilibrium back towards open form.

4.3 Spontaneously blinking fluorophores for acidic organelles

Spontaneously blinking fluorophores (SBFs) are powerful tools for live cell single molecule localization microscopy (SMLM)[4,16,17]. In contrast to conventional SMLM-compatible fluorophores, they blink in the absence of chemical additives and can therefore enable nanoscopy in near-physiological conditions [4,16,17]. A limitation of SBFs is that the position of their equilibrium and therefore the fraction of molecules existing in the 'ON' state is highly sensitive to pH. For example, whereas HMSiR can enable SMLM in the neutral pH of the endoplasmic reticulum[16], it is incompatible with the more acidic pH of the trans-Golgi network[16]. Recently, we have reported two SBFs with pKcycl's below those of HMSiR[4]. These molecules, HMSiR2-FlEt and Cal664sb are likely to enable SMLM within these more acidic environments.

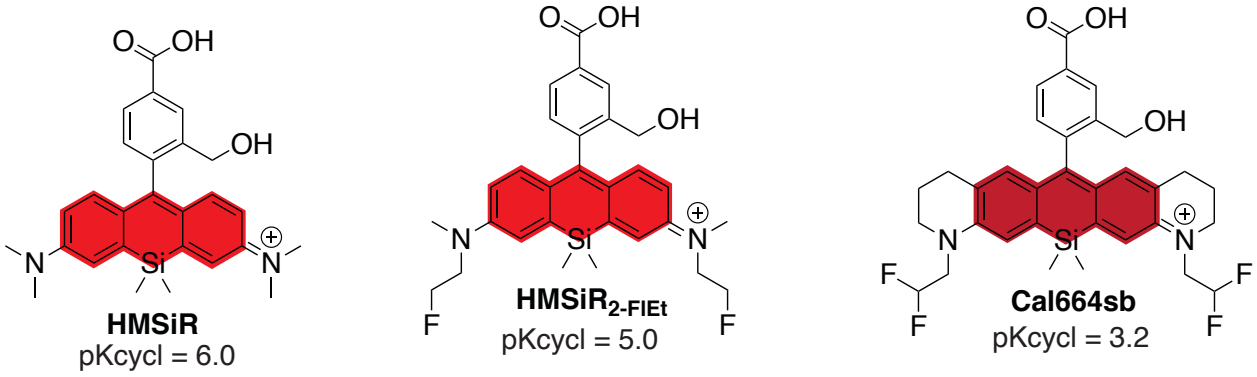

Figure 4.3 Spontaneously blinking fluorophores compatible with acidic organelles. $HMSiR_{2\text{-}FlEt}$ and Cal664sb are designed to have lower pH's than HMSiR. As a result, even at lower pH, the majority of these molecules will still be in the closed form, enabling SMLM in acidic organelles.

4.4 References

1. Wang, L., Frei, M. S., Salim, A. & Johnsson, K. Small-Molecule Fluorescent Probes for Live-Cell Super-Resolution Microscopy. *J Am Chem Soc* 141, 1 12 (2018).

2. Jradi, F. M. & Lavis, L. D. Photosensitive fluorophores for single-molecule localization microscopy. *ACS Chemical Biology* (2019) doi:10.1021/acschembio.9b00197.

3. Li, H. & Vaughan, J. C. Switchable Fluorophores for Single-Molecule Localization Microscopy. *Chem Rev* 118, 9412 9454 (2018).

4. Tyson, J. *et al.* Extremely Bright, Near-IR Emitting Spontaneously Blinking Fluorophores Enable Ratiometric Multicolor Nanoscopy in Live Cells. *Acs Central Sci* (2021) doi:10.1021/acscentsci.1c00670.

5. Light-induced cell damage in live-cell super-resolution microscopy. *Sci Rep-uk* 5, 1 12 (2015).

6. Grimm, J. B. *et al.* A general method to optimize and functionalize red-shifted rhodamine dyes. *Nat Methods* 17, 815–821 (2020).

7. Zheng, Q. *et al.* Rational Design of Fluorogenic and Spontaneously Blinking Labels for Super-Resolution Imaging. *Acs Central Sci* 5, 1602–1613 (2019).

8. Grimm, J. B., Brown, T. A., Tkachuk, A. N. & Lavis, L. D. General Synthetic Method for Si-Fluoresceins and Si-Rhodamines. *Acs Central Sci* 3, acscentsci.7b00247 11 (2017).

9. Grimm, J. B. *et al.* A general method to fine-tune fluorophores for live-cell and in vivo imaging. *Nat Methods* 14, e04236 14 (2017).

10. Grimm, J. B. *et al.* A general method to improve fluorophores for live-cell and single-molecule microscopy. *Nat Methods* 12, 244 250 (2015).

11. Lavis, L. D. & Raines, R. T. Bright Building Blocks for Chemical Biology. *Acs Chem Biol* 9, 855 866 (2014).

12. Lukinavičius, G. *et al.* A near-infrared fluorophore for live-cell super-resolution microscopy of cellular proteins. *Nat Chem* 5, 1 8 (2012).

13. Lukinavičius, G., Johnsson, K., Hell, S. W. & Urano, Y. Fluorogenic Probes for Multicolor Imaging in Living Cells. 1 4 (2016) doi:10.1021/jacs.6b04782/suppl_file/ja6b04782_si_002.pdf.

14. Chu, L. *et al.* Two-color nanoscopy of organelles for extended times with HIDE probes. *Nature Communications* 11, (2020).

15. Gupta, A., Rivera-Molina, F., Xi, Z., Toomre, D. & Schepartz, A. Endosome motility defects revealed at super-resolution in live cells using HIDE probes. *Nat Chem Biol* 1–7 (2020) doi:10.1038/s41589-020-0479-z.

16. Takakura, H. *et al.* Long time-lapse nanoscopy with spontaneously blinking membrane probes. *Nat Biotechnol* 35, 773 780 (2017).

17. Uno, S. *et al.* A spontaneously blinking fluorophore based on intramolecular spirocyclization for live-cell super-resolution imaging. *Nat Chem* 6, 681 689 (2014).

18. Lukinavičius, G. *et al.* Fluorogenic Probes for Multicolor Imaging in Living Cells. *J Am Chem Soc* 138, 9365–9368 (2016).

19. Butkevich, A. N. *et al.* Fluorescent Rhodamines and Fluorogenic Carbopyronines for Super-Resolution STED Microscopy in Living Cells. *Angewandte Chemie Int Ed* 55, 3290–3294 (2016).

20. Uno, S., Kamiya, M., Morozumi, A. & Urano, Y. A green-light-emitting, spontaneously blinking fluorophore based on intramolecular spirocyclization for dual-colour super-resolution imaging. *Chem Commun* 54, 102–105 (2017).

21. Zheng, Q. *et al.* Electronic tuning of self-healing fluorophores for live-cell and single-molecule imaging. *Chem Sci* 8, 755–762 (2017).

22. Lv, X., Gao, C., Han, T., Shi, H. & Guo, W. Improving the quantum yields of fluorophores by inhibiting twisted intramolecular charge transfer using electron-withdrawing group-functionalized piperidine auxochromes. *Chem Commun* 56, 715–718 (2019).